Passive Intermodulation and Corona Discharge for Microwave Structures in Communications Satellites

Vom Fachbereich 18
Elektrotechnik und Informationstechnik
der Technischen Universität Darmstadt
zur Erlangung der Würde
eines Doktor-Ingenieurs (Dr.-Ing.)
genehmigte

Dissertation

von Dipl.-Phys.

Carlos Pascual Vicente Quiles

geboren am 12. September 1976
in Elche

Referent:	Prof. em. Dr. Eng. Dr. h.c. mult. H.L. Hartnagel
Korreferent:	Prof. Dr.-Ing. V. Hinrichsen
Korreferent:	Prof. Dr.-Phys. B. Gimeno Martínez
Tag der Einreichung:	18. Mai 2005
Tag der mündlichen Prüfung:	29. June 2005

D17
Darmstädter Dissertationen

A mis padres

Preface

This thesis originates from my research activities at the Institute for Microwave Engineering of the Darmstadt University of Technology. The work perfomed was supported by the European Comission and the European Space Agency in the frame of several research projects.

I would like to express my gratitude to Prof. em. Dr. Eng. Dr. h.c. mult H.L. Hartnagel for giving me the possibility to work within his international research group and for his confidence on my work, as well as for offering me an extraordinary opportunity to meet a wide spectrum of international scientists. My deepest gratitude is also due to Prof. Dr.-Ing V. Hinrichsen and Prof. Dr.-Phys. B. Gimeno for his readiness to accept the surveyance of this thesis.

Special thanks are due to many colleagues of the Institute for fruitful discussions and for creating a very healthy working atmosphere, in particular, Dr. Manuel Rodriguez-Girones, Dr. Bastian Mottet, Dr. Martin Droba, Albert Cervelló, Nicolae Bogdan and Cezary Sydlo.

This thesis has been possible thanks to the interaction with different people from several organizations. In particular, special thanks are due to Dr. Michael Mattes (EPFL/LEMA, Lausanne, Switzerland) for many fruitful conversations at all levels. Thanks also to the team from Tesat-Spacecom GmbH & Co. KG (Backnang, Germany) for his help in the whole sense of word. Specially, I would like to thank Mr. Meinrad Abele, Mr. Dieter Wolk, Mr. Ulrich Woechner, Mr. Karl-Georg Hampf, Mr. Wilhelm Hartmann, and the rest of the staff at Tesat laboratories. My gratitude also to Mr. David Raboso from the European Space Agency (ESA/ESTEC, Noordwijk, The Netherlands) for his confidence and help. Finally, I would also like to thank all the people and organisations which were involved in the MMCODEF project.

I would also like to express my gratitude to students who helped me in some research projects, in particular, Rafael Peña Bello and Patrick Davis for their great effort in the Java programming environment.

I remain in debt with Alex Pérez and Jaume Masvidal for having the patience and peace of mind to read and correct this thesis.

Many people have influenced my life to take me to this point. I need to thank my parents and my whole family (which is becoming larger and larger) to have helped me to be as I am. I can proudly say that I have many friends. Friends I made here and friends I already had when I left my home country. To all of them many thanks to stand me as I am. Last but not least, I would like to thank Carolina for her support and patience during this crusade called PhD. But above all, I would like to thank her to have helped me to find my place in this world. Always by her side.

Darmstadt, May 2005,

Carlos P. Vicente Quiles

Abstract

As times goes by, satellite communication systems demand for higher component integration. Besides, an increase of services is also required, what implies the use of larger bandwidths. To achieve these objectives, the size of microwave devices on the one hand incessantly decreases whereas, at the same time, the power levels increase. Both trends lead to a higher electromagnetic field density inside the components. This development leads to serious problems with respect to RF breakdown (Corona Discharge and Multipactor) caused by high electromagnetic field densities, and cross-talking interference (Passive Intermodulation) due to bandwidth requirements.

In this work, Passive Intermodulation (PIM) at waveguide flanges and Corona Discharge in microwave components, e.g. filters, are investigated. In both cases, theoretical research is developed in order to understand the physical mechanisms lying behind both phenomena. Results are presented which are useful for providing particular guidelines to avoid both effects in Sat-Com applications. Systematic experimental research for both phenomena is also presented along the thesis.

Contents

Chapter 1

Introduction

In the last years a tremendous effort has been devoted to develop numerical techniques and software tools in order to characterise the electromagnetic response of microwave devices such as filters or resonators. However, today microwave applications in communications satellite systems demand a larger bandwidth integration, higher component integration and more power handling capability. These three requirements lead to both, higher electric field densities inside the devices and an increasing risk of carrier crosstalking. Therefore, it is also indispensable to analyse the impact of such effects in the normal operation of a satellite by means of theoretical models and its implementation in software programs. Nevertheless, no software tools, not even models in some cases, exist in order to assess this impact. This results in high-cost test campaigns as well as long design periods since no reliable prior analysis is possible. Hence, an increasing interest from the satellite industry is being paid to this area in order to remedy such a lack.

Several physical phenomena can take place limiting the capability of a subsystem within a satellite for handling high power signals. In particular, the most relevant are, as long as passive components are concerned, *Passive Intermodulation* (PIM), *Corona Discharge* and *Multipactor Breakdown*. The former is an intrinsic multicarrier problem where interference between carriers results in a malfunctioning of the satellite communications system. It is, however, a non-destructive hardware phenomenon since low power signals are generated. On the contrary, corona and multipactor can occur in both scenarios: single and multi-carrier. They are highly dangerous from the integrity of the satellite hardware viewpoint since they result in an increase of the reflected power which, in turn, dramatically rises the temperature of the device rendering it useless.

The lack of prediction is critical in the case of PIM for which the use of a universal model is not possible due to the erratic and random nature of the phenomenon. However, as we will see, useful models for the design of PIM free systems can be developed provided experimental data is known. For corona and multipactor, some models and tools exist for their analysis. However, they are commonly based on assuming simplified geometries. In fact, analysis tools for arbitrary complex devices are not available for the scientific or the industrial community.

As far as this work is concerned, passive intermodulation at waveguide connections

and corona discharge in complex components based on rectangular waveguide technology are going to be investigated.

Passive Intermodulation [1–4] has its origin in the existence of a non-linear component in the system which generates harmonics of the input signal. If, additionally, more than one signal is present, intermodulation products are also excited. For the sake of understanding, if only two carriers are considered, the intermodulation frequencies are:

$$f_{int} = m f_1 + n f_2$$

where f_1 and f_2 are the two input frequencies, f_{int} is the frequency of the intermodulation product, m and n are integer numbers and the relation $|m| + |n| = N$ provides the intermodulation order N. Moreover, in common situations the dangerous signals are those which accomplish that $m + n = \pm 1$ since these are the intermodulation products falling close to the input carriers. Hence, for third order (N=3) $|m| = 2$, $|n| = 1$ or $|m| = 1$, $|n| = 2$, for fifth order (N=5) $|m| = 3$, $|n| = 2$ or $|m| = 2$, $|n| = 3$, and so on, where always $\mathrm{sign(m)} \neq \mathrm{sign(n)}$.

These PIM signals originated in the transmission band of the satellite can fall in the reception band. Despite the fact that these excited signals have low power (since they have been originated by passive components), the received carriers are also low-power signals and therefore, interference can occur. This can be easily understood considering that, for instance, a geostationary satellite is situated in a 36.000 Km radius orbit. If a signal of power P_0 is isotropically emitted from Earth, though this is not usually the case, the input power P_i in the satellite is approximately: $P_i = P_0/(4\pi r^2) \sim 10^{-15} \cdot P_0$. Therefore, it is clear that, although the intermodulation level can be very low compared to the signals that generate it (transmitted ones), it can seriously affect the reception band. Such a scenario is very usual in communications satellites due to the need of reducing weight employing common paths for both the transmission and the reception bands. For instance, only one antenna is commonly used for the reception and transmission bands in a standard satellite. In fact, the Passive Intermodulation interference was first identified in ships which had two antenna but located close enough to be affected by each other. This was originally called the "rusty-bolt" effect.

The actual problem of the PIM distortion is that it can not be mitigated by using any kind of filtering technique. Since the transmitted and the reception carriers share the same hardware, the intermodulation signals excited can not be filtered out without affecting the original carriers. The only possible prevention is a clever use of the frequency bands in such a way that the intermodulation orders falling inside the reception band are as high as possible since the higher the order the lower its power. However, as mentioned before, as time goes by the frequency operation bands are more and more restrictive and thus, this "rule of thumb" can not be easily applied. Even in the cases where this is possible, the increasing power of the carriers makes higher orders more dangerous from the PIM generation point of view.

Many PIM sources have been identified along the years [5], [6]. Among them, the most important probably are:

- Ferromagnetic materials.

- Metal-to-Metal junctions.

Ferromagnetic materials like nickel or iron have shown high PIM levels (see e.g. [6]) which have their origin in the non-linear relationship between the magnetic field (H) and the magnetic flux density (B) due to the dependence of the magnetic permeability with the applied magnetic field. This results in the well-known B-H hysteresis cycle.

This work deals with a particular case of Metal-to-Metal junctions which is a highly problematic source of intermodulation in satellites: waveguide connections [7]. The excitation of PIM in this system has been associated with several physical mechanisms [5, 8]. In any case, it is accepted that whatever the mechanism responsible for PIM at waveguide junctions is, it can be mitigated by applying high mechanical loads between the waveguides. This can be easily understood if one is aware of the microscopic configuration of metal-to-metal (MM) contacts. Due to the roughness of the metal surfaces, the contact between two metals is never perfect. Therefore, a two-waveguide junction system can be viewed as a combination of metal contact zones and non-contact ones. In addition to roughness, metal surfaces always present a native oxide or sulfide (as for silver) layer recovering them as well as contaminants like oxygen or carbon. The thickness of this layer depends on the metal itself though it is generally in the order of few nanometres. Therefore, the real MM contacts (a-spots) are even more reduced due to the presence of the dielectric layer.

Fig.1.1 shows the system under investigation. The waveguide connection is considered to be separated by a dielectric layer that has been exaggerated and the surface roughness is not visible and, therefore, the air gaps between the flanges neither.

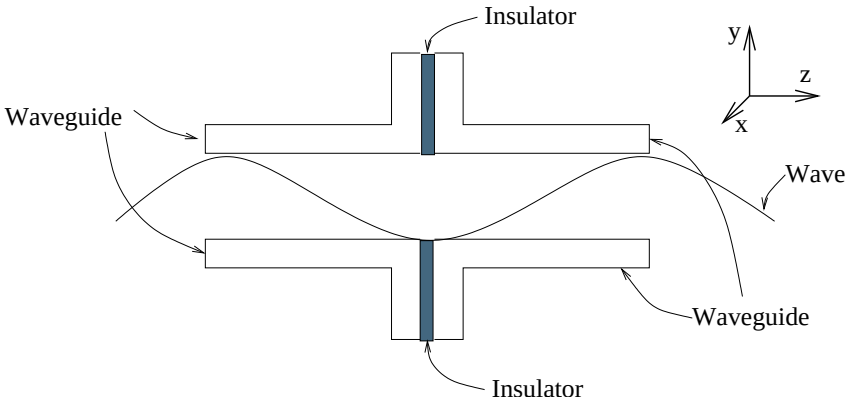

Figure 1.1: *Side view of a two rectangular waveguides connection. The dielectric layer has been exaggerated and the roughness is not apparent, hiding the real surface aspect where air gaps between the waveguides also occur.*

There are not very much published measured data focused on the dependence of the

PIM level on the applied mechanical load. The most important are probably those according to Bayrak [9], Arazm [10], Martin [11–14] and more recently Weibel [8]. In their studies, the PIM level was investigated for different materials as a function of the applied force. They concluded that in general the PIM level strongly depends on the cleanliness of the surfaces and it is not so dependent on the surface roughness. Normally, they observed that the intermodulation level keeps approximately constant (sometimes increasing or decreasing a bit) with the applied load until a threshold load is applied from which it decreases very sharply. This was associated with the formation of metallic contacts due to the rupture of the oxide layer at high loads which results in a decrease of the contact resistance and, therefore, of the PIM level. They also observed that at very low loads, the intermodulation level is quite unstable. For some metals, like gold or silver, they found that the rupture of the covering layer takes place at very low applied forces and, thus, the intermodulation level is driven rapidly under the noise level. In other cases, like steel or aluminium, the intermodulation level kept more or less constant even at very high loads because the covering layer could not be displaced at all. Nevertheless, these experimental data were not obtained for rectangular waveguides but for coaxial lines or connectors.

In this work, a theoretical model has been developed which qualitatively agrees with this data. Moreover, experimental measurements have been performed which are useful for extracting the general behaviour of waveguide flanges for different coating materials.

Corona Discharge is a process by which an electron plasma is formed due to the ionisation of the gas surrounding a zone of high electric field. In normal life one can see this phenomenon in lightnings or on the mast of a ship in a stormy day (St. Elmo's fire). As far as microwave technology is concerned, this phenomenon occurs, for instance, in waveguide filters where the high electric field reached is capable to ignite corona for relatively low pressures (100 - $1{\cdot}10^5$ Pa) which, in atmospheric terms, comprises the Ionosphere (60 to 800 Km height). Since this phenomenon can not occur in vacuum conditions because a gas is necessary for the generation of the electron plasma, it seems not to be a potential danger in satellite applications due to the fact that the operating condition of a satellite is at very low pressures. However, the Telemetry, Tracking and Control system (TTC) is sometimes switched on during launching and therefore, the ionosphere region has to be crossed. It is in these moments when corona breakdown can take place, rendering useless system components. Moreover, an increasing attention is being paid to corona in the case of reentry vehicles due to the exploration of planets and their moons such as Mars or Titan.

The consequences of a corona discharge in a microwave component are extremely harmful. The transmitted power decreases which can lead to the destruction of the power source. Due to this higher reflection, the temperature also rises which finally results in the complete destruction of the device. The prevention of corona relies in the careful testing of the subsystems during the satellite test campaign. In fact, the operating power of the device must be at least 3 dB lower than the measured breakdown power in order to ensure that the discharge will not occur in flight conditions following the space industry margins. Therefore, from the microwave components designer point of view, the corona discharge

power threshold is the critical parameter to be taken into consideration. In other words, the largest input power that a particular device can admit without developing a corona discharge.

Experimentally, several methods must be applied simultaneously in order to ensure that a corona event has occurred. Among them, third harmonic detection, reflection power and/or electronic current measurements are probably the most commonly used. A summary of such detection methods can be found in [15].

Original papers in this field date from the beginning of the past century. For instance, Kunz [16] and Fazel [17] were some of the first authors investigating the problem and performing measurements. In the 40's, a large amount of interest was paid to the study of corona in high frequency fields (see e.g. [18–22]). The first important compilation of theory and measurements about corona in microwave components was performed by MacDonald [23]. In his book, a comprehensive and systematic analysis is done and the fundamentals of the corona discharge are addressed. His investigation mainly dealt with noble gases like helium, neon or argon, although experimental results in hydrogen, nitrogen and air were also fully described in the cases of DC and RF excitations. He also described experimental data in the case of pulse source. More recently, a full analysis has been also performed by Raizer [24] which also includes the fundamentals of the corona breakdown but additionally, pays special attention to the electron plasma behaviour after the discharge.

Other works in corona are also of high interest both experimentally and theoretically. For instance, Woo and DeGroot [25] measured the diffusion, ionisation and attachment coefficients in the case of dry air. Moreover, they provided phenomenological expressions which relate these parameters to the electric field and the environment pressure. Other authors have also measured these quantities for air and other gases. In this way, DeBitetto [26], [27] investigated the cases of hydrogen, oxygen and nitrogen. Harrison [28] also measured the ionisation and attachment coefficients for air and oxygen. MacDonald [20] investigated the microwave breakdown phenomenon in the cases of air, nitrogen and oxygen [29]. Huber [30] studied the microwave corona discharge in nitrogen, oxygen and their mixtures as well.

Light [31] and more recently Anderson et al. [32] have investigated the effect of the temperature in the corona discharge onset. This is important since the high power densities that can be reached inside a particular region of a component can heat up the gas considerably. They have found that an increase of the temperature results in a decrease of the breakdown threshold. However, this is only applicable for high pressures. At low pressures (where the corona effect becomes critical in Sat-Com applications) this statement is not generally true.

The importance of humidity on the corona discharge breakdown level in air was experimentally studied, among others, by Bandel [33], Verhaart [34] or Calva [35]. Differences in the breakdown threshold at different humidities seem to have its origin in the difference between the collision frequencies of water and air. Like in the case of temperature, for a wide range of pressures, an increase of the humidity is associated with a decrease of the breakdown onset. However, this is again open to discussion in the case of low pressures.

Platzman et al. [36] performed an analysis of the influence of the non-uniformity of

the electric field in the corona threshold. Numerical methods regarding the solution of the Boltzmann equation in the case of homogeneous and non-homogeneous electric fields have been investigated by Anderson et al. in [37]. Moreover, they have developed numerical methods for the determination of the onset in the case of complex geometries like resonators [37].

From all this know-how, it is concluded that the accuracy in the prediction of the threshold depends on three main factors. First of all, the experimental determination of the contribution of each physical mechanism involving corona in a particular gas for any environment conditions. Secondly, in the case of complex structures, the numerical computation of the electromagnetic field distribution inside the components. And finally, the evaluation of the free electron density evolution inside a particular device using the aforementioned experimental data and the electromagnetic field distribution in the component.

Therefore, the main aim related to corona discharge has been to create a tool capable to predict the corona breakdown threshold in microwave components, in particular, in complex rectangular waveguide structures like filters or resonators. To do this, resort had to be taken to a software tool able to determine the electromagnetic fields distribution inside of any rectangular component. The existing software tool *Full-wave Electromagnetic Simulation Tool* (FEST), version 3.0 developed by ESA/ESTEC under Contract No. 12465/97/NL/NB in order to efficiently calculate the Scattering Parameters of complex structures was updated within the ESA/ESTEC activity "AO-4026 ITT ESA - Multipactor and Corona Discharge: Simulation and Design in Microwave Components" (Contract No. 16827/02/NL/EC) for the computation of the electromagnetic field in rectangular waveguide geometries. In this thesis, this software has been employed in order to predict the corona discharge onset. The agreement among the simulation results and the experimental data validates the approach followed.

This thesis is structured as follows: Chapter 2 is devoted to the description of metal-to-metal contacts for its application to waveguide connections. In Chapter 3 a full model for the computation of the Passive Intermodulation level at waveguide junctions is developed and theoretical results are analysed. Chapter 4 is dedicated to present the experimental results obtained for waveguide connections. In Chapter 5 the basics of the corona phenomenon are described whereas in Chapter 6 the corona discharge breakdown threshold is computed in terms of different system parameters. Experimental data together with the computed corona breakdown onsets are presented in Chapter 7. Finally, Chapter 8 summarises the work performed and proposes future research in these fields.

Chapter 2

Metal-to-Metal Contacts

Metallic contacts have been object of study since the middle of the last century [38,39]. Indeed, due to their importance and complexity, they still generate many scientific works every year regarding different aspects like surface/contact characterisation [40–47], contact resistance [48–52], or ageing [53, 54]. Today applications like microelectromechanical systems (MEMS) [55] need a realistic description of metallic contacts and their properties. In this chapter, the important aspects of metal-to-metal contacts are described and, in particular, those features which are applicable to waveguide junctions are investigated in more detail.

First of all, a surface model is described as well as the mechanical approach chosen for the calculation of the contact area as a function of the mechanical applied load. Following this, an electrical contact model between rough surfaces separated by a thin dielectric film is described. Moreover, possible PIM physical sources in realistic metallic contacts are described. In particular, tunnelling and thermionic emission in Metal-Insulator-Metal (MIM) structures are considered. Finally, temperature concepts affecting the contact are summarised in the last section of the chapter.

2.1 Topographical and Mechanical Characterisation of Engineering Surfaces

Surfaces topography is of high importance in the response of a metal-to-metal contact system. As a matter of fact, surfaces are never perfect. They present different kind of imperfections like roughness, waviness, among others. Along the years, the scientific community has classified these imperfections and has defined general-purpose parameters in order to describe arbitrary surfaces. All these aspects, as well as experimental techniques used to quantify the surface parameters can be found in the American National Standard for surface texture (surface roughness, waviness and lay) [56].

On the other hand, the mechanical response of a two-surface contact is related to the

mechanical properties of the contacting metals themselves as well as the surface topography. Basically, a mechanical contact can be in three well-differentiated deformation regimes: elastic, elastoplastic and fully plastic. A particular contact is in one or another state depending on the surface finishing (the rougher the surface, the more plastic is the contact), on the mechanical properties of the metals and on the applied mechanical load (the higher the load, the higher the probability to trespass the elastic regime of the contacting metals). This is a key feature since the more plastic the contact, the less mechanical load is needed to have a large area of contact.

It is therefore clear that one needs a surface model as well as a mechanical model in order to fully characterise a metallic contact in terms of applied mechanical load, and metal and surface properties.

2.1.1 Surface model

When two surfaces come into close physical contact, the area of contact between them does not correspond to the area of the smallest surface (nominal area). In fact, only a small portion of the surfaces, which is not usually greater than a few percent of the total nominal area, is in real contact. This is due to the roughness of the contacting surfaces, which makes that the real contact only occur at some surface regions (peaks). In order to simulate rough surfaces topography, a large amount of models have been proposed so far [38, 39, 57, 58]. They are generally based on assuming spherical geometry for a single asperity (peak on the surface) and distributing this asperity's height using a random statistical distribution on the surface[39].

Three main random distributions have been employed so far for characterising the surface topography: Gaussian [39], Weibull [59] and Mandelbrot [45]. All of them present advantages and drawbacks:

- the *Gaussian* distribution allows an easy analysis since the two rough surfaces contact system can be sistematically replaced by a flat hard surface in contact with a rough surface of equivalent roughness and mechanical properties. However, non-symmetrical surfaces are not properly characterised using this distribution [1],
- the *Weibull* distribution does not allow a simplified analysis of the problem but non-symmetrical surfaces can be fully characterised,
- the *Mandelbrot* distribution (or one derived from it) results in a fractal geometry. This has the advantage that the surface modelling is size-independent and then, there is no dependence on the experimental data acquisition process. Nevertheless, it is cumbersome to relate the surface measured data to the distribution function parameters.

[1] Parameters like the skewness or the kurtosis of a surface characterise such a kind of surface (see [56]).

Since it has been used in many other works providing reliable results ([39], [60]) and because of its simplified approach, the Gaussian distribution will be the one used throughout this work. Fig. 2.1 shows the contact model used for simulating the metal-to-metal connection. The asperity height (z) distribution is assumed to be Gaussian, l is the interference distance, i.e., the asperity distance that has penetrated into the flat surface, and d is the distance between the flat surface and the asperity's height mean.

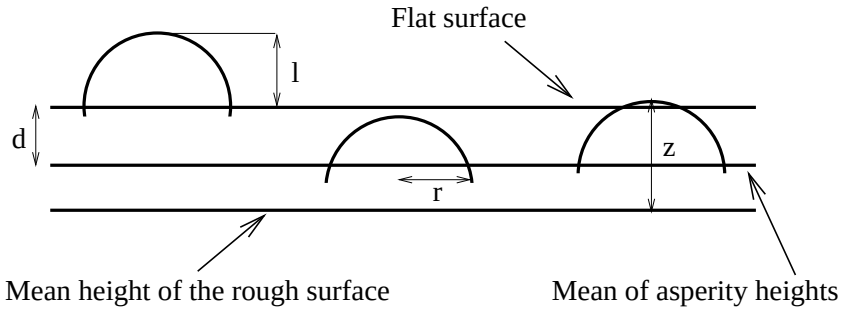

Figure 2.1: *Model for the topography of nominally flat surfaces: one of the surfaces is taken as flat (and infinitely hard) whereas the other is represented by circular asperities above the mean height of the rough surface. A particular asperity is in contact if its height (z) is greater than the distance between the flat surface and the mean height of the rough one.*

In order to characterise the surface, three parameters are used under this model:

- the standard deviation of the surface heights (σ),
- the microasperity density (η),
- the asperity radius (r).

In this case (Gaussian distribution), σ is related to the standard deviation of the surface heights of each surface by:

$$\sigma = \left(\sigma_1^2 + \sigma_2^2\right)^{1/2}$$

The roughness parameter β is defined as:

$$\beta = \eta \sigma r$$

Additionally, σ is related to the standard deviation of the asperity heights (σ_s) by [61]:

$$\frac{\sigma_s}{\sigma} = \sqrt{1 - \frac{3.717 \cdot 10^{-4}}{\beta^2}} \tag{2.1}$$

and σ_s is related to the average roughness (R_a) [56] by:

$$\sigma_s = \left(\frac{\pi}{2}\right)^{1/2} \cdot R_a \tag{2.2}$$

In this way, the roughness parameter directly obtained from the measurements (R_a) is related to the parameter used by the model (σ).

2.1.2 Mechanical model

Once the surfaces in contact have been fully characterised, a mechanical model of the contact has to be developed which provides the deformation characteristics under mechanical load. Different mechanical models have been proposed so far [38, 42, 62, 63]. In particular, the Greenwood and Williamson model [39] (GW model in the following) is adopted here. The basic assumptions of this model are:

- Isotropy of the rough surface,
- the asperity summits have the same radius of curvature but their heights are varied randomly,
- the asperities do not interact among themselves,
- only the asperities are deformed; no bulk deformation can occur.

As mentioned, thanks to the Gaussian distribution of the surface, it can be shown [64] that the contact between two rough surfaces is equivalent to the contact between a hard surface (infinite Young's modulus) and a rough surface of equivalent Young's modulus (E') given by:

$$\frac{1}{E'} = \frac{1-\nu_1^2}{E_1} + \frac{1-\nu_2^2}{E_2} \tag{2.3}$$

where E_1, E_2, ν_1 and ν_2 are the Young's moduli and the Poisson's ratios of the two contacting metals.

The deformation distance of each microasperity is defined as l (as Fig. 2.1 shows) and its average $\overline{l}$ over the whole surface is:

$$\overline{l}^* = \int_{d^*}^{\infty} (z^* - d^*) \cdot \phi^*(z^*) dz^* \tag{2.4}$$

where the asterisk means from now on that the quantity has been divided by σ (in order to deal with dimensionless entities), and ($\phi^*(z^*)$) is the Gaussian distribution of the asperity heights, i.e.:

$$\phi^*(z^*) = \frac{1}{\sqrt{2\pi}} \frac{\sigma}{\sigma_s} \exp\left[-0.5 \cdot \left(\frac{\sigma}{\sigma_s}\right)^2 (z^*)^2\right] \tag{2.5}$$

For each microasperity, the transition among the different deformation regimes (elastic, elastic-plastic and plastic) depends on the microasperity interference distance l. Indeed, a critical interference (l_c) is defined which provides the transition between the elastic and the elastic-plastic regimes [65]:

$$l_c = \left(\frac{\pi K H}{2E'}\right)^2 r \tag{2.6}$$

where:

K= 0.454 + 0.41·ν (ν is the Poisson's ratio of the softer material) [66], and

H is the hardness of the softer material.

It is clear that the critical deformation distance of one single microasperity only depends on the mechanical properties of the contacting materials (H, E', ν) and its geometrical aspect (r). Moreover, this critical distance is independent of the surface properties (η, σ). These properties, however, strongly affect the average deformation distance which value respect to l_c provides the kind of deformation that dominates the surfaces contact for a determined applied mechanical load.

Additionally, the plasticity of a contact is related to the roughness and to the mechanical properties of the contacting materials. A plasticity index is defined as [39]:

$$\Psi = \frac{2E'}{\pi K H}\left(\frac{\sigma_s}{r}\right)^{0.5} \tag{2.7}$$

This parameter governs the mechanical response of rough surfaces contacts. The higher the Ψ, the more plastic is the contact. However, the plasticity index has the disadvantage of considering surface characteristics and material properties altogether. Hence, in order to characterise the surface plasticity regardless of the particular metal, the part of Ψ dependent only on the surface parameters can be taken. Thus, we can define:

$$\overline{\Psi} = \left(\frac{\sigma_s}{r}\right)^{0.5} \tag{2.8}$$

Therefore, contacts between surfaces of the same shape but different metals can be compared by means of $\overline{\Psi}$. This is very useful if the effect of applying coatings on metal surfaces is investigated since, in most cases, the surface topology is not modified but the mechanical properties are.

Another important parameter is the number of microasperities in contact, which can be computed by [60]:

$$N_c = \eta A_n \int_{d^*}^{\infty} \phi^*(z^*) dz^* \tag{2.9}$$

where A_n is the nominal area of contact.

The GW model is restricted to the elastic regime case. The fully plastic regime has also been taken into consideration by other authors (see for instance [57]). Moreover, the intermediate elastic-plastic regime has been investigated [65] despite the fact that no analytical results can be provided.

In the following, the three different deformation regimes are analysed and a recent result [60], which is valid for the whole deformation spectrum, is presented.

Elastic deformation

The elastic deformation regime takes place when the major part of the contacting microasperities are elastically deformed in such a way that, if the surfaces are separated, the original profile is recovered. The critical deformation interference parameter l_c provides information about this. For a single microasperity, if the deformation distance $l = z - d$ is lower than this parameter, elastic deformation occurs.

In the case of one single asperity of radius r, the solution to the problem is given by the so-called Hertz theory [67]. The applied mechanical load as a function of the deformation distance is:

$$L = \frac{4}{3} E' r^{1/2} \cdot l^{3/2} \tag{2.10}$$

whereas the area of contact becomes:

$$A = \pi r l \tag{2.11}$$

If a complete surface is considered, the applied mechanical load can be found generalising (2.10) by using the Gaussian distribution:

$$L = \frac{4}{3} E' r^{1/2} \eta A_n \int_{d^*}^{d^* + l_c^*} \sigma^{3/2} (z^* - d^*)^{3/2} \phi^*(z^*) dz^* \tag{2.12}$$

where ηA_n is the total number of microasperities on the surface and the integral only considers those microasperities in physical contact ($z^* > d^*$) which do not trespass the elastic limit ($z^* < d^* + l_c^*$).

Analogously, the contacting area can be found from (2.11):

$$A = \pi r \eta A_n \int_{d^*}^{d^* + l_c^*} \sigma (z^* - d^*) \phi^*(z^*) dz^* \tag{2.13}$$

Hence, the mechanical contact is in full elastic deformation regime when the major part of the microasperities are not deformed beyond the critical interference distance.

Fully Plastic deformation

Fully plastic deformation occurs if l is well above l_c. In this case, the major part of the microasperities are deformed plastically, not recovering their original shape once the surfaces are separated. The applied load and the area of contact for the case of a single asperity yields

$$L = 2\pi r H \cdot l, \tag{2.14}$$

$$A = 2\pi r l, \tag{2.15}$$

where it is noticeable the fact that the applied mechanical load and the area of contact are just related by H ($L = A \cdot H$).

Generalising again for the multiasperity case, the total applied mechanical load and the total area of contact are:

$$L = 2\pi r \eta A_n H \int_{d^*}^{\infty} \sigma(z^* - d^*)\phi^*(z^*)dz^* \tag{2.16}$$

$$A = 2\pi r \eta A_n \int_{d^*}^{\infty} \sigma(z^* - d^*)\phi^*(z^*)dz^* \tag{2.17}$$

Elastoplastic deformation

An analytical formulation is not possible for the intermediate case between fully plastic and elastic deformation. Several authors have investigated this regime [43,44,46,58,63,65]. The Finite Elements Method (FEM) has been used by many of these and other authors in order to derive phenomenological expressions of general purpose.

In this work, the FEM solution recently developed by Kogut and Etsion is adopted [60] since they have given constitutive relations for the dimensionless real contact area ($A^* = A_{real}/A_n$) and the dimensionless applied load ($L^* = L_{real}/(A_n \cdot H)$) as a function of the surfaces separation d^* for all the ranges of deformation:

$$\begin{aligned} L^* = \frac{2}{3}\pi\beta K l_c^* \Big[& \int_{d^*}^{d^*+l_c^*} K^{1.5} + 1.03 \int_{d^*+l_c^*}^{d^*+6l_c^*} K^{1.425} \\ & + 1.4 \int_{d^*+6l_c^*}^{d^*+110l_c^*} K^{1.263} + \frac{3}{K} \int_{d^*+110l_c^*}^{\infty} K^1 \Big] \end{aligned} \tag{2.18}$$

$$\begin{aligned} A^* = \pi\beta l_c^* \Big[& \int_{d^*}^{d^*+l_c^*} K^1 + 0.93 \int_{d^*+l_c^*}^{d^*+6l_c^*} K^{1.136} \\ & + 0.94 \int_{d^*+6l_c^*}^{d^*+110l_c^*} K^{1.146} + 2 \int_{d^*+110l_c^*}^{\infty} K^1 \Big], \end{aligned} \tag{2.19}$$

where K^β is given by:

$$K^\beta = \left(\frac{l^*}{l_c^*}\right)^\beta \phi^*(z^*)dz^* \tag{2.20}$$

The expressions for A^* and L^* are given as a sum over the separation distance in four different ranges. This is done to appropriately fit the numerical result to an analytical formula. The first integrals in (2.18) and (2.19) reproduce the results of (2.12) and (2.13) respectively. On the contrary, the last integrals in (2.18) and (2.19) coincide with (2.16) and (2.17) if the deformation interference is always much larger than its critical value, and then, the major part of the deformation distances are over $110\ l_c$. The two intermediate integrals take into account the elastoplastic regime because two ranges have become necessary to properly fit the result of the FEM simulation. The main advantage of this formulation consists in the possibility of having an accurate description of the elastoplastic regime without being obliged to perform a heavy numerical simulation like the one resulting from a FEM scheme.

Relations (2.18) and (2.19) provide the applied mechanical load and the real area of contact as a function of the surfaces separation. They can be directly related to each other just by taking their values for the same surface separation. Following this procedure, the contact surface change is known as a function of the applied load.

Fig. 2.2 shows the dimensionless applied mechanical load versus the dimensionless surface separation where the three deformation regimes have been differentiated.

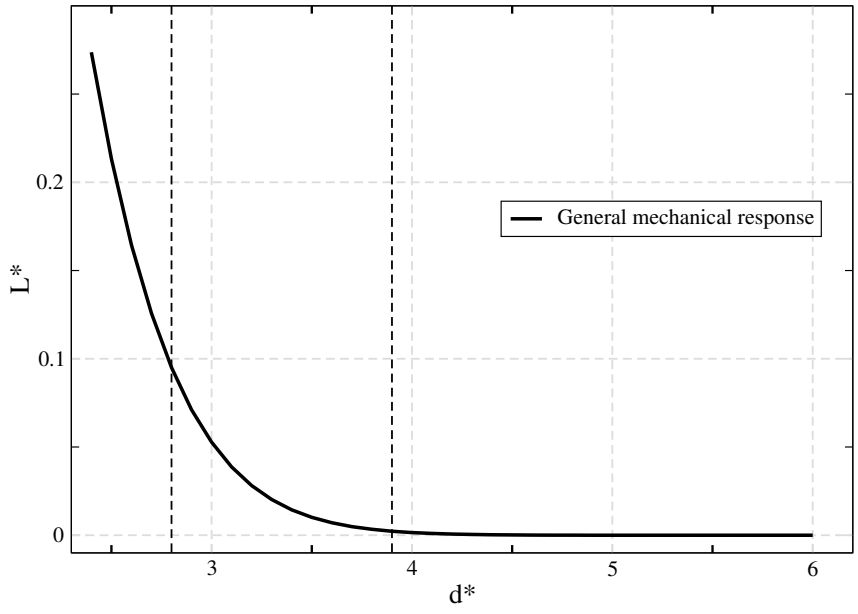

Figure 2.2: *Dimensionless load as a function of the dimensionless surfaces separation. The three regimes are shown. The right side belongs to the elastic regime. The left part shows the fully plastic regime, and in the centre, the transition between both regimes takes place (elastoplastic regime).*

On metal surfaces, oxides and contaminants are always present. Therefore, one could

expect some mechanical influence of such a layer. However, since this layer is much thinner than the typical roughness of engineering surfaces [68], the mechanical properties of the base metal dominate the full mechanical response. Thus, in all the calculations that follow, the mechanical properties taken are those of the contacting metals. Otherwise, a multilayered mechanical system should be considered [69–71] which would introduce a higher degree of complexity.

2.2 Electrical contact of metals separated by a thin dielectric film

As analysed in the previous section, due to the surface imperfections, the metal-to-metal connection only occurs at some points. Therefore, when a current has to flow through the connection, the current lines at the contact deform themselves in order to search the regions of lower resistance. Fig. 2.3 displays this feature schematically. This constriction of the current results in the generation of the well-known constriction resistance [38].

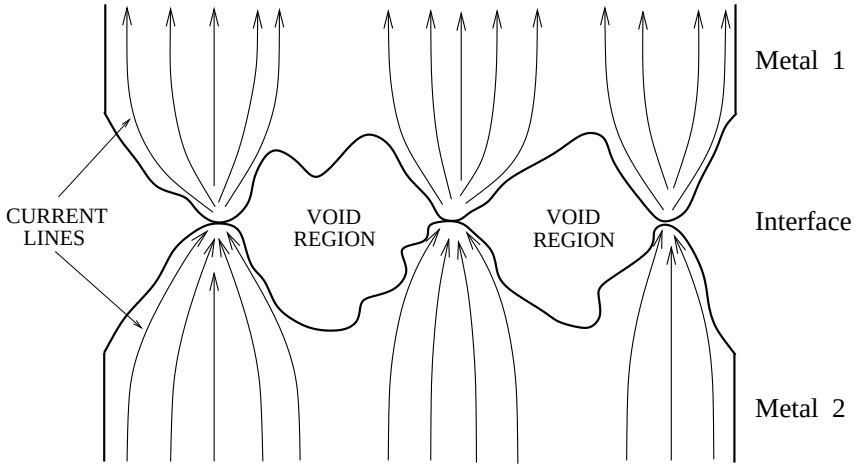

Figure 2.3: *Current lines at a metallic junction.*

If an oxide layer is covering the metals' surfaces, a film resistance is also present at the contact. Moreover, a contact capacitance appears at the junction due to the presence of this layer between the metallic surfaces.

Two main situations can take place when metal surfaces are joined. On the one hand, it is possible that no real metal-to-metal contacts (also called a-spots) exist and then all the contact zones are separated by a thin dielectric layer. On the other hand, it can occur that in the contact zones, a-spots are formed due to the rupture of the dielectric layer by

the base metal.

The presence of one or the other situation depends on a large amount of parameters. Obviously, as the mechanical load between the metals increases, the probability of rupture of the covering layer increases as well. In the same sense, if the oxide layer is extremely thin and/or brittle, the rupture occurs for lower loads. Additionally, the peakiness of the surfaces can also impact the rupture ratio, since the microasperities penetrate more in the opposite metal. In fact, rough surfaces with a high degree of peakiness normally present a lower contact resistance than smoother surfaces with rounded finishing due to this facility for breaking the covering layer.

2.2.1 No Metal-to-Metal contacts case

The electric contact between metals separated by a dielectric layer is analysed in this section. The analysis consists basically in the calculation of the contact resistance and capacitance at the connection.

As Fig. 2.3 shows, in a metallic contact two main regions can be clearly differentiated: the contacting zones between the surfaces and the void regions where no physical contact exists. Increasing the mechanical load, the number of contacting regions and their size also rises. In other words, the area of contact increases. Electrically, both regions are clearly different. The void regions, which have a size comparable to the roughness of the surfaces, are mainly dominated by the vacuum (or air), whereas the contacting regions are separated by a thin dielectric layer formed, in a large extent, by the native metal oxide and contaminants like oxygen or carbon.

Fig. 2.4 displays the equivalent circuit used to simulate metal-to-metal systems when no rupture of the covering layer occurs. The two capacitors have their origin in the displacement currents both in the void regions (C_{n-c}) and in the contacting zones (C_c). In the void regions, the capacitance is the sum in series of two contributions: the air capacitance of thickness *d-s* and the insulator capacitor of thickness *s*. However, since the insulating layer is only few nanometres thick [72] and the separation between engineering surfaces is typically of the order of few micrometres [68], the contribution of the dielectric layer to the non-contact capacitance can be neglected [73].

The circuit of Fig. 2.4 shows the contact effective capacitance and the non-contact effective capacitance. Each one is the sum of the parallel capacitances in all the void regions and in all the contact zones respectively. The effective non-contact capacitance is just

$$C_{n-c} = \frac{\varepsilon_0 A_n (1 - A^*)}{d}, \tag{2.21}$$

where $A_n(1-A^*)$ is the non-contacting total area. In the same way, the effective contact

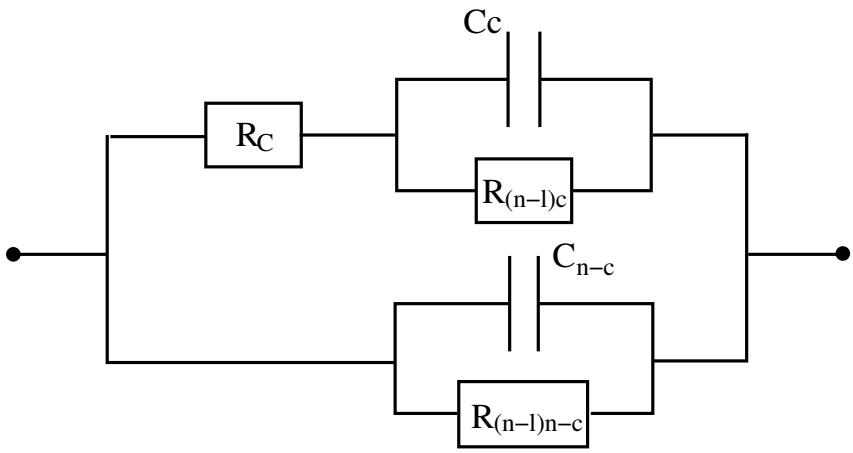

Figure 2.4: *Equivalent circuit of a metal-to-metal contact in the case that no a-spots are formed.*

capacitance is computed using

$$C_c = \frac{\varepsilon A_n \cdot A^*}{s}, \tag{2.22}$$

where ε is the permittivity of the dielectric layer and s its thickness.

It is clear that, for low contact areas (low applied mechanical load), the dominant capacitance is the non-contacting one whereas C_c dominates at high loads. This is graphically shown in Fig. 2.5. The effective non-contact capacitance is almost load independent. This is easy to understand by inspection of (2.21). Both, the surfaces separation and the non-contact area decrease slowly as the load increases. In fact, the small increase is due to the small reduction in the surfaces separation, since the non-contact area variation is negligible. However, the effective contact capacitance strongly increases as the load rises. In (2.22) it is seen that the only load-dependent quantity is the area of contact which sharply increases with the load.

For each capacitance, a non-linear resistance in parallel has been included. These resistances are the PIM sources in the void regions and in the contact zones (film resistance). Of course, these resistances are much larger than the other resistances in the circuit since, otherwise, their impact would be much larger than observed. For instance, higher PIM levels would be generated and not the typical range between -20 and -150 dBm for a combined input power of 50 dBm. This is extremelly important since it allows the simplification of the problem by splitting it in two steps: first, calculating all the linear elements in the circuit, and then, determining the non-linear response. Among the physical sources of these resistances (which are the PIM sources), tunneling, thermionic emission, Poole-Frenkel effect, etc.. can take place in the contact zones whereas in the void regions, mechanisms like field emission or gas breakdown (corona) can occur.

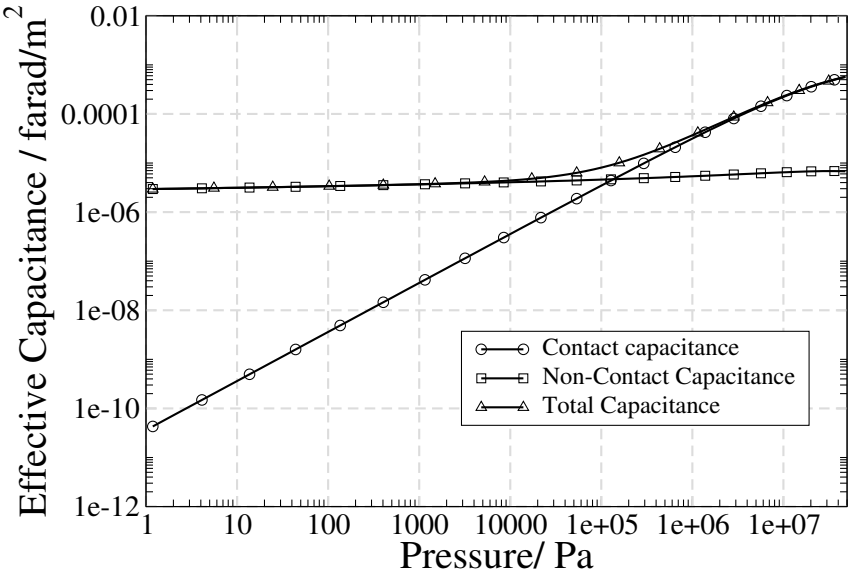

Figure 2.5: *Contribution of each capacitance and the total capacitance in the case in which no a-spots are formed.*

Finally, the last element in the circuit is the envelope constriction resistance R_C [38]. This resistance is microcontact size dependent. Indeed, depending on its size two different mechanisms can occur: Sharvin or Holm.

The Sharvin mechanism [74] dominates the constriction resistance if $R < \lambda$, where R is the radius of the asperity contact and λ is the average electron mean free path, whereas the Holm mechanism [38] is predominant if $R > \lambda$. In Sharvin's case, the electrons travel balistically in the contact whereas if the Holm mechanism prevails, the electrons diffuse from one metal to another. Mikrajuddin et al. [75] have derived a general expression for the constriction resistance in any range:

$$R_c = \frac{4(\rho_1+\rho_2)\lambda}{9r} + \frac{\rho_1+\rho_2}{2\pi R}\int_0^\infty \exp(-x\lambda/R)\frac{\sin(\pi x)}{\pi x}dx \tag{2.23}$$

where ρ_1, ρ_2 are the specific resistivities of the contacting surfaces.

In our application, the Holm mechanism is considered as the cause of this resistance, since, under normal conditions, the radius of the microcontacts at the microasperities are larger than the average electron mean-free path of the electrons in the metals. In this case, the envelope constriction resistance for one single microasperity is [38]:

$$(R_C)_i = \frac{(\rho_1+\rho_2)}{4R} \tag{2.24}$$

where ρ_1, ρ_2 are the specific resistivities of the contacting surfaces. In the case of N_c microasperities, the resulting resistance is the sum of the individual parallel resistances.

An average radius ($\overline{R}$) can be extracted from the contact area and the total number of microasperities in contact:

$$\overline{R} \approx \left(\frac{A_n A^*}{\pi N_c} \right)^{1/2} \tag{2.25}$$

And then, for the case of N_c microasperities in contact, R_C can be approximated by:

$$R_C \approx \frac{(\rho_1 + \rho_2)}{4 N_c \overline{R}} \tag{2.26}$$

Fig. 2.6 shows this resistance together with the impedances of the two capacitors as well as the total impedance of the circuit of Fig. 2.4. At low applied mechanical loads, the dominant term is the resistance of the non-contact capacitor since, in this case, this resistance is much smaller than the contact capacitor resistance and the envelope constriction resistance. As the load increases, the dominant resistance is the contact resistance due to the fact that it is much lower than the non-contact resistance. It can be noticed that the envelope constriction resistance can be neglected in front of the other resistances in the circuit since it is not relevant at any applied load regime.

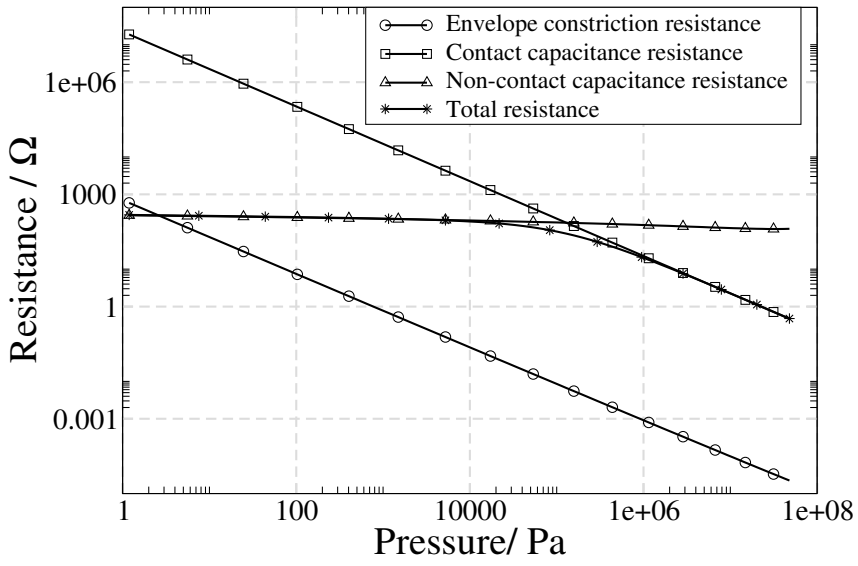

Figure 2.6: *The three resistances in circuit of Fig. 2.4 and the total equivalent resistance.*

2.2.2 Metal-to-Metal contacts case

In this situation, the circuit of Fig. 2.7 is used for simulating the system behavior instead of the circuit of Fig. 2.4. The only (and critical) difference is the appearance of a constriction resistance which, as in the case of the envelope constriction resistance, is due to the change in the direction of the current lines which now occurs in the a-spots,

i.e., inside each microasperity in contact several a-spots appear through which the current flows.

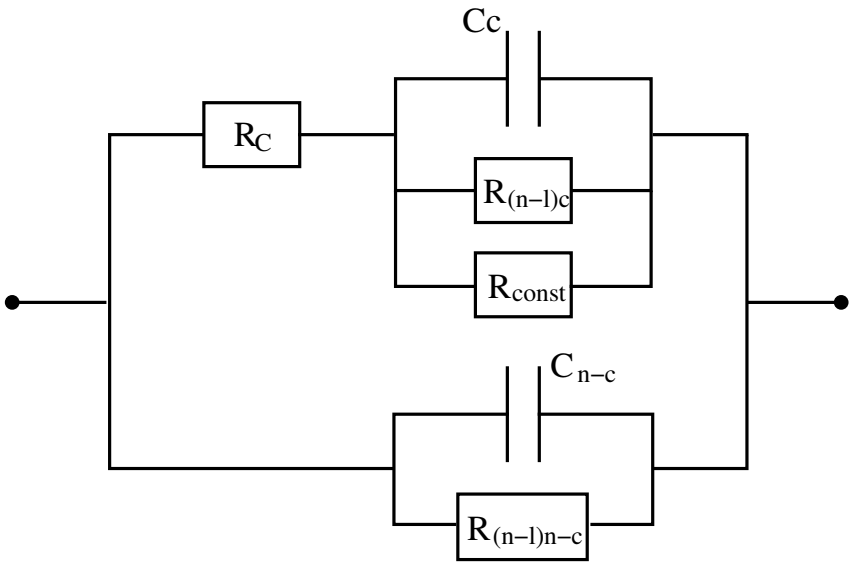

Figure 2.7: *Equivalent circuit in the case of MM contact in the microasperities.*

The constriction resistance in this case is similar to (2.24) but now the radius corresponds to the a-spot radius. A cracking function, which provides the cracking rate of the dielectric layer as the force is increased, is needed. The cracking phenomenon is very dependent on small irregularities on the surfaces and/or of the covering dielectric layer. Therefore, a full theoretical model capable to predict such a phenomenon does not exist. However, some qualitative aspects can be addressed following the existing literature: if the base metal is soft, the covering layer can be easily displaced [76]. Moreover, if the hardnesses of the base metal and the covering layer are similar, the probability of rupture also increases [77]. Additionally, it is obvious that the thinner the covering layer is, the lower the force needed to rupture it [53]. This knowledge helps to create phenomenological expressions in order to model the covering layer cracking.

Therefore, in the present work, a simple cracking profile which has to obey some basic characteristics is postulated:

1. It must be an increasing function with the applied force.

2. No significant cracking occurs at low applied forces.

3. At extremely high loads, almost all the area of contact are indeed MM contacts (perfect Ohmic contact).

4. It must be related to the thickness of the insulating layer and the microasperities deformation.

The pressure threshold value (or any related parameter) needed to make the cracking appear will be dependent on the oxide/contaminants - metal junction characteristics, like microhardness difference or layer thickness. Malucci [53] has pointed out that, after some assumptions, the cracking is basically dependent on l/s in such a way that, if the deformation is lower than the insulating thickness, no cracking can occur. However, we do not assume this since the average deformation $\bar{l}$ will be used as parameter and therefore, even if this parameter is lower than s, cracking can take place. The expression is:

$$A_{MM} = A_n A^* \cdot \left(\frac{\bar{l}/s}{1+\bar{l}/s} \right)^{\alpha} \tag{2.27}$$

where α (cracking factor) is a parameter that indicates how fast the MM regions grow with the applied force. This parameter is unknown and has to be calculated using an indirect method, like for example, the measurement of the contact resistance. This simple function fulfils the requirements above mentioned and relates the cracking mechanism to the averaged value of the surface penetration of the rough surface into the flat one and the covering layer thickness, which has a clear physical meaning. Fig. 2.8 shows the cracking function for different values of the cracking factor. It is clearly appreciated that the larger the cracking factor, the lower the cracking ratio.

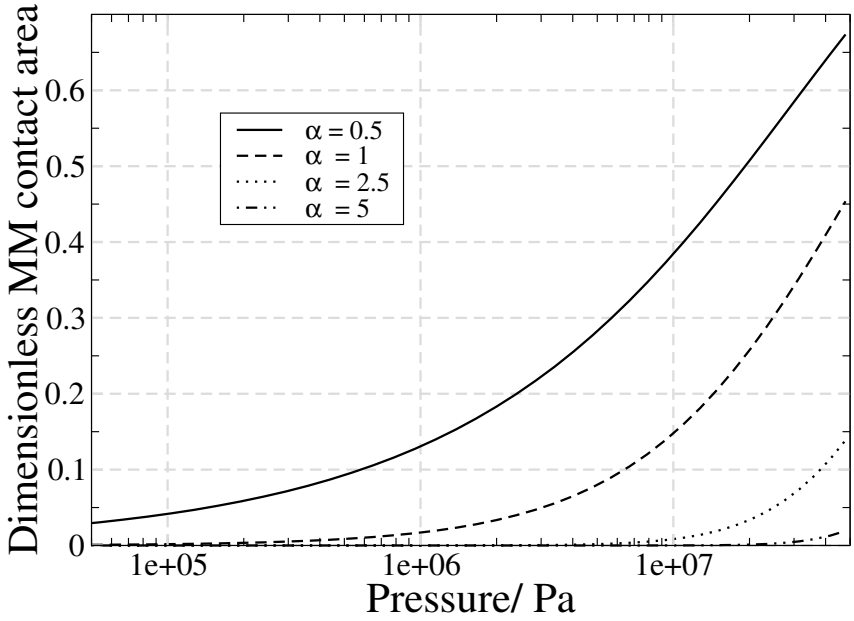

Figure 2.8: *Dimensionless real MM contact area for different values of* α.

The calculation of the constriction resistance (R_{const} in circuit of Fig. 2.7) from the total area of all the a-spots is not direct. Indeed, the constriction resistance for one microasperity where N_a a-spots are present is analog to (2.26)

$$(R_{const})_i \approx \frac{(\rho_1 + \rho_2)}{4N_a\overline{a}_{spot}}, \tag{2.28}$$

where $\overline{a}_{spot}$ is the average radius of all the circular a-spots in one single microasperity. For N_c microasperities, the total constriction resistance is

$$R_{const} \approx \frac{(\rho_1 + \rho_2)}{4N_cN_a\overline{a}_{spot}}. \tag{2.29}$$

From (2.27), and assuming that the N_a a-spots behave like an effective single a-spot, the value of $N_a a_{spot}$ can be obtained in the same way as in (2.25), i.e.

$$R_{const} \approx \frac{(\rho_1 + \rho_2)}{4N_c\left(\frac{A_{MM}}{\pi N_c}\right)^{1/2}}. \tag{2.30}$$

Of course, the expressions developed for the constriction resistance will not provide a high accuracy. Nevertheless, the objective is to find the correct dependence of the contact on parameters like the contact area or the degree of cracking and therefore, this approximated analysis is justified.

2.3 Non-linear response

The non-linear response of the system finally results in the excitation of the intermodulation products. Two well-differentiated kinds of regions can excite the PIM level in a waveguide junction: the void regions and the contact zones separated by a thin dielectric film.

For the case of very low applied forces, the surfaces are almost separated and therefore, all the PIM level is likely to occur in the void regions. This case has been experimentally investigated in [78] although no conclusions about the PIM source mechanism have been reported. In that investigation, some kind of dependence of the PIM level on the ambient pressure was observed. Due to the shape of the curve, an ionisation mechanism like Corona Discharge (which is fully explained in the second part of this thesis) could be proposed as possible physical PIM source. In fact, the Corona Discharge is usually detected, among other detection methods, by measuring the excited harmonics, what finally is the same as saying that IM products are also excited in the multicarrier case.

However, if the applied mechanical pressure is increased, it is very likely that the main source of intermodulation occurs in the contact zones since a high number of contacting

zones exist. Due to the fact that waveguides are joined with high mechanical loads, in this work only the contact zones are investigated as possible PIM source regions from the physical point of view. In fact, in the experimental tests presented in chapter 4, it will be seen that, at low contact pressures, the PIM sources seem to be located in the void regions (generated by large waviness of the waveguide flanges), but that when the pressure is increased, the intermodulation level is generated at the contact zones.

In this case, the main intermodulation sources can comprise several contributions like tunneling, thermionic, Poole-Frenkel and more [5], [79]. Electron transport mechanisms which can occur in Metal-Oxide-Metal structures are described in the following sections. In particular, tunneling and thermionic emission are analysed as possible PIM physical sources. Moreover, the insulating case as dielectric layer is investigated since it is the most common situation for metal oxides.

2.3.1 Tunneling theory & Thermionic emission

Two physical mechanisms occurring in metallic contacts separated by a thin insulating layer are taken as possible PIM sources: tunneling effect and thermionic emission. Both phenomena are highly non-linear what can result in the excitation of measurable PIM levels.

Tunneling theory

One of the most important consequences of quantum theory is the tunnel effect [80,81]. Electrons from one metal can *tunnel* across a classical forbidden region to another metal if the distance between them is small enough.

If no bias (voltage) is applied, the net current flow is zero because the currents from one metal to the other are the same but in opposite directions since the Fermi level of both metals coincide, provided the system is in thermal equilibrium [82]. If a voltage V is applied between the metals, a difference of eV between the two Fermi energy levels appears and the barrier becomes trapezoidal in shape. As the voltage raises, the tunnel probability increases because the total area of the barrier decreases, i.e., the tunnel probability is dependent on the barrier surface.

The value of the barrier height is, basically, the difference between the work function of the metals and the electron affinity of the insulator [83]. Thus, the insulator fundamentally reduces the barrier height with respect to the metal-vacuum-metal case where the barrier height is just the work function of the metal.

Studies of the tunnel current in Metal-Insulator-Metal (MIM) structures spread out from the last century until nowadays [84–89]. Presently, there is still a lot of interest in this structure and new models to tackle the problem frequently emerge [90], [91]. These

new approaches try to improve the previous results by applying new methods for the resolution of the Schrödinger equation in a many particle system. Though these schemes are very interesting, they do not provide more knowledge from the practical point of view.

The tunnel current between the metals can be calculated using the Simmons equation [86] for direct tunneling in MIM structures which is based on the WKB approximation. The volume tunnel current density is non-linear and voltage dependent:

$$J(V) = \left(\frac{6.2\times10^{10}}{\Delta s^2}\right)\left(\phi_I exp[-1.025\Delta s\phi_I^{1/2}]\right. \\ \left. -(\phi_I+V)exp[-1.025\Delta s(\phi_I+V)^{1/2}]\right) \tag{2.31}$$

where:

$$\phi_I = V_0 - \frac{V(s_2+s_1)}{2s} - \frac{2.88}{\varepsilon(s_2-s_1)}\ln\frac{s_2(s-s_1)}{s_1(s-s_2)}, \tag{2.32}$$

s is the barrier width (insulating thickness) without considering the image force effect [79], s_1 and s_2 are the turning points of the tunneling barrier which define the effective barrier width $\Delta s = s_1 - s_2$, different from s due to the aforementioned effect, V_0 is the barrier height and V is the applied voltage. The values of s, s_1, s_2 and Δs are given in Angstrom and ϕ_I in Volts.

This expression is accurate for low and intermediate voltages ($V \leq V_0$). For higher voltages, where the tunneling practically becomes a field emission problem, resort must be taken to the Fowler-Nordheim formula. However, in this application, the use of the Simmons equation is sufficient since no high voltages are generated at the junction.

Thermionic emission

In a MIM structure, the thermionic emission current [92] is determined by the electrons that flow from one metal into the other *overcoming* the potential barrier. The thermionic current in MIM structures can be obtained easily. All the necessary steps can be followed in reference [93] and here only some highlights are given.

In a metal-vacuum interface, the current of electrons that overcome the work function of the metal is given by the Richardson-Dushman equation:

$$J_T = AT^2 e^{\frac{-W}{kT}} \tag{2.33}$$

where:

- W is the work function of the metal.
- $A = 4\pi mek^2/h^3$.

being m and e the mass and the charge of the electron, k the Boltzmann constant and h

the Planck constant.

In the case of two metals, there are two currents flowing in opposite directions, and then, the total current is the difference between them:

$$J_T = AT^2\{e^{\frac{-\varphi_1}{kT}} - e^{\frac{-\varphi_2}{kT}}\} \tag{2.34}$$

The work function has been substituted by the height of the barrier at each metal-insulator interface. If both metals are the same, then $\varphi_1 = \varphi_2$ and the total current is zero. If a voltage V is applied, $\varphi_2 = \varphi_1 + eV$, and hence:

$$J_T(V,T) = AT^2 e^{\frac{-\varphi_1}{kT}}(1 - e^{\frac{-eV}{kT}}) \tag{2.35}$$

It is therefore clear that as voltage increases, thermionic emission also increases because the barrier is lowered. Moreover, the higher the temperature, the higher the thermionic current since more electrons can overcome the barrier.

In principle, one expects that the thermionic emission current does not depend on the thickness of the insulating gap, and only depends on the barrier height because $\varphi_1 = V_0$. However, if the Image force is considered [79], the barrier height is also related to the barrier thickness, and therefore, a dependence of J_T on Δs indeed exists. Finally, following [93], the total thermionic current can be expressed as:

$$J_T(V,T) = AT^2 exp\left\{\frac{[14.4(7 + eV\varepsilon_i s)]^{1/2} - V_0\varepsilon_i s}{\varepsilon_i skT}\right\}(1 - e^{\frac{-eV}{kT}}) \tag{2.36}$$

The final expression of the current corresponds to the sum of tunneling (2.32) and thermionic emission (2.35) currents:

$$J = J(V) + J_T(V,T) \tag{2.37}$$

2.4 Temperature considerations

In this section, temperature effects that affect the PIM response of a junction are briefly described. The importance of temperature can be understood just by considering the high temperature gradient that suffers a satellite in working conditions. In orbit, satellites are exposed to high temperatures when they are lighted by the sun. On the contrary, when the satellite is shadowed by the Earth, very low temperatures are reached. In fact, variations from - 150 ℃ to + 80 ℃ occur. Among others, this is one of the main reasons of the ageing of satellite systems, which results in the fact that a quiet-tested PIM system becomes active during operation.

Mechanical stress

In the case of waveguide junctions, temperature variations can lead to mechanical stress due to the difference in the thermal expansion coefficient between the waveguide metal (usually aluminium) and the bolts (screws), which are normally made of Iron or Stainless Steel [94]. If this happens, the load between the surfaces suffers a cycle along a day. This finally results in an overall increase of the contact resistance due to the ageing of the junction. To avoid this, several options exist. The obvious solution is to isolate thermally the whole system in order to reduce the temperature gradient. To do this, thermal blankets are usually employed in satellites though they do not ensure perfect thermal isolation.

Local Temperature Heating

Apart from the environment temperature, local temperature rises can also take place in any component leading to the excitation of PIM frequencies over the noise level. For instance, resonators which store a large amount of electric energy can heat up the device exciting PIM signals [95]. The PIM excitation in these cases is associated to the linear dependence of the metal conductivity on the temperature, which results in the excitation of harmonic components producing wall currents at the PIM frequency [96]. In the case of waveguide junctions, the appearance of a contact resistance in the metallic contacts leads to the local increase of the temperature in the contact points through the Franz-Wiedemann law which relates the voltage drop at a pure metallic contact (a-spot) to the temperature by means of the electrical and the thermal conductivity

$$T^2 - T_0^2 = \frac{V^2}{4L}, \tag{2.38}$$

where L is the Lorentz number ($L \approx 10^{-8}\ V^2K^{-2}$), which is constant for many metals and is defined as the quotient between the thermal and the electrical conductivities. It is therefore clear the big impact of the contact resistance in the temperature rise of a particular metallic point, since just a voltage drop of 100 mV makes the contact temperature rise from room temperature (300 K) to 580 K. This fact can have several consequences; for instance, the melting point of the contacting metals can be reached and therefore, welding can occur. Or high temperatures can soften the oxide layer making it more prone to rupture, leading to a reduction of the contact resistance of the system. As we will see in the next chapter, this is possibly one of the reasons why the PIM level has lower dependence on the total power than the one predicted by the theory. This is easily understood since the higher the input power, the higher the voltage drop and then, the higher the local temperature at the a-spots, which results in a lower contact resistance and, hence, in a lower PIM level than expected.

Finally, the PIM physical mechanisms can be also temperature dependent. For instance, tunneling is weakly temperature dependent whereas thermionic emission is strongly temperature dependent as shown by (2.35).

Chapter 3

Passive Intermodulation Computation

In the previous chapter, a model for characterising the electrical contact between two general metallic rough surfaces separated by a thin dielectric film has been described. Now, this approach is going to be generalised for the case of a rectangular waveguide connection where the waveguides are assumed to be made of a perfect conductor and, therefore, no losses are included in the calculations. It will be shown that the waveguides junction can be described using the simple equivalent circuits presented in the previous chapter. After doing this, the PIM response is computed by means of two different procedures: a mathematical approach, which only considers one PIM order based on a pure Taylor series, and a physical approach which is based on assuming that tunneling and thermionic emission are the PIM sources in the Metal-Oxide-Metal regions. This second approach allows the study of all the intermodulation orders simultaneously and the contribution of higher orders into the lower ones. Two important dependencies are investigated as well: the PIM variation with the combined power of the input carriers and the dependence with the power ratio between both signals. These computations are relevant in order to understand the experimental results presented in the next chapter.

3.1 Waveguide junction model

In this section, the voltage drop at the waveguide junction is determined for the case in which the whole nominal area is in contact (full contact case) and separated by a thin insulating layer (no a-spots are formed). In order to perform this calculation, the basic electromagnetic equations of a rectangular waveguide are used. Later on, it is seen how the expression obtained can be related to the calculated voltage drop using only the resistance of the contact capacitor of the equivalent circuit of Fig. 2.4. This will allow us to generalise this approach to realistic cases in which no full contact is achieved and a-pots are formed.

Throughout this work, only the case of mono-mode waveguides is considered. This basically means that only the fundamental mode (TE_{10}) can propagate in the waveguide for the frequencies under consideration. Therefore, the electric field inside the waveguide has just one component different to zero: E_y [97, 98]. The modes different to TE_{10}, if excited for any reason, would be evanescent and would reconvert into the fundamental one. This is important since the non-linearities in the system excite both the intermodulation products and the harmonics of the input signals as well as the harmonics of the input modes, i. e., in this case TE_{20}, TE_{30}, etc... If only the fundamental mode is propagating, these excited modes reconvert to it along the waveguide and, thus, they are not relevant for our purposes. On the contrary, if several modes could propagate for the operating frequency, the contribution of each mode should be considered separately when calculating the PIM response. In real applications, waveguides commonly work in the fundamental mode since losses are minimised in this case.

The surface current density $\overrightarrow{j}$ on the walls of a waveguide can be determined from the magnetic field distribution inside the device using [97]

$$\overrightarrow{j} = \overrightarrow{n} \times \overrightarrow{H}, \tag{3.1}$$

with $\overrightarrow{n}$ an orthonormal inward vector to the waveguide walls and $\overrightarrow{H}$ the magnetic field.

The discontinuity in the RF current path occurs in the propagation direction (z-axis). Therefore, it is considered that only this component of the current can excite PIM products. It is likely that the transversal components of the current also generate a certain amount of PIM. However, it is clear that the contribution from the longitudinal current is much more important since its density dramatically increases at the junction because of the reduction of the real area of contact.

For the fundamental mode, longitudinal current exists only on the top and the bottom walls. It can be written as [97]

$$\vec{j}(x,z,t) = -\frac{A_{mn}\beta_z\pi}{\omega\mu_0\varepsilon_0 a}\sin\left(\frac{\pi x}{a}\right)\cdot e^{j(\omega t-\beta_z z)}\overrightarrow{k}, \tag{3.2}$$

being A_{mn} an integration constant related to the square root of the power

$$A_{mn} = 2\varepsilon_0\cdot\sqrt{PZ}\cdot\sqrt{\frac{a}{b}}, \tag{3.3}$$

$\beta_z = \sqrt{\omega^2\mu_0\varepsilon_0 - \left(\frac{\pi}{a}\right)^2}$ the wavenumber inside the waveguide, μ_0 and ε_0 the permeability and the permittivity of the media filling the waveguide, $\omega = 2\pi f$ where f is the signal frequency, a and b the width and the height of the rectangular waveguide, P the input power of the carrier and Z the characteristic impedance of the fundamental mode:

$$Z = \frac{\sqrt{\mu_0/\varepsilon_0}}{\sqrt{1-\left(\frac{1}{2fa\sqrt{\mu_0\varepsilon_0}}\right)^2}}. \tag{3.4}$$

The volume current density on the waveguide walls is obtained from (3.2) following the skin-depth approximation:

$$\overrightarrow{J} = \frac{\overrightarrow{j}}{\delta}, \tag{3.5}$$

where $\delta = \sqrt{\frac{1}{\pi f \kappa \mu}}$ is the skin depth, and κ and μ are the conductivity and permeability of the waveguide metal. The skin depth approximation states that, although the current falls exponentially from the surface of the wall, it can be assumed that the current is distributed constantly on a region limited by the width of the waveguide (only the top and the bottom walls are considered) and the distance to the surface where the current falls a factor $1/e$, i.e., a region of area $(a \times \delta)$.

On the other hand, the volume current density is related to the electromagnetic fields through the Ampere's law

$$\overrightarrow{\nabla} \times \overrightarrow{H} - \frac{\partial \overrightarrow{D}}{\partial t} = \overrightarrow{J}, \tag{3.6}$$

where $\overrightarrow{D} = \varepsilon \overrightarrow{E}$ (with ε is the permittivity of the dielectric) is the dielectric displacement and t is the time. Besides this, the electric field ($\overrightarrow{E}$) is related to the potentials (scalar (V) and vector ($\overrightarrow{A}$)) by

$$\overrightarrow{E} = -\overrightarrow{\nabla} V - \frac{\partial \overrightarrow{A}}{\partial t}. \tag{3.7}$$

Hence, combining (3.6) and (3.7), the voltage drop generated between the two waveguide flanges can be determined by means of

$$V = \int \int_0^s \left(\frac{1}{\varepsilon} \left[J_z - (\overrightarrow{\nabla} \times \overrightarrow{H})_z \right] - \frac{\partial^2 A_z}{\partial t^2} \right) dz\, dt, \tag{3.8}$$

where s is the distance between the two waveguide flanges, in this case, the oxide thickness. In (3.8), only the longitudinal component of the vectors has been considered.

At this point, it is necessary to notice the fact that, for the fundamental mode, the axial components of $\nabla \times \overrightarrow{H}$ and $\overrightarrow{A}$ vanish because are parallel to the electric field, which is transversal. Hence, the voltage drop simply becomes

$$V = \int \int_0^s \frac{1}{\varepsilon} J_z(x,y,z,t) dz\, dt. \tag{3.9}$$

And integrating

$$V(x,y) = \frac{1}{\omega \beta_z \varepsilon} J_z(x,y) |\exp(-j\beta_z s(x,y)) - 1|, \tag{3.10}$$

where $V(x,y)$ is the voltage difference for each point (x,y) in the surface limited by the waveguide width - a - and the skin depth, and s(x,y) is the distance between the two

waveguide flanges for each point (x,y), in this case, the oxide layer thickness.

Assuming that the gap distance is constant through the waveguide and following the skin depth approximation, the voltage drop for any point x along the waveguide width finally is:

$$V(x) = \frac{1}{\omega\beta_z\varepsilon\delta} j_z(x) \left[2 \cdot (1 - \cos(\beta_z s))\right]^{1/2}. \tag{3.11}$$

As seen in (3.2), the surface current density distribution along the waveguide width is given by a sine function and then, it can be written that $j_z(x) = j_z(a/2) \cdot \sin\left(\frac{\pi x}{a}\right)$. Doing this, the voltage drop reads

$$V(x) = \frac{1}{\omega\beta_z\varepsilon\delta} j_z(a/2) \cdot \sin\left(\frac{\pi x}{a}\right) \left[2 \cdot (1 - \cos(\beta_z s))\right]^{1/2}. \tag{3.12}$$

This expression can be simplified in order to reduce it to a simple interpretation. If the dielectric layer between the waveguide flanges is very thin compared to the wavelength, the cosine can be developed until order two, i.e.:

$$\cos(\beta_z s) \approx 1 - \frac{(\beta_z s)^2}{2}$$

In realistic situations, this approach always holds accurate since the typical oxide thicknesses are in the range of few microns [72], whereas the wavelength, in the case of microwave devices, is of the order of centimetres.

Therefore, using this approximation, the voltage drop of (3.12) can be written as

$$V(x) \approx \frac{s}{\omega\varepsilon\delta} j_z(a/2) \cdot \sin\left(\frac{\pi x}{a}\right). \tag{3.13}$$

V(x) is the voltage drop at each point x along the waveguide width. Its average can be obtained just taking the average of the sine function, i.e., $2/\pi$. Hence,

$$V = \frac{s}{\omega\varepsilon\delta} \frac{2}{\pi} \cdot j_z(a/2). \tag{3.14}$$

On the other hand, the total current can be calculated by integration of the surface current *j(x)* along the x-axis

$$I = \frac{2a}{\pi} j_z(a/2) \rightarrow j_z(a/2) = \frac{\pi}{2a} I. \tag{3.15}$$

And thus, the average voltage of (3.14) can be expressed as

$$V = \frac{s}{\omega\varepsilon \cdot \delta \cdot a} I, \tag{3.16}$$

and, since the total considered RF-path area is $a \cdot \delta$, the voltage can be expressed as the current multiplied by the impedance of the contact capacitor (R_c)

$$V = \frac{s}{\omega\varepsilon \cdot A_n} I \equiv R_c \cdot I. \tag{3.17}$$

The voltage has been strictly determined using electromagnetic considerations for the case where full contact is achieved, i.e., without considering the surface roughness of the waveguides themselves and the possible cracking of the layer leading to real MM contacts. A similar expression would have been obtained for the case in which no contact existed at all, and therefore, the voltage drop would have been given by the non-contact capacitor resistance. This connection has been possible because the dielectric layer thickness is much thinner than the wavelength and no magnetic terms affect the voltage drop in the case of propagation with the fundamental mode. Now, we can generalise the voltage drop at the waveguide connection for the rough surfaces case just substituting the contact capacitor resistance in (3.17) by the total effective resistance of circuits of Figs. 2.4 or 2.7

$$V = Z \cdot I, \tag{3.18}$$

where the impedance Z is schematically calculated in appendix A. Of course, the connection must be done changing the general parameters in the impedance expression by waveguide parameters like width or skin depth. Moreover, the current is given by the waveguide surface current.

Finally, one more remark has to be done. In order to compare both approaches, the average value of the voltage along the x-axis has been used. However, for the calculations, the real voltage to take into consideration is the peak voltage, i.e. in this case, the voltage at the centre of the waveguide. Therefore, if the voltage is determined by means of the circuits of the previous chapters, when calculating the PIM response, it has to be multiplied by $\pi/2$. Of course, since the PIM response is a non-linear function, the non-linear current will not follow a sine distribution around the centre point. This behaviour is nothing else than the excitation of higher waveguide modes, which superposition provides the total response. However, since we are assuming that the waveguide ports are very far away from the connection, these modes reconvert to the fundamental one, and thus, the TE_{10} distribution can be taken.

It has been shown that the effective circuits presented in the previous chapter are capable to model the waveguide junction resistance. Next, the way in which this affects the PIM response of the system is described. In order to do it, a PIM model is required. As a consequence, the target of the following sections is to present different PIM models and calculations based on the voltage drop at the connection.

3.2 Passive Intermodulation calculation

In this section, the computation of the PIM level based on the voltage drop of (3.18) is carried out. For the sake of simplicity, we will only consider two monochromatic signals. The study of two signals is enough to provide an understanding of the relevant aspects regarding PIM in waveguide connections. The "in-phase" case results in the worst case possible.

For two frequencies (ω_1, ω_2), the voltage drop at the junction is

$$V(t) = V_1 \sin(\omega_1 t) + V_2 \sin(\omega_2 t). \tag{3.19}$$

The voltage drop amplitudes V_1 and V_2 for both signals are slightly different since they depend on the frequency through the skin depth and through the capacitor impedance (in the case of dominance of the contact resistance by the capacitors). For these reasons, the difference between both voltages increases as the separation between the carriers also increases.

An harmonic balance-like procedure has been followed for the PIM simulation. In few words, the harmonic balance method consists in treating all the linear components of the system in the frequency domain, whereas the non-linearities are analysed in the time domain. The connection between them is performed by means of a Fourier transform in time or frequency domain. This procedure is however simplified because the non-linear currents in the system are negligible compared to the linear ones. This must be always the case because, otherwise, the PIM products generated would have a power of the order of the signals which generate them. For instance, in a two-carrier case with 50 dBm per carrier, typical PIM levels measured are around -20 or -30 dBm in the worst case or, what is the same, around 7 orders of magnitude lower in power. Since the current is proportional to the square root of the power, this means that the linear current is about 6 orders of magnitude greater than the non-linear one. In other words, although the non-linear current affects also the electric response of the junction, its effects can be neglected. As a matter of fact, in the derivation of the voltage drop which lead to (3.18) this assumption was already taken.

To sum up, the resistance (voltage) of the connection is fully dominated by the linear components. Thus, for the computation of the PIM level a linear diagram flow like the one shown in Fig 3.1 has been used.

If the non-linear components can not be neglected, a higher degree of complexity is added. In that case, an iterative procedure must be followed for the correct calculation of the voltage drop (see e.g. [99]).

As shown in the diagram of Fig. 3.1, the non-linear current computation from the voltage drop is the fundamental step for the calculation of the PIM level. Nevertheless,

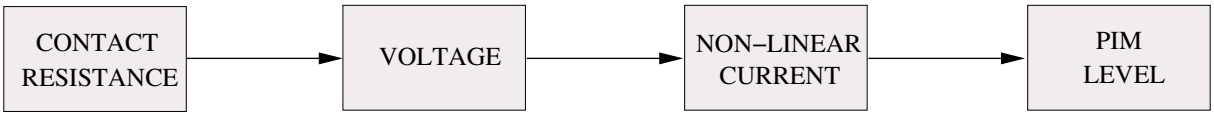

Figure 3.1: *Diagram flow for the calculation of the PIM level.*

two connections are still missing. The non-linear relationship between the current and the voltage, and how to extract from this non-linear current the PIM level. The former is explained in the next sections. The latter is achieved by taking into account that the PIM signals indeed propagate along the waveguide. Therefore, the non-linear current generated by the contact resistance can be directly related to the power of the PIM signal using the fundamental mode equations.

Thus, the PIM signal power can be obtained by means of the fundamental mode expression, just by inverting (3.2), and hence, the PIM level can be expressed as

$$PIM(dBm) = 10\log\left[\frac{P_{int}[J(V)]}{1\cdot 10^{-3}}\right], \tag{3.20}$$

where $P_{int}[J(V)]$ is obtained from (3.2) and (3.3).

It is therefore clear that what defines the PIM signal power is the voltage - nonlinear current relationship. In the next sections, different relationships between them are used. First of all, a purely mathematical approach is followed, which is based in a Taylor expansion of any non-linear relationship regardless its particular aspect. This will allow us to investigate the PIM behaviour with different system parameters. However, this approach is limited to a particular PIM order and thus, no higher order contributions can be considered. Moreover, it is not based in any particular physical PIM source, which makes it useful only from the application point of view. Hence, a second approach is also considered based on a physical scheme where the source of the distortion is tunneling and thermionic emission in MIM connections (see 2.37). The aim of this second approach is to provide physical understanding of a possible PIM mechanism and, additionally, after calibration of a given order, to be able to predict the intermodulation level of the whole PIM spectrum. Moreover, the influence of higher orders into the lower ones can be investigated as well.

3.2.1 Taylor expansion

As already mentioned, the PIM level is excited by a non-linear relationship between the current flowing through the non-linear resistances and the voltage. In a general case, the current can be expressed as a Taylor series of the voltage regardless the particular

shape of the real J-V curve

$$J(V) = \sum_{i=0}^{\infty} a_i V^i. \tag{3.21}$$

In the case of two sinusoidal signals, the voltage is given by (3.19), and then

$$J(V) = \sum_{i=0}^{\infty} a_i \Big[V_1 \sin(\omega_1 t) + V_2 \sin(\omega_2 t) \Big]^i. \tag{3.22}$$

This non-linearity excites the harmonics of the input signals $(2\omega_1, 2\omega_2, 3\omega_1, ...)$ as well as the intermodulation products $(\omega_1 \pm \omega_2, 2\omega_1 \pm \omega_2, ...)$. Normally, but not always, the interesting PIM products are those falling very close to the input carriers. Only the odd PIM orders accomplish this and, hence, the PIM frequencies ($f_{int} = m f_2 + n f_1$) must fulfil that

$$m \neq 0, n \neq 0, \qquad |m| + |n| = i, \qquad m + n = \pm 1.$$

And then, the resulting expression for the current is

$$J(V) = \sum_{i=0}^{\infty} a_i \sum_{\substack{m=-\infty \\ n=-\infty}}^{\substack{m=\infty \\ n=\infty}} \Big[V_1^{|n|} V_2^{|m|} \sin((n\omega_1 + m\omega_2)t) \Big]. \tag{3.23}$$

In (3.23) all the relevant PIM products are considered. If the PIM signal under consideration is a result of a non-linearity of order three, the current can be written as:

$$J(V) = a_3 \Big[V_1^2 V_2 \sin((2\omega_1 - \omega_2)t) + V_2^2 V_1 \sin((2\omega_2 - \omega_1)t) \Big] \tag{3.24}$$

where higher order contributions have been neglected.

In order to use (3.24), the Taylor coefficient a_3 must be known. The only way to do it consists in calibrating the system using a predefined PIM value. In other words, the intermodulation level for a particular set of parameter's values must be known and, from it, the Taylor coefficient has to be determined. Once this has been done, one of the system parameters can be varied and the PIM amplitude determined due to the change in the contact voltage drop. For instance, for a particular applied mechanical load, V_1 and V_2 can be obtained. If the PIM level is known (measured) for this applied pressure, a_3 in (3.24) can be determined. After this, the intermodulation level has been calibrated and can be determined for other applied mechanical loads.

In the following, the PIM level using this approach is obtained as a function of different system parameters. All the results presented in the next pages are, qualitatively, in agreement with the results in the literature on different connection types [9, 10] and with the experimental results presented in the next chapter.

For the analysis, the two input frequencies are 9.75 and 10 GHz. The third order intermodulation frequency chosen is the one which falls in the upper part of the spectrum, i.e., 10.25 GHz. The parameters used for the numerical calculations, if nothing else is explicitly stated, are: $\eta = 94 \cdot 10^{10} m^{-2}$ (number of microasperities per square metre), $R = 10\,\mu m$, $P = 100\ W\ (50\,dBm)$ power of the input signals per carrier, the standard WR90 waveguide, i.e., $a = 0.02286\ m$ and $b = 0.01143\ m$, $s = 4nm$ and $\varepsilon = 4$ in relative units.

The calibration has been done for bulk aluminium (E = 70 GPa, ν = 0.35 and H = 245 MPa) assuming that for $\sigma = 0.5\,\mu m$ and for an applied flange pressure of $6 \cdot 10^4$ Pa, the third order intermodulation level is -100 dBm. Again, if nothing else is written, it is assumed that no cracking of the oxide layer occurs ($\alpha \to \infty$).

PIM level vs. applied pressure

Fig. 3.2 shows the results of such a calculation (notice that for the $\sigma = 0.5 \mu m$ curve at $6 \cdot 10^4$ Pa the PIM level is indeed -100 dBm). As a general behaviour, the intermodulation level slowly decreases as the applied pressure is increased. This happens until a certain pressure, from which the intermodulation level decreases sharply. The explanation to this is that for low mechanical loads, the contact resistance is dominated by the non-contacting capacitance because the area of contact is very low. Therefore, the PIM level decreases slowly because it is directly related to the surface separation, which does not vary too much for different applied mechanical loads. As the pressure increases, the contact capacitance and the constriction resistances provide the electrical response of the junction and, therefore, the intermodulation level decreases much faster since these resistances depend linearly on the area of contact.

PIM level vs. roughness

As shown in Fig. 3.2, three different surface finishings have been chosen for investigating the effect of the roughness in the PIM level. In order to compare the three results properly, it has been assumed that the same contact resistance leads to the same intermodulation level. However, this is not necessarily true since the particular PIM mechanism can be dependent on the surface separation and, therefore, despite having the same voltage drop, the intermodulation level can be different. However, this is the only way to make reasonable comparisons, which are almost always applicable. Results show, as would be expected, that the larger the roughness, the larger the intermodulation. Nevertheless, this difference is only important if low loads are applied. The explanation to this can be found again in the fact that at low pressures the voltage drop is dominated by the non-contacting capacitance. Thus, if the roughness increases, the surfaces separation for the same applied pressure increases, which leads to an increase of the non-contact capacitor resistance. In spite of that, for high loads, the PIM level is not dependent on the roughness because the dominant resistances are the contact capacitance resistance

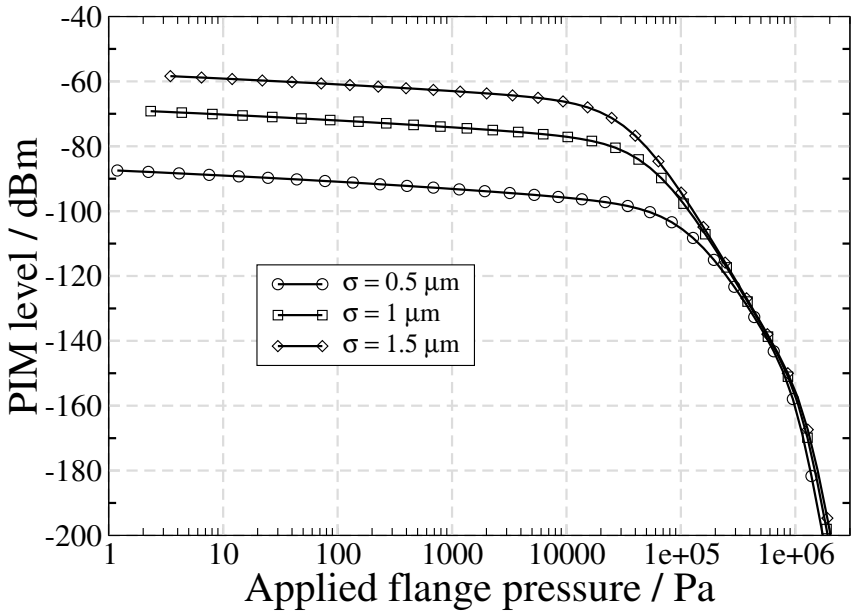

Figure 3.2: *PIM level for three different surface topographies.*

and the constriction resistance, which basically depend on the cleanliness of the surfaces. It has been experimentally observed by previous authors [9, 11] that, at low loads, the intermodulation level is rather unstable, probably due to oscillations in the contact resistance caused by the formation of a-spots of extremely small size, which response is hardly predictable. However, higher contact pressures are more relevant since are the employed in real applications.

The behaviour of the PIM level as a function of the surface roughness is, although, not yet completely described. The results of Fig. 3.2 are obtained assuming that no cracking of the oxide layer takes place. However, if cracking occurs, it is clear that a rough surface penetrates more easily than a smooth one into the oxide layer, breaking it and forming MM contacts. As mentioned, this leads to a decrease in the contact resistance which, in turn, diminishes the intermodulation level. Fig. 3.3 shows an example of such a situation. Again, for low applied mechanical loads, the rougher surface results in a higher intermodulation level. However, as the applied load is increased, the cracking of the oxide layer starts to diminish the contact resistance and, therefore, the PIM level.

This apparent contradiction in the dependence of the intermodulation level on the roughness has resulted in opposite statements from previous authors which experimental results [9,11] where somehow contradicting but, at the same time, completely compatible.

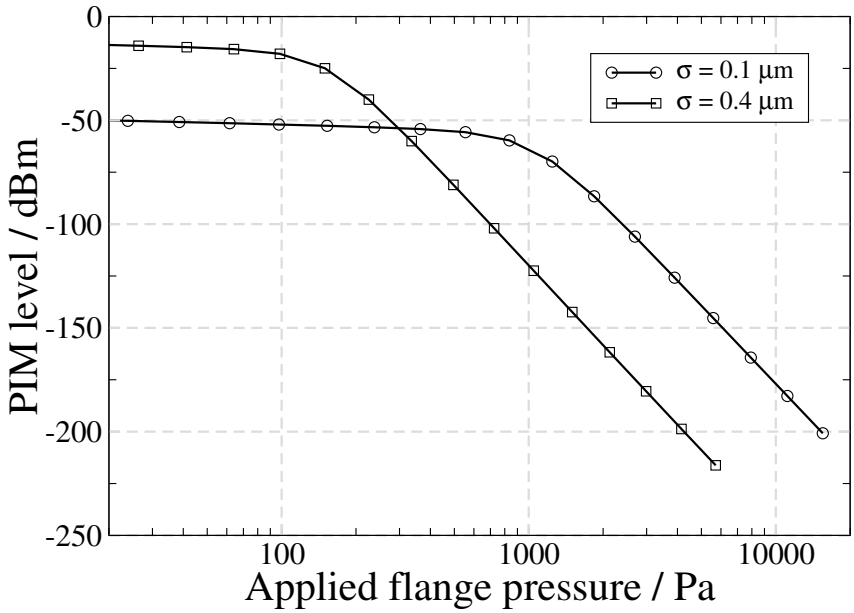

Figure 3.3: *Cases in which the PIM level decreases with the roughness of the surfaces. In this case* $\alpha = 2$ *and a softer material has been chosen:* $H = 50$ *MPa.*

PIM level vs. contaminant layer thickness

The influence of the covering layer thickness has been also investigated. Fig. 3.4 displays the PIM level for three different layer thicknesses. As expected, the thicker the layer, the higher the intermodulation level. In this case, the PIM level for low pressures is independent of the thickness, since the non-contact capacitance is basically independent of the layer thickness. However, for high applied mechanical loads, the contact capacitance, which is inversely proportional to the dielectric thickness, dominates. As a consequence, the voltage drop increases in this zone, resulting in a higher PIM level.

Since no physical source of the PIM excitation has been assumed, one has to be careful when analysing these results. It is true that, as it has been experimentally observed, the intermodulation levels are higher if the metals have suffered a higher degree of corrosion [78]. Nevertheless, if tunneling is the main PIM source, the thickness of the insulating layer also affects the intermodulation level beyond the voltage drop. As a matter of fact, tunneling falls exponentially with the thickness, whereas the voltage drop increase is only linear (and only if the MIM capacitor dominates the contact resistance). This will be seen in the next section for a particular example, in which the PIM level diminishes as the contaminant layer thickness increases.

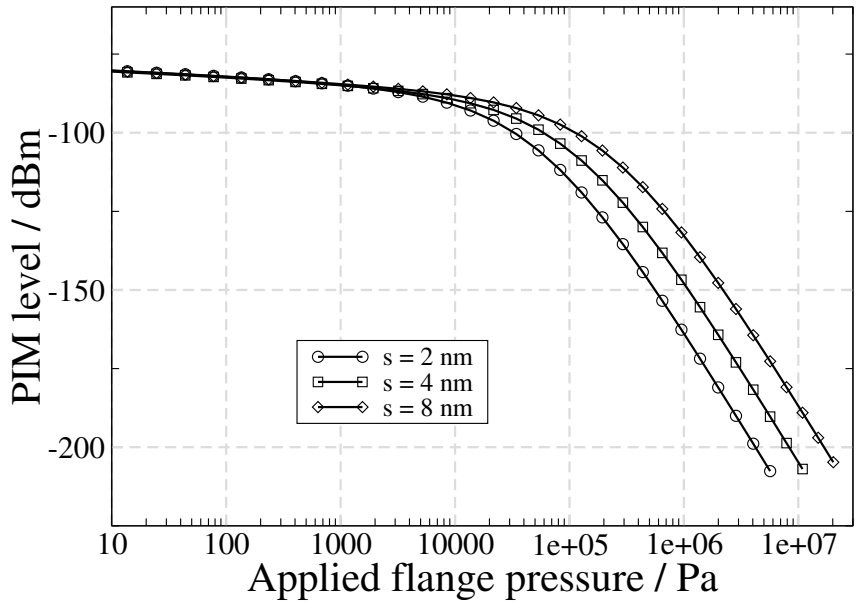

Figure 3.4: *PIM level as a function of the covering layer thickness.*

PIM level vs. cracking factor

Probably, the most important parameter to estimate the quality of a contacting material for electrical applications is the facility to break its oxide layer in order to form MM contacts. In this work, a cracking rate (α) has been defined in order to qualitatively describe such a phenomenon. The effect of this cracking rate is shown in Fig. 3.5, where four different values of α have been used. Again, it can be seen that, at low loads, no influence of the variable, in this case the cracking rate, is observed. The decrease of the cracking rate has, as a consequence, that the strong decrease of the intermodulation level starts at lower pressures because more a-spots are formed for the same applied mechanical load.

PIM level vs. mechanical properties

An important topic in the seek of PIM free flanges is the use of coatings. Normally, soft metals are employed since they provide a better contact and, therefore, a lower contact resistance. As an example of the extremely importance of this, Fig. 3.6 compares the intermodulation level of indium (very soft material) and aluminium. Neither the cracking parameter nor the oxide layer thickness have been modified though, it is clear that, in real life, their values are different for each material. Hence, the only difference between both cases comes from their mechanical properties. Additionally, it has been assumed that the surface aspect is not modified by the application of the coating (same roughness) and that the mechanical response is only due to the coating material (coating is thick enough). Indium has been chosen because it has been used as coating, showing very good

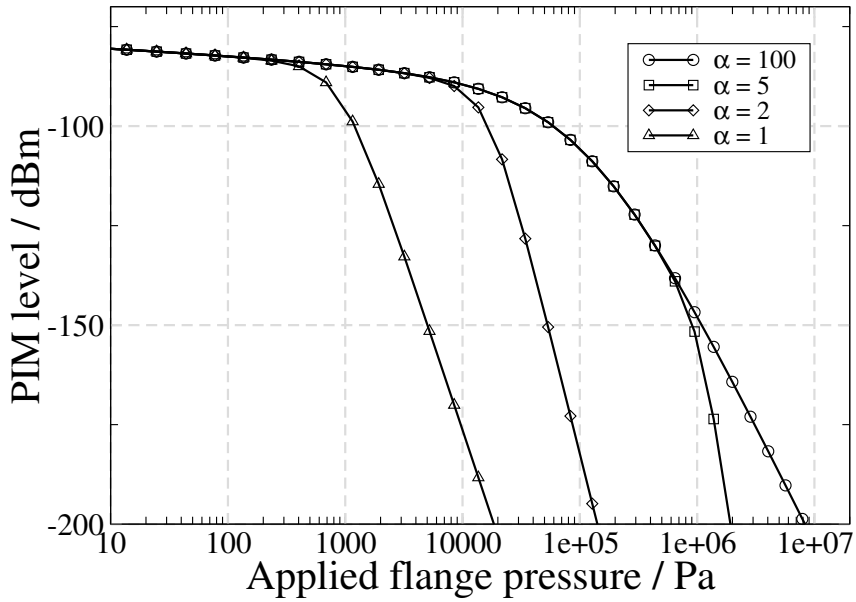

Figure 3.5: *PIM level for different cracking rates.*

PIM response at least the first time the flanges are tightened (see e.g. [100]).

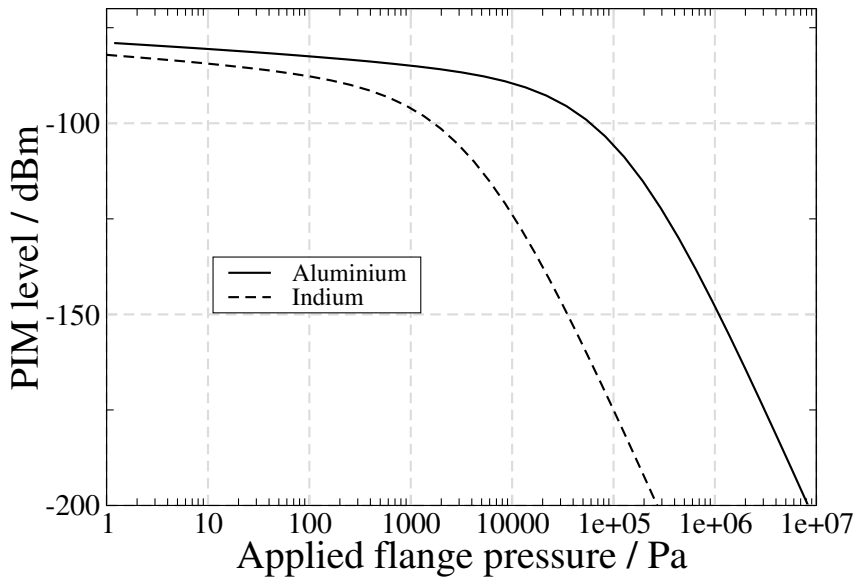

Figure 3.6: *PIM level for the case of a standard waveguide (aluminium) connection and in the case in which the flanges have been coated with indium keeping the topography of the surfaces.*

The graph shows that the PIM level is enormously reduced if the waveguide flanges are coated with Indium. The question arises immediately. Why not use soft materials like Indium in waveguide flanges? Their use is limited for two reasons: first, the high stresses that are generated due to the difference of the thermal expansion coefficient of the waveguide metals (aluminium) and that of the bolts (iron/steel) used to tightened them.

If the material were too soft, it would exist the possibility that, in one of the temperature extremes, it were plastically deformed and could not recover its original shape when the other temperature extreme were reached, leading to a decrease of the overall contact pressure between the flanges [94]. Second, and maybe more important, due to the extremely softness of the coating, it can be easily displaced from the high pressure zones after many mounting/unmounting cycles, which finally makes the whole coating disappearing of the region of interest.

Conclusions

Different calculations based on the model presented have been performed in order to characterise the system parameters influence. This has been done using a general non-linear PIM response based on the ability of splitting it in different orders which do not interact. In order to consider this interaction, and the possibility of determining different PIM signals amplitude once one intermodulation level is known, there are two possibilities: to use a mathematical non-linear function (see [101]) which allows for an arbitrarily long Taylor expansion series and has no physical meaning, or to employ a physical-based function which additionally provides information about the physical nature of the phenomenon. More attention has been paid to the second option since a physical interpretation of the PIM generation through (2.32) has been suggested by previous authors [102]. Besides, in section 3.3 a phenomenological expression based on an arctangential function is also presented since it has been used in the bibliography [101] for the assesment of the PIM response of RF systems.

3.2.2 Tunneling & Thermionic emission

In this section, the intermodulation level is computed assuming that the PIM physical sources are tunneling and thermionic emission in the Metal-Insulator-Metal regions. Therefore, (2.32) is used for the calculation of the non-linear current. The main advantages of this approach are three: knowledge is acquired about which physical parameters can affect the PIM level; once the power of a single intermodulation frequency is known, the rest can be extracted; and finally, higher order contributions to lower ones are automatically considered.

Apart from the voltage drop itself, the three main parameters that affect the non-linear strength of (2.32) are: the thickness of the insulating layer, its dielectric constant, and the barrier height. Given a PIM reference value and an applied load, these three pa-

rameters can be varied in order to obtain the same intermodulation level as the reference one. Since the insulating layer thickness and the dielectric constant also affect the voltage drop at the connection (see (3.17)), only the barrier height has been used, since it is the unique parameter exclusively affecting the tunneling and the thermionic currents, as the fitting variable in order to obtain the calibrated PIM level. As far as tunneling is concerned, one more remark has to be done. Due to the intrinsic inhomogeneity of the oxide layer, its real physical thickness does not correspond to the tunneling thickness in (2.32). This occurs because of the exponential nature dependence of the tunneling current on the insulator layer thickness. Therefore, an effective tunneling thickness can be defined, which can be again used in (2.32). This thickness results to be, approximately, one half of the real physical layer thickness[103,104], though this is qualitative and hardly predictable.

In this case, since the whole PIM spectrum is searched, a Fourier transform in time domain has to be performed to calculate the part of J(V) which corresponds to each PIM signal. Notice how the contributions of higher orders are taken into consideration automatically due to the general character of (2.37) and to the numerical calculation by means of the Fourier transform.

Fig. 3.7 shows the results of the Fourier transform after the calibration of the third order. It is seen how the third order intermodulation frequency in the upper part of the spectrum (10.25 GHz) coincides with the calibrated value (-100 dBm). To achieve this result the barrier height is 1.63 eV, a value which is close to the typical barrier heights (for instance, for alumina the barrier height is around 1.8 eV) [105]. The two large peaks correspond to the PIM signals which interfere with the input carriers; no significant interference occurs to the input carriers since they have a power of 50 dBm (100 dBm over the PIM signal) whereas the interference products are around -40 dBm.

As in the case of the Taylor approach, the intermodulation level as a function of the applied mechanical load can be also determined using the physical formulation. The calculation of the PIM level as a function of the applied pressure of Fig. 3.8 shows the general result of a non-linear component that only depends on the total resistance of the junction. In other words, the PIM level depends only on the voltage drop on the whole connection. However, if we only consider the MIM regions as possible PIM sources , the resulting dependence becomes different. As Fig. 3.8 shows, the case of considering only the MIM regions leads to the fact that, being in the low pressure range if the pressure increases, the intermodulation level also increases. This is due to the fact that the region of contact is very low and, consequently, low PIM is generated. As the pressure increases, more area is in contact and, hence, more MIM non-linearity is generated. At very high pressures, the area of contact is very high and therefore the current density in the MIM regions has decreased. It is thus clear that the peak appears due to this balance: total MIM area versus current density (voltage drop).

However, it is not realistic to assume that, at low applied mechanical loads, the PIM

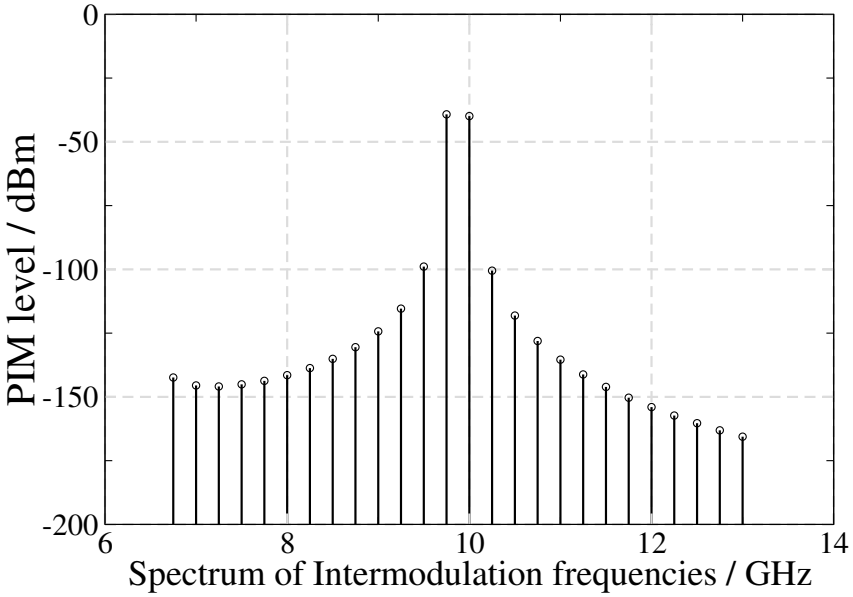

Figure 3.7: *Results for all the intermodulation frequencies falling inside the band of the fundamental mode using tunneling and thermionic emission in the MIM zones as source of intermodulation. The barrier height used is 1.63 eV.*

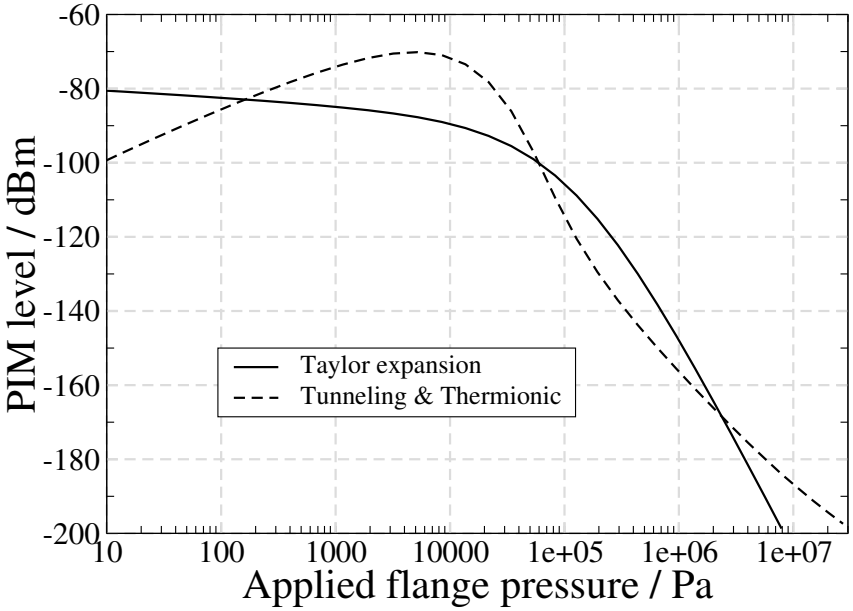

Figure 3.8: *PIM level as a function of the applied pressure in the case of a Taylor approach and in the case of considering a MIM structure only as the PIM source. No cracking is taken into consideration. The barrier height used is 1.63 eV*

source is located in the contact regions. It is likely that the PIM excitation is caused by some mechanism in the non-contacting regions, since the area of contact is extremely low.

Fig. 3.9 shows the fact that the increase of the oxide thickness leads to the decrease of the PIM level as opposite to the behaviour of Fig. 3.4. This happens because the main contribution is due to tunneling which decreases with the insulating thickness. It could be thought that a better PIM response would be obtained by oxidising the flanges on purpose. However, if the insulating thickness is larger, other non-linear processes can occur in insulators such as Poole-Frenkel [79].

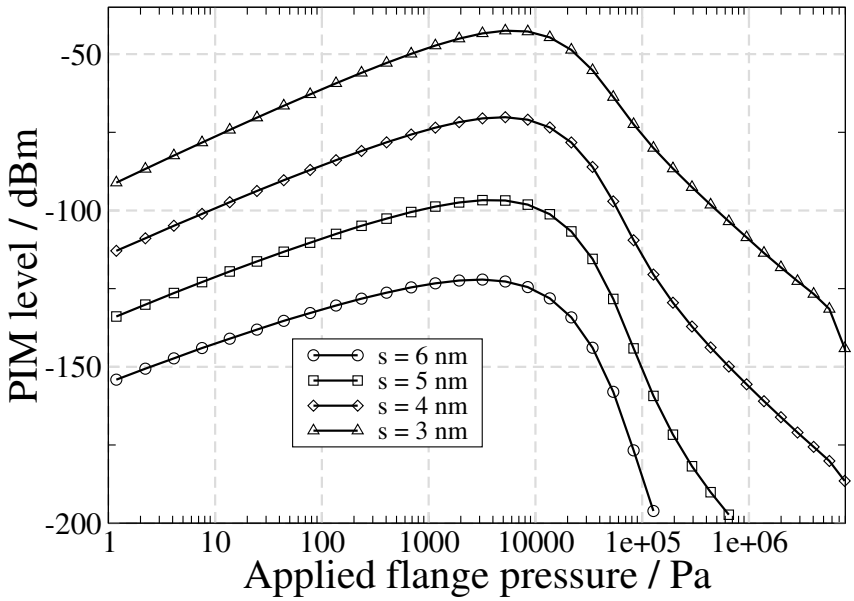

Figure 3.9: *PIM level decreases with the insulating layer thickness.*

3.3 Phenomenological PIM function

The PIM results presented in the previous section are based on a physical mechanism as the PIM generator. General non-physical functions exist in the literature which have been used in order to simulate the PIM response of a system. Among them, probably the most commonly used has been the arctangential function [101]. This function reads:

$$Y = A \cdot \tan^{-1}(X/B). \tag{3.25}$$

In our particular case, the meaning of Y and X is clear; they are the PIM signal surface current and the voltage drop at the junction respectively. Two constants (A and B) are used in order to fit this function to the particular PIM level.

The main advantage of this function is that one can apply it regardless of the particular PIM mechanism. It will be seen in the next chapter that this function is quite appropriate when attempting to predict the intermodulation level at high powers. In fact, this is probably the reason why it has been used as a PIM generator: it provides the PIM level dependence on the combined power. However, this fact does not mean that the arctangential function is the result of physical processes involving PIM.

3.4 PIM level vs. total power

The variation of the PIM level with the total combined power provides a large amount of understanding about the processes that cause the phenomenon. If only one order of intermodulation contributes to the intermodulation level of a particular frequency, a clear dependency exists between the PIM variation and the combined power (in dBm). The dependence can be easily derived. The amplitude of the PIM signal is proportional to the amplitude of each carrier. For an order $N = |m| + |n|$

$$A_{PIM} \sim A_1^n \cdot A_2^m.$$

On the other hand, $A \propto P^{1/2}$ and $PIM \propto \log[(A_1^n A_2^m)^2]$. Hence, $PIM \propto \log(P^{|m|+|n|}) = \log(P^N)$ and therefore, for order N, a N dB/dB dependence appears. However, experiments performed by previous authors (see e.g. [9]) have shown that this dependence can be quite different. In fact, normally a lower slope is observed which tends to saturation for very high input powers. Notice that such a behaviour must occur since, otherwise, the PIM level would monothically increase with the input carriers power. This would finally result in an unrealistic situation in which the PIM signal power would become larger than the signals power which have generate it. Deviations from the N dB/dB rule can occur mainly due to two facts:

1. Higher order contributions are not negligible.

2. Contact parameters are affected by the input power.

In case 1, it is clear that if higher order contributions are not negligible, the power dependence changes since the higher the order, the higher the dependence. However, it can not be stated which will be the direction of the change, if increasing to a greater slope or to a lower one. This basically depends on the sign of each derivative in the full Taylor expansion as well as on its strength. Fig. 3.10(a) shows the variation of the third-order PIM level as a function of the total combined power in the case in which no a-spots are formed at all. The straight line follows the N dB/dB rule, since it has been obtained following the mathematical approach for order three. For the physical approach, the calibration has resulted in a barrier height of 1.5 eV. It can be seen that the physical approach also follows the N dB/dB rule for low powers. However, as power increases, deviations can be observed due to a positive contribution of higher orders which lead to a stronger power dependence. The common point of both lines is the calibration point

(P= 200 W, PIM=-100 dBm).

If negative derivatives are present, a cancellation can occur among positive and negative contributions which results in a PIM valley for some particular system values. This has been identified in the literature as sweet spots [106] and has been used in active components in order to make them work under low intermodulation conditions. However, it is difficult to predict such a valley in the case of metallic junctions since many uncontrolled variables are present. An example of sweet spot appearance can be seen in Fig. 3.10(b). One of its characteristics is that the slope before and after the sweet spot is different.

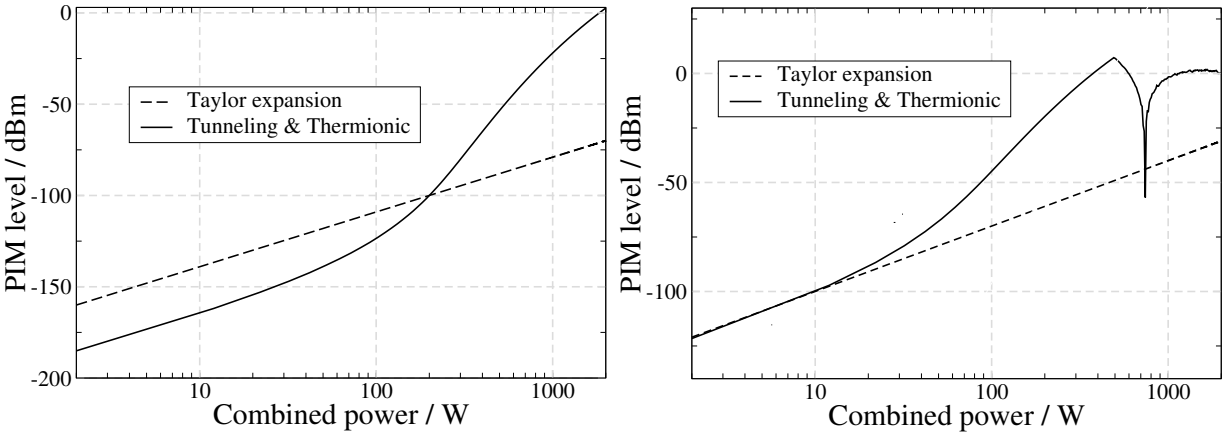

(a) *Calibration: 200 W, -100 dBm. The barrier height used is 1.5*

(b) *Calibration: 10 W, -100 dBm. The barrier height used is 0.86*

Figure 3.10: *PIM level as a function of the combined power.*

In the case that cracking occurs, the physical approach can also be followed. Fig. 3.11 shows the results obtained for two particular cases for which the cracking rate is different.

There is one way to clearly distinguish whether the deviation from the N dB/dB rule is due to higher order contributions or not. It consists in measuring the PIM level as a function of the power ratio. This provides an invaluable information about higher orders without measuring them. Next section fully develops this concept.

In case 2, deviations of the N dB/dB rule caused by some dependence of the contact mechanism on the total input power is the other possibility. The increase of the input power must improve the conductivity of the junction in order to explain why a lower slope is indeed experimentally observed (see next chapter). This is easily understandable if the local temperature heating of the a-spots is considered. Increasing the power, one increases the voltage drop and, therefore, the temperature. This heating softens the oxide layer and, as a consequence, more a-spots are formed or those already existing become

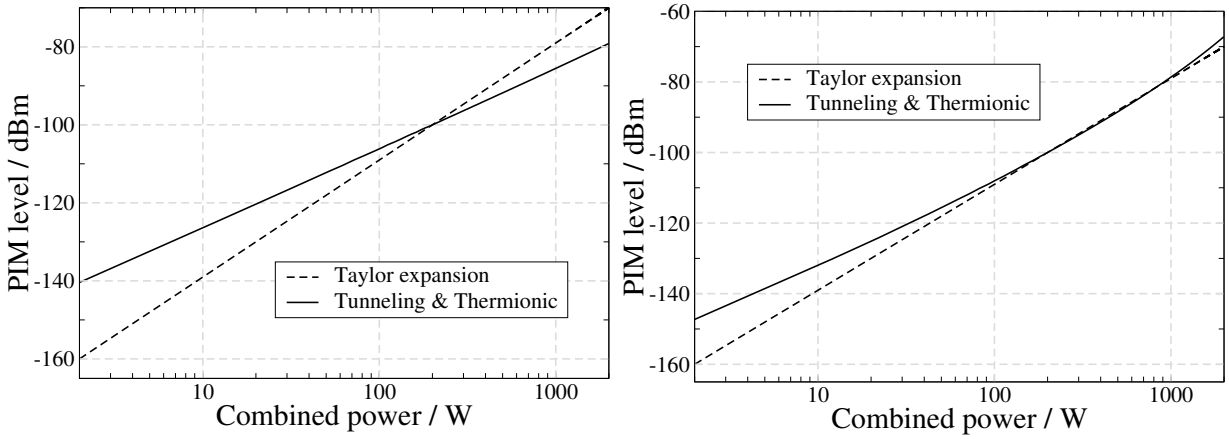

(a) *Cracking factor used is 1.0. The barrier height used is 0.307 eV*

(b) *Cracking factor used is 2.0. The barrier height used is 0.66 eV*

Figure 3.11: *PIM level as a function of the combined power. Calibration: 200 W, -100 dBm.*

larger.

3.5 PIM level vs. power ratio

In the last section, it has been seen that higher order contributions can affect the level of a particular PIM signal. However, this can not be known just by measuring the slope of the intermodulation level versus the total power, since increasing the input power the contact characteristics of the junction are changed (case 2). Nevertheless, a method exists that can be used to know the impact of the higher orders without modifying the total combined power. This method is as simple as measuring the PIM level as a function of the power ratio between the carriers.

The frequency of intermodulation $f_{int} = mf_2 - nf_1$ is considered in the following. The power ratio is defined as $\overline{R} = \frac{P_2}{P_1}$, where P_2 corresponds to the signal with frequency f_2 and P_1 to f_1. Additionally, the total power is kept constant, i.e., $P_1 + P_2 = P_T$. Thus, the powers can be written as a function of the desired variable only

$$P_1 = \frac{P_T}{1+\overline{R}} \qquad \text{and} \qquad P_2 = \frac{P_T \cdot \overline{R}}{1+\overline{R}}.$$

The amplitude of the PIM signal is proportional to the amplitude of each signal. For an order $N = |m| + |n|$:

$$A_{PIM} \sim A_1^n \cdot A_2^m.$$

On the other hand: $A \propto P^{1/2}$ and $PIM \propto \log[(A_1^n A_2^m)^2]$.

Therefore:

$$PIM \sim m\log(P_2) + n\log(P_1) = m\log\Big(\frac{P_T \cdot \overline{R}}{1+\overline{R}}\Big) + n\log\Big(\frac{P_T}{1+\overline{R}}\Big). \tag{3.26}$$

The derivative of this expression as a function of $\overline{R}$ provides the location of the maximum

$$\frac{d}{d\overline{R}}(PIM) = 0 = \frac{m}{\overline{R}} - \frac{m}{1+\overline{R}} - n\frac{1}{1+\overline{R}} \quad ,$$

or,

$$m(1+\overline{R}) - m\overline{R} - n\overline{R} = 0.$$

And then, the maximum occurs for:

$$\overline{R} = \frac{m}{n}. \tag{3.27}$$

Thus, for instance, for third order, $m = 2$ and $n = 1$, and therefore, the maximum must occur when the input power of the frequency with $m = 2$ is double than the other signal power. In this case, the input signal of 10 GHz should have the double of power than the signal of 9.75 GHz. This is shown in Fig. 3.12. Any deviation in the location of this maximum irremediably indicates that higher order contributions are of relevance. In fact, as seen in (3.27), the tendency at higher orders is the displacement of the maximum to 1; the higher the order, the closer the maximum to the unity.

Experimentally, the main difficulty is to detect accurately such a maximum since, as observed in Fig. 3.12(b), on the top of the curve a high sensitivity is required, which can not be always achieved.

This problem can be solved if, instead of considering the maximum itself, one considers the slope of the curve for very high and very low power ratios when the plot is logarithmic as in Fig. 3.12(a). From (3.26), the derivative respect to the logarithm of the power ratio can be performed:

$$\frac{d}{d(\log(\overline{R}))}(PIM) \equiv \overline{R} \cdot \frac{d}{d\overline{R}}(PIM) = \frac{m}{1+\overline{R}} - \frac{n}{\overline{R}(1+\overline{R})}.$$

Taking the limits for large and small power ratios:

$$if\ \overline{R} \uparrow\uparrow, \qquad \frac{d(PIM)}{d(\log(\overline{R}))} \to -n$$

$$if\ \overline{R} \downarrow\downarrow, \qquad \frac{d(PIM)}{d(\log(\overline{R}))} \to m$$

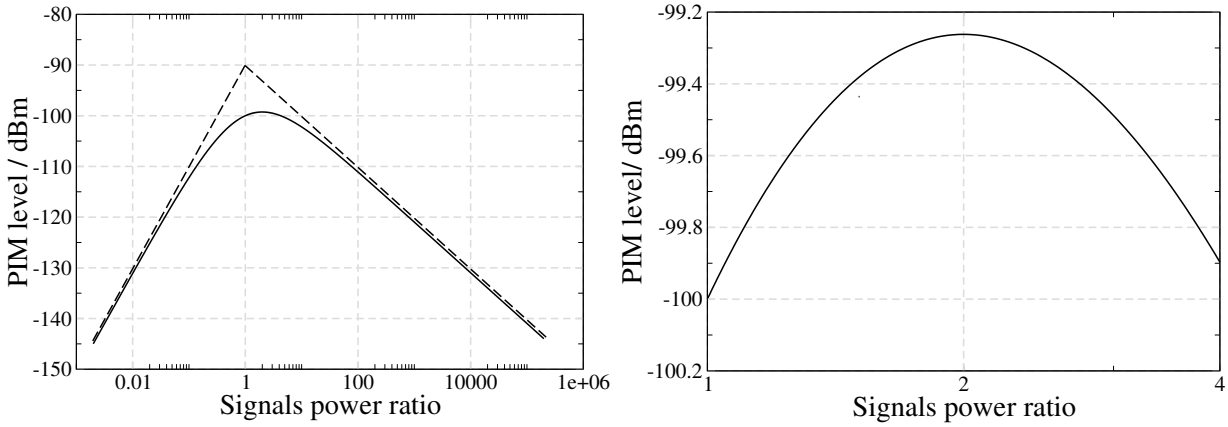

(a) *The two lines show the slopes of value 2 and -1.*

(b) *A zoom of the left figure where it can be seen that the maximum occurs at a power ratio equal to 2.*

Figure 3.12: *PIM level vs. power ratio for third order if no higher order contributions are relevant.*

This can also be seen in Fig. 3.12(a). The two straight lines represent the two slopes derived above. Deviations from this behaviour directly imply that higher order contributions are of relevance in the calculation of a particular PIM frequency. For such a case, the Taylor approach can not be used to simulate the system.

An example for the deviation of this behaviour is shown in Fig. 3.13, where the PIM level as a function of the power ratio has been plotted for different calibration points (same intermodulation level but different combined power). By increasing the total combined power, deviations from the single order contribution become more and more significant: maximum gets closer to the unity and the slopes also diverge from the predicted values.

From the practical point of view, the real application of this knowledge is related to simplify a complex PIM test set-up for measuring several PIM orders simultaneously and to reduce it to a two carrier test set-up.

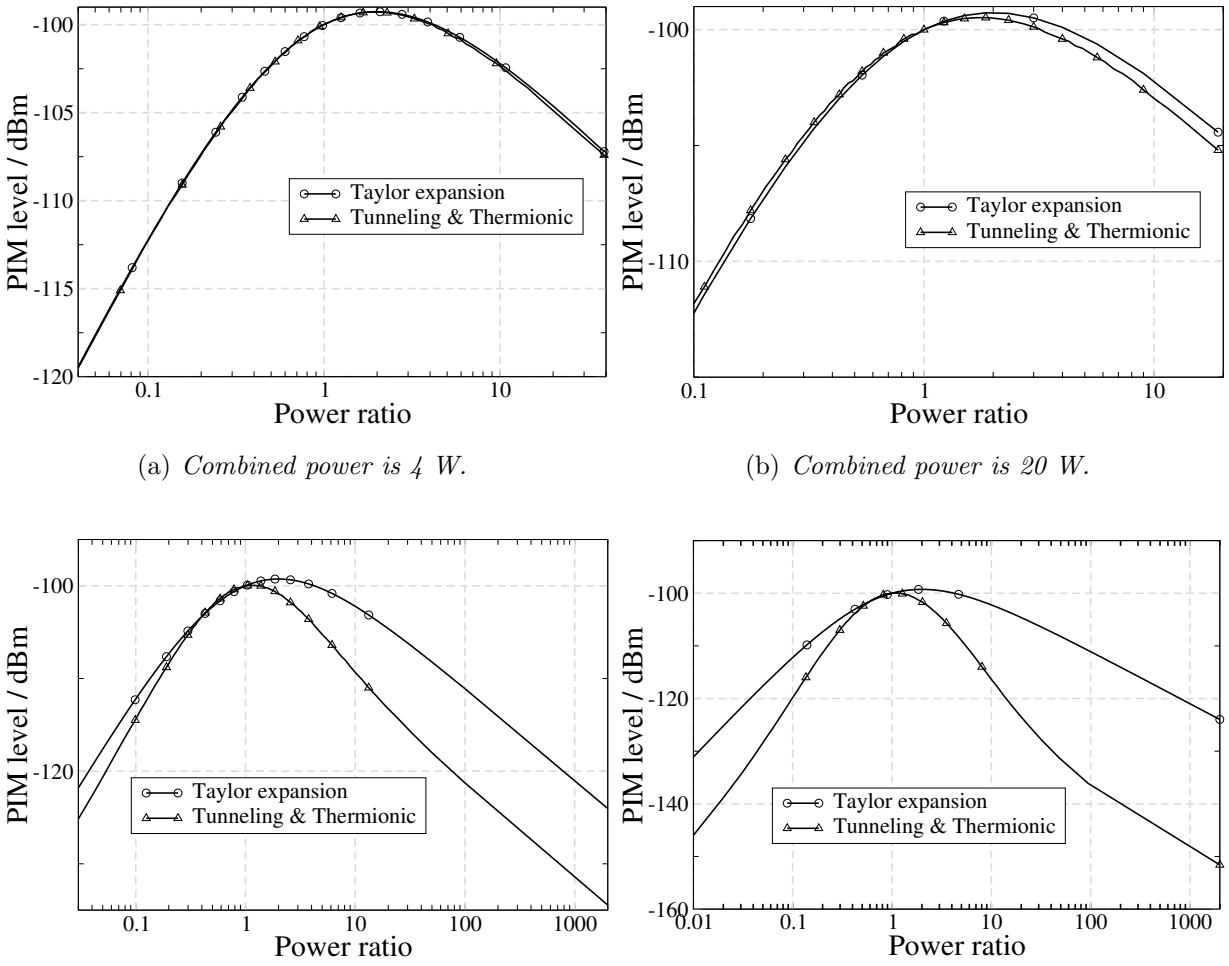

(a) *Combined power is 4 W.*

(b) *Combined power is 20 W.*

(c) *Combined power is 200 W.*

(d) *Combined power is 2000 W.*

Figure 3.13: *PIM level vs. power ratio for different calibration points.*

Chapter 4

PIM Measurements

Any satellite payload is formed by different passive (and active) components which have to be interconnected. Therefore, the design of the flange connections is extremely important in order to ensure low intermodulation levels. To assess such a quality, every component has to be tested. Thus, a test set-up, which is also formed by several interconnected devices, with an extremely low intermodulation interference is necessary. In this chapter, experimental data in waveguide flanges are presented which can be used as guidelines to reduce the residual intermodulation level of a particular PIM test set-up and to design PIM free flight models.

4.1 Samples

Different considerations have to be taken into account before testing. First of all, the type of waveguide flanges that are going to be utilised. This includes the size of the waveguides themselves (which obviously defines the frequency range to be employed), the position, size and number of screw holes, the waveguide material, and the possible coatings that are deposited on it.

The waveguides used to perform the tests were standard WR-90 waveguides (22.86 x 10.16 mm) operating in X-Band (8-13 GHz). They were manufactured using pure aluminium ($>$ 99.9% purity) which is the standard material in Sat-Com applications due to its low weight. Nevertheless, aluminium waveguides are commonly coated with silver using a DC electroplating process (a silver thickness layer of around $10\ \mu m$ is deposited) in order to improve both the electrical and the thermal conductivities. Moreover, aluminium junctions generally show a high PIM level [11], whereas silver-plated aluminium connections present much lower intermodulation levels [8, 11]. Thus, silver-plated aluminium waveguides were also tested since they are, in fact, the standard waveguides used by the satellite industry.

As seen in photograph B.1, the waveguides had two different flanges. One of them

was the flange under test (six screw holes) whereas the other one (eight screw holes) was the interface with the test set-up (photographs C.1, C.2 and C.3). The latter should not add more intermodulation level to the noise floor and, therefore, a care design had to be chosen. This is the reason why an eight hole flange configuration was employed and the waveguides were joined to the test set-up interface flanges with the maximum possible torque. Moreover, the two interface flanges of the test set-up had a special design. In addition to the eight hole configuration, they also presented a "bridge" of 1 mm width and 1 mm height around the waveguide cavity and another bridge of the same dimensions in the outer side of the flange. This allowed for higher pressures in the RF path region since less area had to be brought into contact. On the other hand, the flange under test was a six hole flange. Such a configuration was chosen instead of the standard one of four holes in order to minimise possible mechanical instabilities.

Apart from full-length waveguides, short (3 mm long) gaskets as the ones shown in photograph B.2 were manufactured. They were also made using pure aluminium. These gaskets were coated with different materials and inserted between the waveguides providing, this way, information about the PIM response of the deposited metal. As shown in photograph B.2, two kind of gaskets were used: complete flat gaskets and high-pressure gaskets which presented a bridged configuration similar to the test set-up interface flanges described above. In order to have statistics, three flat gaskets and three bridged gaskets were coated per each material.

The materials deposited were:

- *Silver*, as mentioned above, is used as the standard coating in Sat-Com applications. Therefore, silver coated gaskets can be used as reference as well. Indeed, the quality of a specific material, in terms of its PIM response, must be evaluated by comparing it to the PIM behaviour of silver.

- *Hard Gold* (gold in general) is a very particular metal due to the fact that it does not oxidise. An oxygen layer (monoatomic) is formed on the surface, which does not grow beyond. Therefore, gold contacts always present a very low contact resistance since the covering layer is easily ruptured. One of the risks of gold is related to its softness. Electroplated pure gold is quite soft, what makes gold "disappear" from the contacting regions after some assembly/disassembly cycles. Thus, instead of pure gold, hard gold was employed. Hard gold is basically gold ($> 99\%$) alloyed with nickel or cobalt. Such an alloy increases the hardness ($H > 150$ MPa) of the metal, keeping unaltered its fundamental properties (no oxidation, high conductivity...).

- *Indium* is an extremely soft metal ($H \approx 8$ MPa). Therefore, it normally presents a very low PIM level [100] since the contaminant layer is displaced very easily. However, in our particular application, indium is normally not used for the same reason as pure electroplated gold: after some assembly/disassembly cycles, the indium layer

is completely displaced. This finally results in a metallic contact between the base metals. Nevertheless, indium was chosen for two reasons: it would probably provide the best PIM response for the first assembly cycle and, therefore, it could be used as reference. Also, the intermodulation response could be quantitatively investigated as a function of the number of assembly/disassembly cycles.

Some bare aluminium gaskets were left uncoated in order to use them as reference. Additionally, three flat and three bridged gaskets completely made of *beryllium-copper* were also tested.

- *Beryllium-Copper* (BeCu) is used in electrical contacts due to its low contact resistance [107]. Hence, it was also tested since previous researchers had reported that BeCu contacts result in low intermodulation levels [10, 11]. BeCu basically consists of copper with a beryllium content always lower than 2%.

The coatings of silver, hard gold and indium were performed by Tesat-Spacecom GmbH & Co. KG. The BeCu material was obtained from Brush Wellman GmbH and milled by Tesat-Spacecom GmbH & Co. KG.

4.2 Measurements

The intermodulation level between full length waveguides was measured. Three different dependencies, if possible, were checked: PIM level as a function of the applied torque, as a function of the combined power of the carriers, and as a function of the power ratio between the signals. The effect of the insertion of the different gaskets between the waveguides was investigated as well.

The minimum possible torque that could be applied to the screws was 4 Ncm, and the maximum 80 Ncm (nominal torque for M3 (3 mm diameter) screws).

The two input frequencies used during the test campaign were

$$f_1 = 11.21\ GHz, \qquad f_2 = 11.895\ GHz,$$

and the intermodulation frequency investigated was the third order intermodulation product falling in the upper side of the spectrum, i.e.,

$$f_{int} = 2 \cdot f_2 - f_1 = 12.584\ GHz.$$

The measurements were performed at Tesat-Spacecom GmbH & Co. KG facilities. The importance of an excellent test set-up in PIM measurements is critical due to the high sensitivity that must be reached. In this case, for the maximum available power (170 W per carrier), the noise floor, which defines the minimum intermodulation level that can be measured, was below -145 dBm.

4.2.1 Aluminium waveguide connections

The PIM response of several aluminium waveguides was investigated. Fig. 4.1 shows the intermodulation level as a function of the applied torque for a particular waveguide connection at a combined power of 60 W. The measurements were carried out several times (assembly/disassembly cycles) in order to look for reproducibility. This was done to check if stable results could be obtained and if the waveguide surface topography was modified due to the test campaign.

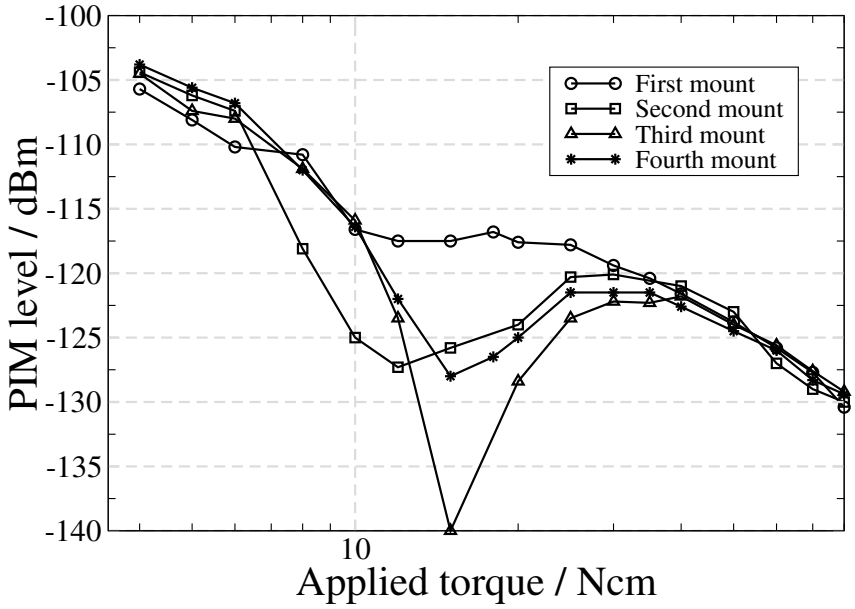

Figure 4.1: *PIM level versus applied torque to the screws for a combination of two aluminium waveguides. The process was repeated several times. P = 60 W.*

By inspection of Fig. 4.1, some repeatable facts do emerge:

1. At very low torques, the PIM level is more or less reproducible.

2. At high torques, the intermodulation level is quite repeatable as well.

3. At intermediate torques (between 10 and 20 Ncm) a PIM valley appears.

Due to the erratic character of PIM in metallic connections, it could be argued that this behaviour is not reproducible from one aluminium waveguide junction to another. Thus, a connection formed by two different aluminium waveguides was also tested (see Fig. 4.2). The same dependency was found, suggesting that it is, indeed, a general PIM behaviour for this kind of waveguide flange configuration.

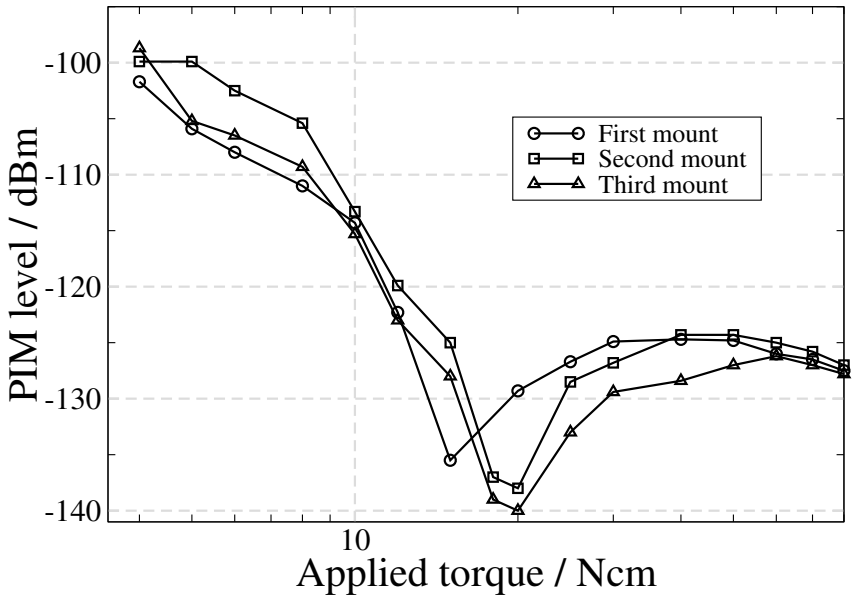

Figure 4.2: *PIM level versus the applied torque to the screws for a combination of two different (with respect to Fig. 4.1) aluminium waveguides. The process was repeated several times. P = 60 W.*

The repeatability of the intermodulation level is in disagreement with the statements of previous authors (see e.g. [9–11]), who have claimed that the PIM response at aluminium connections is unstable and unpredictable. This discrepancy is explained by two facts:

- Previous authors have not considered real waveguide connections but metallic contacts (normally rather small in terms of area of contact) submitted to a definite applied force.

- The pressure between the flanges is rather low and, therefore, surfaces are not critically deformed (do not reach the full plastic regime), and the oxide layer is not cracked either. Thus, no -or very few- a-spots are formed and the surfaces do not experience irreversible topographical deformation. This results in the repeatability of the system regarding its PIM response.

This is an extremely important result since it clearly manifests that aluminium connections with this particular waveguide flange configuration do present a repeatable PIM response. Moreover, standard waveguide flanges consist of 4 bolts and, hence, the overall pressure achieved is even lower. Thus, it is expected that standard waveguide flanges will also present repeatable PIM levels since the surfaces are not irretrievable damaged.

The existence of a minimum (or at least of a plateau) in the PIM response is also a noteworthy fact. Chiefly, two causes can explain this behaviour:

- A pure mechanical effect.
- An intrinsic effect to PIM mechanisms.

The mechanical effect is associated to the fact that the torque applied to the screws can lead to the deformation of the flanges: they do not support the applied torque and deform, reducing the pressure at the RF path zone. This can even result in the formation of an air gap in that region (a membrane effect). Hence, an increase of the PIM level with the applied torque for a particular torque range is expected. However, with the flange configuration used, it seems difficult that this phenomenon will occur since it has more impact when the screws are located far from the waveguide cavity and/or few screws are employed. Furthermore, this situation is also more prone to occur if thin flanges are used [108]. In our case, thick flanges (5 mm) are utilised which ensure a high mechanical stability. Thus, it is unlikely that the torque applied will cause a reduction of the pressure in the RF zone for a particular range. Moreover, it is also doubtful that this problem will be solved by applying higher torques to the bolts, as would be suggested by the decrease of the PIM level at that torque range.

The second possible reason for a minimum in the PIM valley is related to the possibility that different physical mechanisms are playing a role in the PIM generation. As stated in chapter 2, the conduction at very low contact pressures is dominated by the void regions since the area of contact is very low. Thus, it is expected that the physical PIM mechanism or mechanisms are located in these non-contacting zones. At higher contact pressures, however, the intermodulation level is generated at the contacting regions. This leads to the existence of two regions which transition, in terms of intermodulation level vs. contact pressure, is not smooth. This occurs because the PIM mechanisms in both zones are completely different in nature and, therefore, the intermodulation level from one pressure range is not related to the intermodulation level in the other one. If this is the case, there are two relevant features to consider:

- The PIM response at low torques is extremely pressure dependent (steep slope).
- The PIM mechanism/s at intermediate or high torques leads to an initial increase of the intermodulation level followed by a decrease at higher torques (see Fig. 4.2 for torques higher than 20 Ncm).

The first behaviour is related to the fact that, at low torques, the large irregularities (mainly waviness) of the surfaces are playing a leading role in the PIM response. A small torque change has a great impact on the mean surface separation and, thus, the intermodulation level varies accordingly. Moreover, the PIM mechanism itself can be dependent on the surface separation as it is, for instance, the corona effect (considered in the next chapters).

The second feature is in agreement with the shape of the curve in Fig. 3.8 shown in the previous chapter for the case in which tunnelling and thermionic emission are the

PIM sources. As already explained, the shape of the curve is not related to the particular mechanism/s but to the fact that PIM is essentially generated at the contacting regions separated by a contaminant layer, and not at the void zones.

Apart from the PIM level dependency with the applied torque, its variation with the combined power was also investigated. Fig. 4.3 shows such results for the connection in Fig. 4.2 at different applied torques. Comparison is done to the ideal case (3 dB/dB rule) and to the case in which the arctangential function is calibrated.

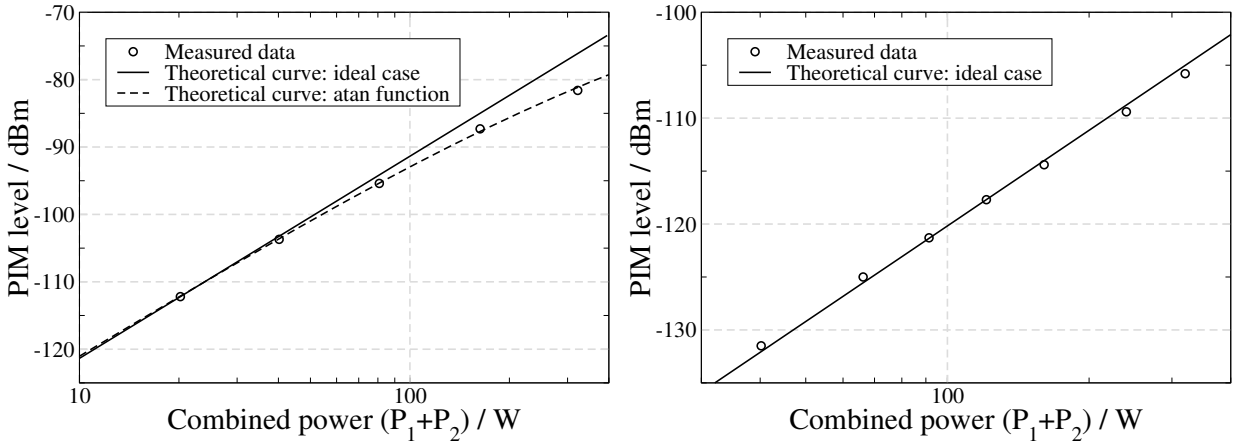

(a) *Applied torque equal to 4 Ncm. Calibration point: P = 20.2 W, PIM = -112.2 dBm.*

(b) *Applied torque equal to 80 Ncm. Calibration point: P = 121 W, PIM = -117.7 dBm.*

Figure 4.3: *PIM level as a function of the combined power for different applied torques.*

Deviations from the 3 dB/dB rule are only observed for the low torque case. In order to understand the cause of this behaviour, the PIM level has been also investigated as a function of the power ratio between the carriers. Fig. 4.4 displays the experimental results obtained together with the ideal case in which no higher order contributions are considered. It is seen that, for the input power used, a perfect agreement is achieved, indicating that orders higher than three are not contributing to the measured intermodulation level.

Therefore, a thermal effect due to the increase of the input power of the carriers is probably playing a fundamental role. As remarked in section 2.4, the most simple explanation is related to the difference between the thermal expansion coefficients (α) of the waveguide material (aluminium, $\alpha = 23.8 \cdot 10^{-6}$) and the screws (stainless steel V2A, $\alpha = 16 \cdot 10^{-6}$). At high power levels, the temperature of the system increases (in this case, the thermopars located close to the connection indicated that, for the highest input power of 340 W, a temperature around 39 ℃ was reached) what leads to different elongations of the screws and the waveguide flanges. Since aluminium dilates easier than steel, the effective pressure at the contact increases and, thus, the intermodulation level decreases.

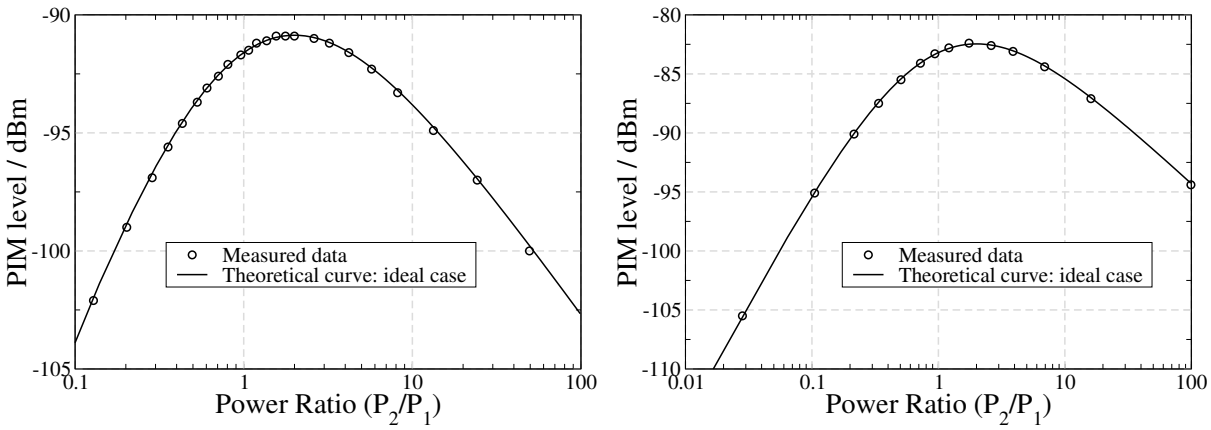

(a) *Combined power 100 W.* (b) *Combined power 170 W.*

Figure 4.4: *PIM level as a function of the power ratio for two aluminium waveguides connection using a torque of 4 Ncm.*

This effect has more impact with low torques since the surfaces have a greater range of deformation. The other possibility is that the local heat at the contact asperities (as shown by eq. 2.38) softens the oxide layer, allowing for a better contact, and reducing, this way, the PIM level. However, this effect seems to be secondary in aluminium connections up to the input power levels available. Otherwise, deviations should also occur when high torques are applied, which is not the case (see Fig. 4.3(b)).

Aluminium gaskets

Aluminium gaskets were inserted between the aluminium waveguides (the waveguides for which the PIM response is presented in Fig. 4.2) in order to measure their impact in the intermodulation level of the system. The results are shown in Fig. 4.5. Four type of measurements were performed: inserting one flat gasket (Fig. 4.5(a)), using one bridged gasket (Fig. 4.5(b)), employing two flat gaskets together (Fig. 4.5(c)), and without any gasket at all (Fig. 4.5(d)). This last set of measurements was done before, during and after the gaskets insertion in order to check if the test campaign modified the connection PIM response.

It is observed that the employment of gaskets led to an overall increase of the intermodulation level at low torques. In fact, at this torque range, the PIM response was quite unstable because two junctions (three in the case of two gaskets) were present and, thus, the surfaces barely deformed. However, at high torques, the PIM level was lower when using flat gaskets (one or two). In principle, this behaviour is not expected since each additional metallic junction contributes to the intermodulation level (an increase of 3 dB per extra connection should be observed assuming that each connection has the same

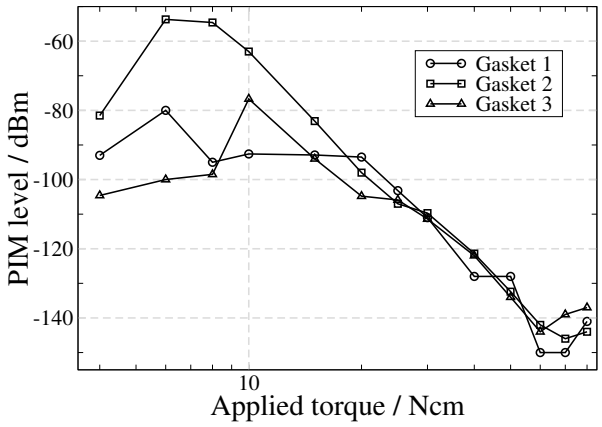

(a) *PIM level versus applied torque when one flat gasket is inserted.*

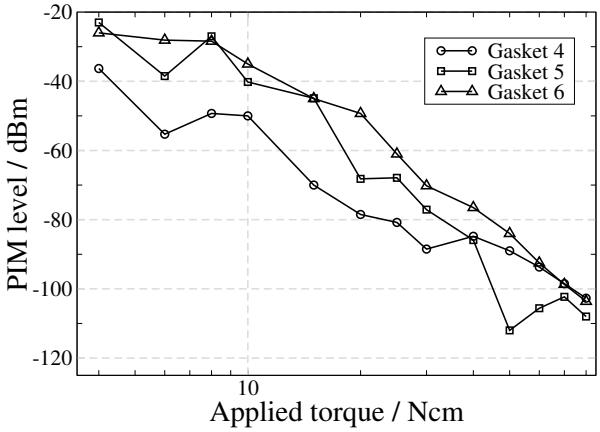

(b) *PIM level versus applied torque when one bridged gasket is inserted.*

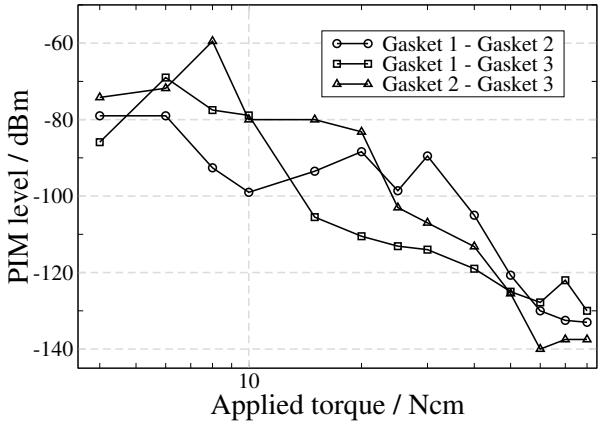

(c) *PIM level versus applied torque when two flat gaskets are inserted.*

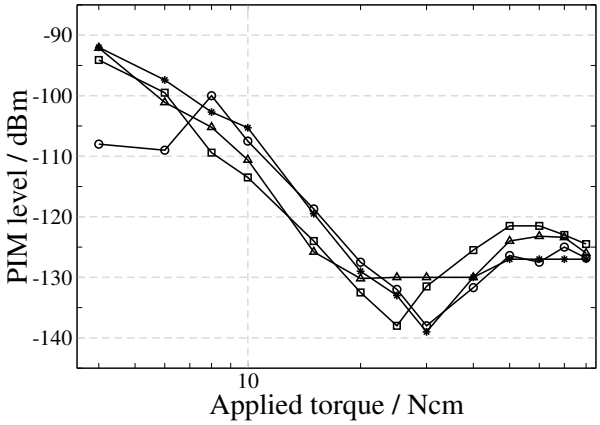

(d) *PIM level versus applied torque without gaskets.*

Figure 4.5: *Effect of inserting aluminium gaskets on the junction, P = 60 W.*

contribution). However, the insertion of gaskets leads to an increase of the thickness of the region between the screw head and the nut. In other words, an increase of the total flange effective thickness occurs. Such an increase results in a better distribution of the pressure caused by the application of the torque to the screws [108]. Indeed, in bolted junctions, it has been demonstrated that the area of contact increases if the thickness of the plates joined increases. Song et al. [109] have derived a formula based on Finite Elements which relate the radius of the nominal area of contact (r_c) to the thickness of the connecting plates (L_P) and the radius of the bolt head or washer (B_T) when one single bolt is used:

$$r_c = B_T + L_P/2. \tag{4.1}$$

With such a result, it can be seen that, in order to have a good contact, the distance between screws should be less than $2 \cdot r_c$. For the flanges employed (5 mm thick) and the washers used (2.85 mm radius), the distance $2 \cdot r_c$ is equal to 10.7 mm. In Fig. B.3, it is seen that the distance between screws in the broad wall is 13 mm and the distance in the narrow wall is 20 mm. Thus, the flange design is not optimised to have a good contact on the whole surface. This is more critical in the narrow wall although it is expected to generate a lower intermodulation level in that zone. By adding two gaskets of 3 mm, the contact in the broad wall is improved since $2 \cdot r_c$ is larger than 13 mm. The increase of overall contact can be seen in Fig. D.4. Sheets were inserted between the flanges to check the contact of the connection. The darker - more red - the sheet becomes, the better the contact. It is seen that in the pure waveguide connection (Fig. D.4(a)), a very good contact is achieved around the bolts. However, when a flat gasket is inserted (Fig. D.4(b)), the contact is more spread on the surface. Moreover, the contact at the narrow walls is clearly improved.

To sum up, the fact of adding gaskets has a double impact on the PIM response of the connection:

- An increase of the intermodulation level due to the increment of the number of metallic connections.
- A decrease of the PIM level caused by the increase of the effective area of contact.

Therefore, depending on each particular situation, the insertion of gaskets can improve or not the PIM response of the system. In any case, this discussion is true provided enough torque is applied. At low torques, the insertion of gaskets always leads to an increase of PIM caused by the lack of deformation of the metallic surfaces in contact.

The PIM response when bridged gaskets were inserted was rather surprising as well. This combination presented the worst results (PIM level higher than -110 dBm at the highest torque). However, the bridged gaskets configuration results in an increase of the pressure in the RF path zone and, therefore, a much better intermodulation level would be expected, at least, at high torques. At low torques, the extremely high PIM level (around -30 dBm) is explained by the fact that electromagnetic radiation was detected flowing out of the flange. Due to this, it is expected to have high and unstable intermodulation levels. Indeed, this was the case. Radiation was detected up to 15 Ncm. Nevertheless, it is likely that, at higher torques, there was still a considerable amount of electromagnetic field "confined" between the inner and the outer bridges and, probably, the screws were an additional PIM source. However, probably the main reason why they presented such a large intermodulation level was that it was checked (by simple visual inspection) that the surface of these gaskets was quite irregular presenting many flaws.

Finally, there was a displacement of the location of the PIM valley after the use of the gaskets (see Fig. 4.5(d)). This is another fact in favour of the second of the options to explain its existence. The use of the bridged gaskets affected the surface close to the RF

path zone by flatting it. As a consequence, the force necessary to put again into contact such regions increased because they had been deformed plastically.

Silver-plated gaskets

Silver-plated aluminium gaskets were also inserted between the aluminium waveguides (results in Fig. 4.6). It can be noticed that the insertion of such gaskets improved the PIM level at high torques. Thus, it is confirmed again that the increase of the effective flange thickness results in a better mechanical contact. However, no substantial improvement is observed with respect to the case of aluminium gaskets except for the case of silver-plated bridged gaskets. In that case, the intermodulation level was driven around -145 dBm at the highest torque. This improvement is caused by the increase of contact around the waveguide cavity (RF current path zone). After the insertion of the silver gaskets, the valley still appeared but it was even more displaced to higher torques, providing another evidence that the PIM valley is caused by a balance between PIM mechanisms.

Additional measurements

Hard Gold gaskets presented a behaviour similar to silver-plated ones (see Fig. D.1). The insertion of gaskets lead to a better PIM response at high torques than the pure waveguide connection. However, by inspection of Fig D.1(d), it can be observed that the intermodulation level for the aluminium connection without gaskets was also quite low at this level. After this set of measurements, the intermodulation valley has almost vanished.

Beryllium-Copper gaskets had the same impact as the previous cases (see Fig. D.2). At low torques high PIM levels were measured whereas at high torques, levels close to the pure connection were found. In fact, it is seen that the insertion of bridged BeCu gaskets drove the intermodulation level under -140 dBm for the three gaskets. After this set of measurements, it is observed that the PIM valley did not occur anymore but just a plateau indicating that the surface has been seriously flattened at the RF zone due to the application of the bridged gaskets.

Indium gaskets insertion resulted in the lowest PIM level of all the gaskets employed (as Fig. D.3(a) shows). The use of these gaskets drove the intermodulation level under the noise level regardless of the geometry of the gasket (flat or bridged). In this case, not all the gaskets were used because it was observed that, after the first assembly, the indium layer had been seriously damaged. Therefore, an indium flat gasket was assembled and disassembled several times in order to see the evolution of the PIM level. This is shown in Fig. D.3(b). It can be seen that, just after four assemblies, the intermodulation level saturates at a high and stable value. This saturation level is not better than the intermodulation level obtained when using silver or hard gold plated gaskets.

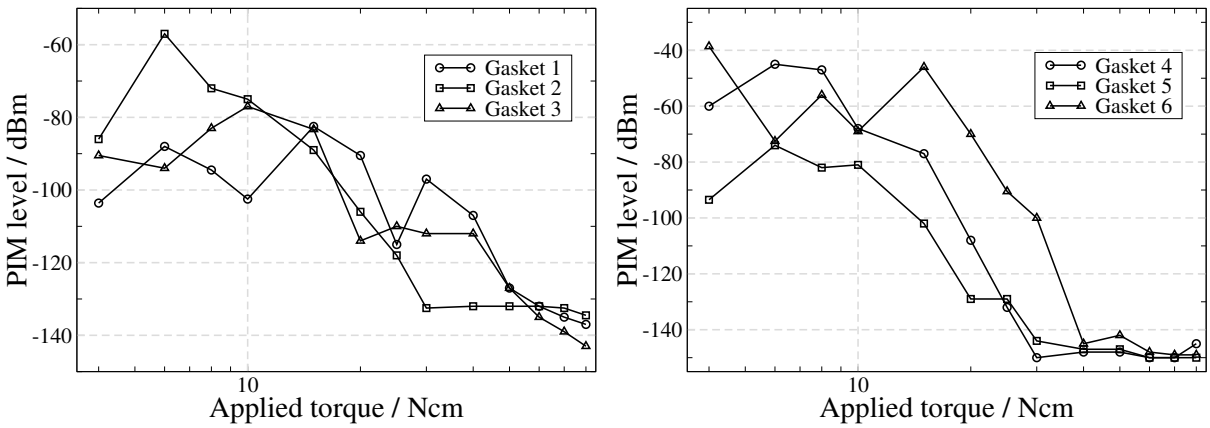

(a) *PIM level versus applied torque when one flat gasket is inserted.*

(b) *PIM level versus applied torque when one bridged gasket is inserted.*

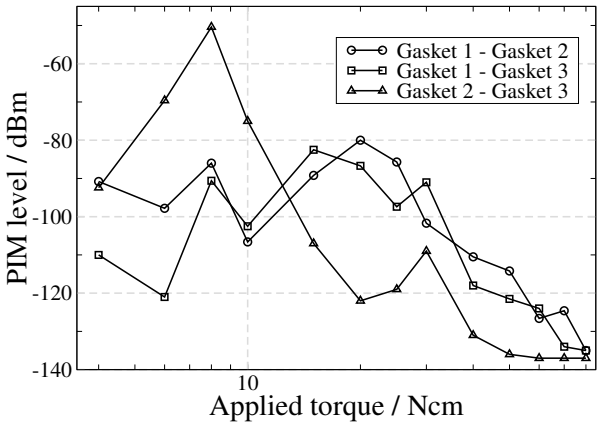

(c) *PIM level versus applied torque when two flat gaskets are inserted.*

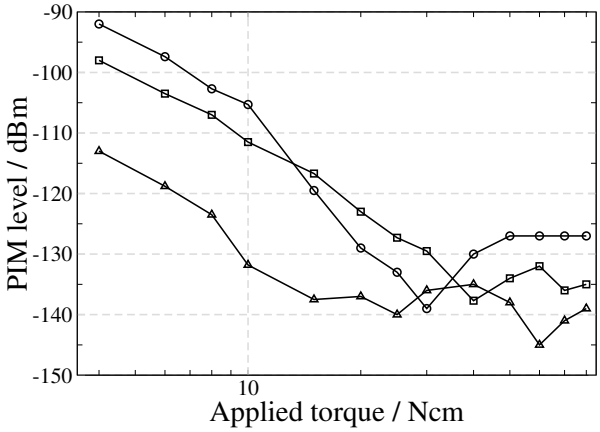

(d) *PIM level versus applied torque without gaskets.*

Figure 4.6: *Effect of inserting silver-plated aluminium gaskets on the junction, P = 60 W.*

Summary of aluminium waveguide connections

From the experimental results and analysis presented above, several conclusions can be extracted:

1. The intermodulation level decreases very steeply in the low torque range due to large irregularities of the surfaces.

2. The existence of an intermodulation valley, observed for different samples, indicates a change of the physical sources responsible for PIM generation.

3. At low loads, the use of gaskets results in rather high and unstable PIM levels. In fact, in many occasions, electromagnetic radiation flows out of the flange. At

this point, it is likely that the screws themselves are notably contributing to the measured intermodulation level.

4. The use of high pressure gaskets changes the surface profile of the waveguide flanges close to the RF path zone, as observed by the change in the PIM response throughout the test campaign.

5. The use of more than one gasket does not generally result in a worse PIM response at high torque values. The increase in the ability of the screws to transmit the applied torque, compensates the decrease of the surfaces deformation and the PIM generation caused by the increase in the number of metallic connections.

6. As a guideline, the flanges should be always designed in such a way that the distance between screws is never larger than $2 \cdot r_c$, as defined in (4.1).

7. At low loads, deviations from the theoretical predicted 3 dB/dB PIM variation as a function of the input power level are observed. Such deviations are not originated by the contribution of higher orders but to the mechanical stress caused by the thermal expansion coefficient difference between the screws and the waveguide metals.

8. However, at high torques, the predicted curve is followed. Of course, this is due to the limited input power available. At higher power levels, a behaviour similar to the case of low torques should appear since, otherwise, the PIM level would monotonously grow until reaching a level of the order of the input signals, which is physically impossible.

9. The indium case provides the best response though its use is limited in terms of the number of times that it can be employed.

4.2.2 Silver-plated aluminium waveguide connections

As mentioned previously, in standard applications the most common used waveguide configuration is an aluminium waveguide (due to its low density) coated with silver (in order to improve the electrical conductivity). Moreover, silver also presents a low intermodulation level at metallic connections, as shown by previous researchers [8, 9], because its contaminant layer is broken at low contact pressures.

The first important fact that appeared when the waveguides were joined was that the full available input power was necessary in order to have a reasonable high PIM level even for the lowest torque. In other words, whereas a combined power of 60 W was enough in the case of aluminium in order to measure a significant intermodulation level even at high torques, this did not happen for silver-plated waveguides. In fact, for an input combined power of 60 W and the minimum applied torque, the PIM level was very close to the noise floor. Therefore the full available input power (170 W per carrier) was employed in this situation. Unfortunately, this means that it was not possible to investigate the

intermodulation level as a function of the combined power or in terms of the power ratio between the carriers.

Fig. 4.7 shows the intermodulation level as a function of the applied torque to the screws for the connection of two particular silver-plated waveguides. It can be seen that the decrease of the PIM level with the applied torque was not so important as in the case of the aluminium waveguides. In fact, the intermodulation level remained quite torque-independent almost in all the cases.

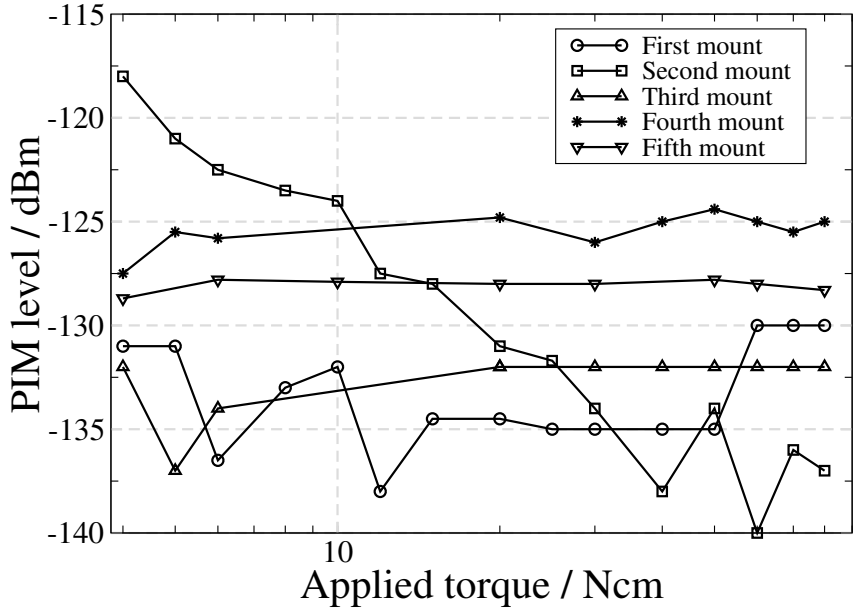

Figure 4.7: *PIM level versus applied torque for silver-plated aluminium waveguides. P = 340 W.*

Two different silver-plated waveguides were tested in order to check if this behaviour was repeatable (results in Fig. 4.8). It was found that, as before, the intermodulation level kept more or less constant independently of the applied torque.

This behaviour can only be explained by three facts:

1. The PIM level measured was not generated at the investigated flange but in the flanges between the device under test (DUT) and the test set-up.

2. The intermodulation level was produced by the waveguides themselves and not by the junction.

3. The PIM level was originated at the junction but a kind of saturation situation was reached.

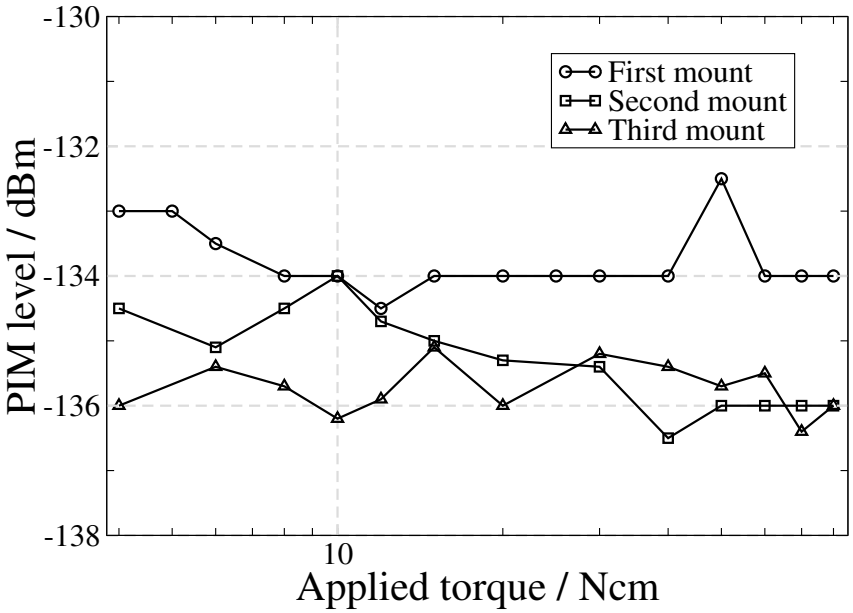

Figure 4.8: *PIM level versus applied torque for silver-plated aluminium waveguides. P = 340 W.*

The first and the second options are discarded because a gasket was introduced between the flanges showing that the PIM level could be driven below the noise floor. Furthermore, the second possibility is even more unlikely since all the components in the test set-up were manufactured by the same company (Tesat-Spacecom GmbH & Co. KG), following the same process as for the tested samples. Hence, it is clear that the intermodulation level was not generated at any other part of the system but at the tested connection.

Thus, the only feasible explanation is related to the third point. It is possible that the connection at low torques is already so good (very low PIM levels) that no improvement is achieved by application of higher torques. However, this is suspicious because the rest of connections in the test set-up were also silver-plated junctions and a lower intermodulation level was achieved (noise floor). The difference between the tested connection and the other waveguide junctions forming the test set-up in the critical zone (between the input and the output diplexer) was that the latter were eight hole flanges together with a high pressure configuration. Such a configuration has a lower distance between screws allowing for a better contact. In fact, those flanges have a distance between bolts always lower (or very close) to $2 \cdot r_c$. Song et al. [109] have shown that the contact resistance of bolted clean connections is basically torque independent and is directly related to (4.1). This is in agreement with the PIM data obtained for silver-plated aluminium waveguides, for which the intermodulation level does not vary significanly with the applied torque.

Aluminium gaskets

Aluminium gaskets were inserted between the silver-plated aluminium waveguides. The PIM response is shown in Fig. 4.9. Again, it is observed that at the highest torque value the insertion of the gaskets did not result in a higher PIM level except for the bridged gaskets (as in the case of aluminium waveguides). In fact, for the flat gaskets case (one or two) the PIM level was sometimes lower than the pure waveguides connection. Such a behaviour is rather surprising since it means that the silver waveguides connection produces a higher intermodulation level than two silver-aluminium contacts if a gasket is used. Moreover, the results in the case that two gaskets are employed are quite good even considering that an aluminium-aluminium connection is present. This is understood, again, by the increase of seal of the junction caused by the increment of the overall contact pressure.

Silver-plated gaskets

As shown in Fig. 4.10 the insertion of silver-plated gaskets (flat or bridged) did not improve the PIM response of the system. In fact, exactly the same intermodulation level was measured (around -135 dBm) at high torques. Even the bridged gaskets, where the RF path zone is tightly joined, could not improve the intermodulation level. However the use of two gaskets at a time reduced the PIM level around the noise floor for all the cases, indicating again that the mechanical improvement of the connection is extremely important in the reduction of the intermodulation level of bolted waveguide connections. It is also found that the PIM response of the silver-plated waveguide connection is not changed due to the test campaign (see Fig. 4.10(d)).

Additional measurements

Hard gold gaskets presented a similar response to silver ones. Fig. D.5 shows that the PIM level converged to the ”saturation” level for the cases of flat and bridged gaskets. The insertion of two gaskets resulted in an intermodulation level slightly better (around -140 dBm) than the ”saturation” value at high torques.

Beryllium-Copper gaskets showed intermodulation levels slightly higher than silver and hard gold gasktes (see Fig. D.6). Only the bridged gaskets presented a similar behaviour since the ”saturation” level was recovered. However, the use of two gaskets or of the flat gaskets did not improve the response of the system.

Indium gaskets insertion (Fig. D.7) did not improve the PIM level of the connection. This is extremely important because confirms that the intermodulation level measured at the connection was independent of the coating material applied. This is true for connections like those formed by silver-plated waveguides whose surface is soft and clean enough.

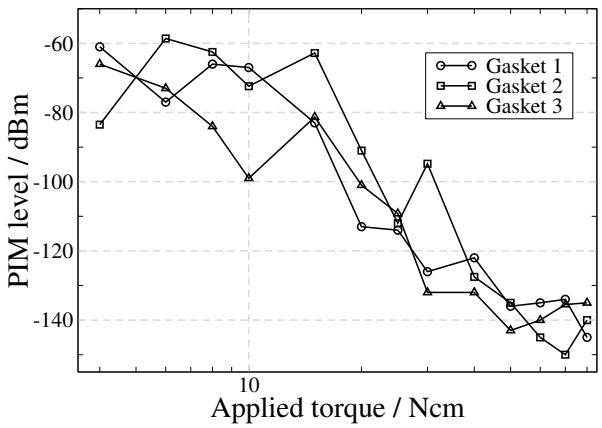

(a) *PIM level versus applied torque when one flat gasket is inserted.*

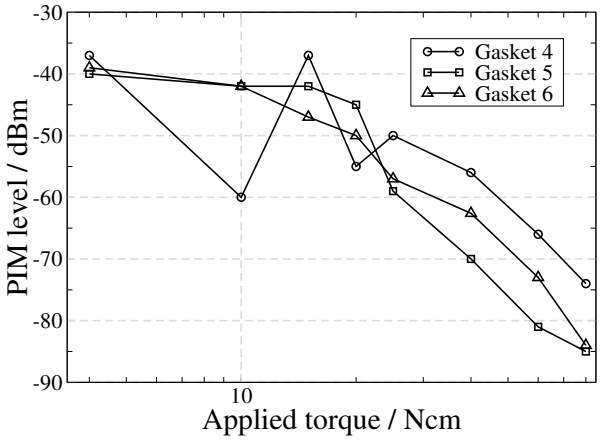

(b) *PIM level versus applied torque when one bridged gasket is inserted.*

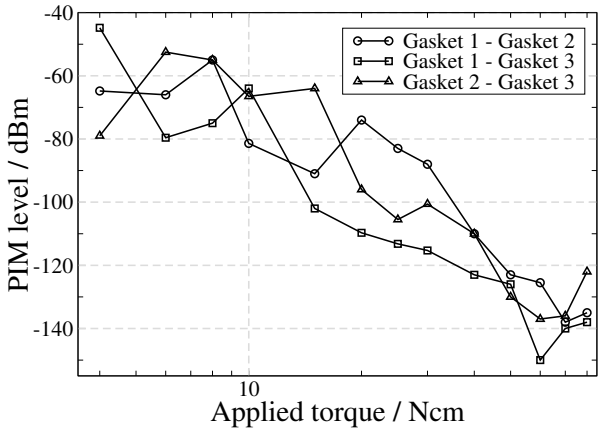

(c) *PIM level versus applied torque when two flat gaskets are inserted.*

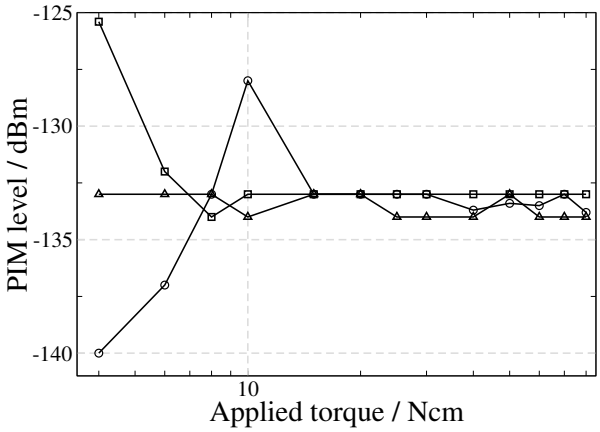

(d) *PIM level versus applied torque without gaskets.*

Figure 4.9: *Effect of inserting aluminium gaskets on the junction, P = 340 W.*

Summary of silver-plated aluminium waveguide connections

Conclusions in relation to the PIM data for silver-plated connections can be extracted:

1. Silver-plated waveguides show, as expected, lower PIM levels than aluminium contacts. In fact, the intermodulation level generated can be detected thanks to the exceptional quality of the test set-up employed.

2. The importance of reaching high pressures in such contacts is secondary. From a particular torque value, the PIM level becomes rather torque-independent. It is more important to have a relatively low pressure - enough to form a-spots - but more distributed.

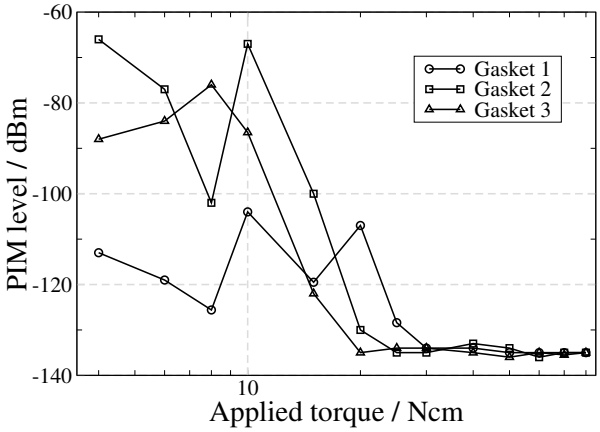

(a) *PIM level versus applied torque when one flat gasket is inserted.*

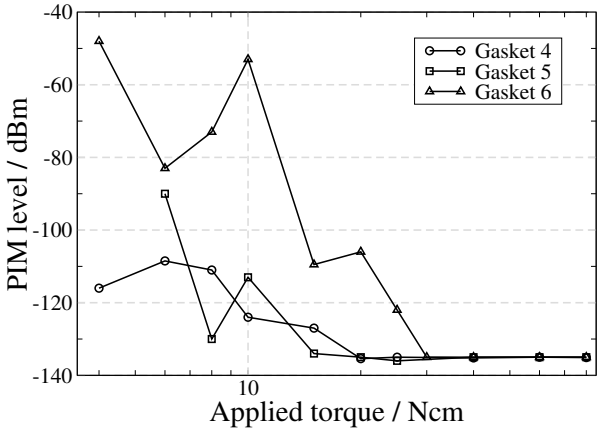

(b) *PIM level versus applied torque when one bridged gasket is inserted.*

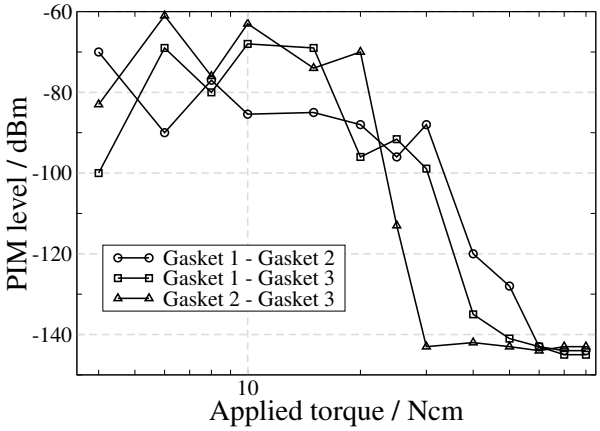

(c) *PIM level versus applied torque when two flat gaskets are inserted.*

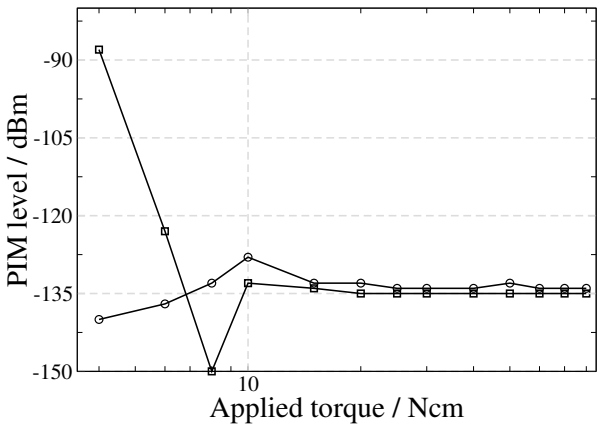

(d) *PIM level versus applied torque without gaskets.*

Figure 4.10: *Effect of inserting silver-plated aluminium gaskets on the junction, P = 340 W.*

3. The test campaign does not affect the PIM response of the waveguide connection significantly.

4. The application of two silver gaskets results in the lowest PIM levels at high torques. Moreover, in opposite to the behaviour of aluminium waveguides, the insertion of very soft gaskets (indium) does not improve the intermodulation level of the connection. This emphatizes the fact that the mechanical configuration of the connection is more important than the material/surface properties, provided the metal has good contact properties (like silver, gold, BeCu,...).

Chapter 5

Corona discharge basics

This chapter is devoted to present a full understanding of the physics lying behind the corona discharge in microwave devices. The basic mechanisms which control the discharge process are described. In particular, their dependence on the applied electric field, the environment pressure and the frequency is discussed. Moreover, phenomenological expressions are formulated for the quantitative characterisation of these mechanisms in the cases of air and nitrogen. Additionally, the main equation governing the corona discharge phenomenon is expounded, justified and simplified for our particular application. Finally, some specific factors which can affect a corona discharge are presented and their effect on the breakdown onset value is outlined.

5.1 Corona Discharge Physics

Corona Discharge is a balance process among different physical mechanisms involving electron dynamics inside gases. The main phenomenon contributing to the increase of the free electron density is the ionisation of the gas molecules. On the contrary, several mechanisms inhibit the development of the electron plasma formation by reducing the number of free electrons in the gas: diffusion, attachment and recombination are, in any situation concerning Sat-Com applications, the most relevant. Their importance depends on several factors like electric field, pressure and frequency. Needless to say that for each particular gas the dependence of the different physical corona mechanisms on these parameters varies.

In the following, all these physical processes are described and their impact in the corona discharge threshold is underlined. Remarks concerning particular aspects applicable to Sat-Com are done. Special attention is paid to *air* and *nitrogen* since air is indeed the gas filling the components during operation, whereas nitrogen is used in many Sat-Com laboratories to perform the breakdown tests.

5.1.1 Ionisation

Ionisation is the process by which electrons are extracted from a molecule/atom. To achieve this, the colliding electron must transfer enough energy to the molecule in order to overcome the binding energy of the electron to it. If this energy is not high enough, an elastic collision can occur (no energy is transfered and the colliding electron does not lose energy) or an inelastic collision (energy exchange) that excites the atom, which finally results in the radiation of energy from the atom when it returns to its ground state. The ionisation reaction for a specie M is

$$e^- + M \rightarrow 2e^- + M^+.$$

For instance, the ionisation potentials for the two major constituents of air, N_2 and O_2, are 15.6 eV and 12.1 eV [110] respectively, i.e., in order to have a noteworthy probability of electron extraction from these molecules, the energy of the impacting electron must be higher than these values. Thus, it is clear that high electric fields result in a higher ionisation rate since more energy is transfered to electrons in the surrounding gas. If this rate is high enough to overcome losses due to other mechanisms (see following sections), an avalanche process can be ignited resulting in the formation of an electron plasma, i.e., a corona discharge occurs.

If the electron losses are negligible, the growth of the free electron density (n) with time is given by

$$\frac{dn}{dt} = \nu_i n,$$

where ν_i is the ionisation rate which provides the number of ionisation events occurring per second.

5.1.2 Diffusion

Inside a gas receptacle, diffusion occurs due to the tendency to reduce any kind of gradient existing in it. For instance, if a higher density of molecules is present in one side of a gas container, a mass flux appears in order to reduce this difference. In the same sense, if a charge imbalance exists, charges move to neutralise this charge gradient.

In *free space*, the diffusion of electrons is directly related to the scattering cross sections of the molecules in the gas. Ionisation occurs in high field regions and hence, wherever a high-field region surrounded by a low field is present, an electron current will flow from the high-field zone to the low-field one in order to compensate the charge "generation" in the high-field region. The ability of a gas to diffuse is very pressure dependent. At high pressures, electrons find many obstacles in its path to the low-field region, and therefore, diffusion is inhibited. However, at low pressures, the mean free collision path of the electrons can become larger than the high-field region size and thus, electrons diffuse freely.

Mathematically, the diffusion process can be analysed by means of a continuity equation for the electron density. In the case that only diffusion and ionisation are considered, the equation [23]:

$$\frac{dn}{dt} = D\nabla^2 n + \nu_i n \tag{5.1}$$

defines the problem, where D is the diffusion coefficient, which has been taken as constant, i.e., it is assumed that D is space-independent.

This equation can be solved by separation of variables assuming that the ionisation rate is space and time independent resulting in an exponential solution:

$$n = n_0 e^{(\nu_i - \gamma)t}, \tag{5.2}$$

where γ is the integration constant of the separation of variables method, which is:

$$\gamma = -D \cdot \frac{\nabla^2 n}{D}. \tag{5.3}$$

Let consider, for instance, a rectangular metallic cavity of dimensions a, b, c. In the fundamental harmonic, the solution to (5.1) reads:

$$n = n_0 \sin\left(\frac{\pi x}{a}\right) \sin\left(\frac{\pi y}{b}\right) \sin\left(\frac{\pi z}{c}\right). \tag{5.4}$$

This leads to the following value of γ:

$$\frac{\gamma}{D} = \left(\frac{\pi}{a}\right)^2 + \left(\frac{\pi}{b}\right)^2 + \left(\frac{\pi}{c}\right)^2. \tag{5.5}$$

Since $\frac{\gamma}{D}$ has dimensions of the inverse of the distance, MacDonald defined a characteristic diffusion length as

$$\frac{\gamma}{D} = \frac{1}{\Lambda^2}, \tag{5.6}$$

and, thus, the diffusion process becomes fully dependent on the geometry. If one of the dimensions is much larger than the rest (parallel plate approximation), the diffusion length is just the plate separation divided by π.

This approach is of course limited to the cases in which the pressure is high and electrons do not diffuse out of the high field region, or for those cases in which the pressure is very low and electrons diffuse freely being absorbed in the metallic walls of the device. Even more critical, the definition of the characteristic diffusion length is only possible for uniform fields. If the field becomes highly non-uniform (as occurs inside complex devices), a more general treatment based on numerical techniques must be followed.

In the case of Direct Current (DC) excitation, the electric field transfers all its energy to the electrons and, as a consequence, there is no dependence of this transfer with ambient

conditions such as pressure. However, when a microwave field is applied, the transfer of energy is field (frequency) and ambient conditions (pressure) dependent [23]. An effective field that takes this into account can be defined [23]:

$$E_{eff} = \frac{E_{rms}}{(1 + \frac{\omega^2}{\nu_c^2})^{1/2}} \tag{5.7}$$

where E_{rms} is the root mean square electric field, $\omega = 2\pi f$ and ν_c is the electron collision frequency, which provides the number of electron collisions per second.

The effective field has a very useful meaning since it allows to relate the DC and the AC corona properties. The corona characteristics of an AC field of amplitude $(2E_{rms})^{1/2}$ are equivalent to those of a DC electric field equal to E_{eff}. Therefore, DC experimental data can be used for the AC case just exchanging E_{eff} by $(2E_{rms})^{1/2}$. However, there are intrinsic differences between the DC and the AC discharge process. In the first case, a dependence exists on the surface properties of the cathode/anode since the electrons are accelerated always in the same direction impacting, eventually, into the cathode. In the second situation, electrons hardly move from their initial position (if the electric field wavelength is smaller than the mean free electron path), and the discharge basically depends on the properties of the gas and the geometry of the device.

Another important remark to be considered in order to understand the corona discharge phenomenon in terms of pressure and frequency is directly related to ν_c. At very high frequencies, many oscillations occur before an impact takes place. On the contrary, at very low frequencies, many collisions occur before an oscillation of the field elapses. The optimum state, at which one impact occurs per oscillation is given by $\nu_c = \omega$. Since the electron collision frequency is related to the pressure (the higher the pressure, the larger the number of collisions per second), one can define a particular pressure for which this occurs as a function of the RF field frequency.

The behaviour of the corona discharge breakdown at one side or the other of this "resonance" is clearly different. At low pressures, the collisions of the electrons with the molecules occur out of phase, which means that the electrons do not have their maximum energy at the moment of the impact. Therefore, a higher field is necessary in order to ionise the molecules. Moreover, there are few molecules in the gas and, thus, few collisions take place preventing the electron plasma to be formed since not enough electrons are freed. At very low pressures, what indeed happens is that the electron mean free path is larger than the dimensions of the device and therefore, collisions to the walls take place. In this regime, multipactor breakdown [111] instead of corona can occur. At high pressures, the transfer of energy from the electric field to the electrons is optimum. However, the energy of the electrons is so high that almost all the collisions are elastic.

For instance, in the case of air, a good approximation to ν_c is [23]:

$$\nu_c \approx 5 \cdot 10^9 p \tag{5.8}$$

where p is the pressure in torr[1]. Thus, if a microwave field of 10 GHz is considered, one would expect to have the "resonance" for a pressure of 10 torr. The pressure at which this occurs is the so-called critical pressure for which the field necessary to breakdown the gas is minimum.

All these facts lead to the well-known Paschen curve where the corona breakdown level is plotted versus the pressure, as shown in Fig. 5.1. For low and high pressures, a very high electric field is needed to ignite the corona discharge (electric fields which are beyond the values reached in microwave components). Nevertheless, for pressures close to the critical pressure, the breakdown electric field is dramatically reduced, increasing the risk of corona discharge.

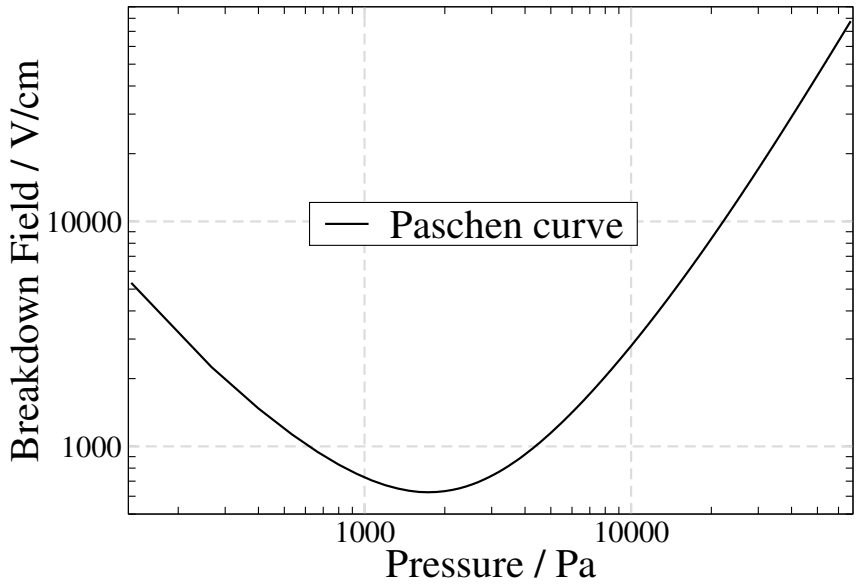

Figure 5.1: *Example of Paschen curve: breakdown level as a function of the environment pressure.*

Apart from free diffusion, the so-called ambipolar diffusion can also take place. Ambipolar diffusion occurs when the concentration of ions and free electrons is relatively high. In this situation, the electrostatic forces between the positive and the negative particles are considerable and thus, a space charge is formed in such a way that electrons and ions

[1] 1 torr = 1.33 mBar = 133.32 Pa. The unit in the international system for pressure is Pascal (Pa). It will be used along this thesis. However, in many cases, the units torr or mBar will be employed depending on their use in the literature.

do not diffuse separately but as a whole. This results in a reduction of the diffusivity of electrons and consequently, in a lower breakdown onset, since less free electrons are ”lost”.

In normal situations, free diffusion is much higher than ambipolar diffusion and therefore, the latter is usually neglected. Only when the gas is in a pre-ionised state with a high free electron density present, ambipolar diffusion is important. Normally, this occurs only after the corona discharge and, for this reason, ambipolar diffusion is commonly not considered.

5.1.3 Attachment

Attachment refers to the process in which electrons are absorbed by a neutral molecule forming an ion. Ions do not take part in the breakdown phenomenon due to their high mass. Because of this, they can not be accelerated for the electric field ranges available in Sat-Com applications. Therefore, attachment is a loss process increasing the breakdown level threshold. The capability of a molecule to attach electrons depends on the degree of fullness of its external electronic layers. The fuller they are, the higher the probability of attachment. This fullness is quantitatively given by the electron affinity of the atom/molecule. Negative electron affinity means that the molecule releases energy when an electron is attached to it and hence, electrons are easily trapped by such a molecule. For instance, oxygen is a highly attaching molecule whereas nitrogen - with a positive electron affinity - hardly attaches electrons.

Attachment can be a two body or a three body process. The two body mechanism dominates if a high electric field is applied whereas the three body situation is dominant if no field or a very low one is present. For this reason, in almost any situation of interest, the two body attachment is much more relevant than the three body case.

The two body attachment reaction is:

$$e^- + A + E(eV) \rightarrow B + C^-,$$

where E(eV) refers to the energy required to unbound the molecule A. The reaction products are a neutral molecule (B) and an ion (C^-). For instance, in the case of O_2, $E(eV)$ = 3.6 eV and $B = C = O$.

In the case of three body attachment, the process is, for instance, in the case of O_2:

$$e^- + O_2 + M \rightarrow O_2^- + M$$

where the molecule M is normally O_2, N_2 or H_2O in the case of air.

Thus, it is clear that, at low electric fields, the dominant attachment mechanism is the three body attachment since no additional energy is necessary to ignite the reaction. Moreover, both the two body and the three body attachment rates increase with the pressure since more molecules are present and therefore, more reactions can occur. For the low pressure range, few collisions take place and consequently, the attachment rate is low. This explains why attachment is less important than diffusion for the pressure range of interest in Sat-Com applications.

5.1.4 Recombination

Recombination is the interaction of an electron with a positive particle resulting in a neutral state. In other words, after an ionisation event, a free electron can "recombine" with a positive ion. Hence, the probability for a recombination event to occur is directly related to both the electron and the ion densities. Recombination can be dissociative or radiative. The radiative reaction can be schematically written as

$$e^- + M^+ \rightarrow M + \hbar\omega,$$

whereas the dissociative recombination process is

$$e^- + AB^+ \rightarrow A + B.$$

In those cases where no other mechanisms are considered, the free electron losses due to recombination can be expressed as

$$\frac{dn}{dt} = -\beta_r n n_i,$$

where dn/dt is the time variation of the free electron density due to recombination of electrons, β_r is the recombination rate, n is the electron density and n_i the ion density.

Hence, recombination becomes relevant when a sufficient amount of electrons and ions is present in the gas. Since this normally happens when the discharge has already started, recombination can be neglected in the determination of the breakdown onset.

5.1.5 Free electron production rate

One of the most difficult tasks when emulating real conditions of devices in operation is the determination of the free electrons production rate. From a physical point of view, the production of electrons is mainly caused by the solar radiation arriving to the atmosphere and, in a second extent, by the cosmic rays colliding in the upper layers of the atmosphere, which results in a particle cascade process in which electrons, as well as other particles like muons or neutrinos, are produced [112]. Moreover, the electron density in the atmosphere extremely depends on the altitude above the sea level. The typical profile of the free electron density along the atmosphere height is shown in Fig. 5.2. This profile is known

as Chapman layer [113]. It is seen how the maximum occurs for a height around 110 Km, which corresponds to a range pressure around 2000 Pa which, by chance, is very close to the critical pressure region for the case of microvave frequencies.

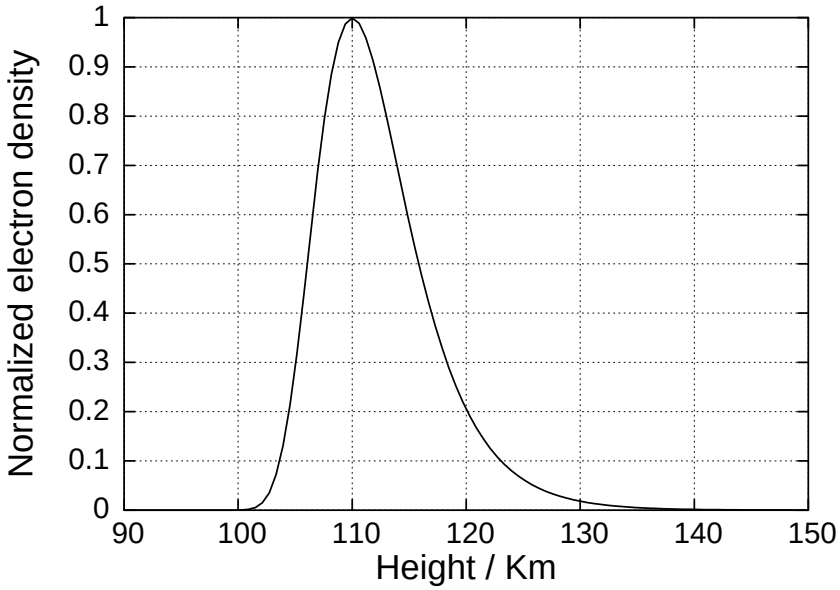

Figure 5.2: *Free electron density profile in atmosphere.*

The explanation of this free electron density profile is quite simple. At high altitudes, the gas density is low and ,consequently, few molecules can be ionised. Descending in altitude, the atmosphere density increases and therefore, more and more molecules can be ionised. The peak is produced because the radiation is being absorbed along the atmosphere and, thus, at low altitudes less ionisation events indeed occur.

Fortunately, from the corona onset computation point of view, the impact of this parameter is secondary due to the exponential nature of the electron growth for power levels slightly larger than the breakdown power.

5.2 Corona Discharge equation

The equation governing the whole corona discharge process can be written based on all the physical mechanisms related to electron freeing and absorption described in the previous section. In particular, a generalisation of the continuity equation in (5.1) involving all these production/loss mechanisms mathematically describes the time evolution of

the free electron density [23], [24]:

$$\frac{\partial n}{\partial t} = \nabla(D\nabla n) - \vec{v}\cdot\nabla n + (\nu_i - \nu_a)n - \beta n^2 + P, \tag{5.9}$$

where ν_i and ν_a are respectively the ionisation and attachment rates, D is the diffusion coefficient, β is the recombination coefficient and P is the production rate of electrons from external sources. The time derivative provides the evolution of the electron density, $\nabla(D\nabla n)$ is the diffusion term, which is space dependent, and the convective term $\vec{v}\cdot\nabla n$ takes into account the possible motion of the gas.

In the particular case under investigation some systematic simplifications can be done without loosing generality. First of all, the recombination term can be neglected since it is only of relevance once the electron density is high enough, which only occurs when the discharge has already started. Moreover, the convective term can be also neglected since a stationary medium is assumed. Additionally, the diffusion coefficient can be considered space-independent since it has been chosen field independent. The simplified equation finally becomes:

$$\frac{\partial n}{\partial t} = D\nabla^2 n + (\nu_i - \nu_a)n + P, \tag{5.10}$$

which is, in fact, the equation that is going to be solved throughout this work.

5.3 Diffusion, ionisation and attachment for air and nitrogen

From the previous sections, it is clear the importance of a proper characterisation of the aforementioned processes in order to predict the corona discharge onset in passive components. However, there are no analytical expressions derivable for each particular gas which provide the dependency of these mechanisms on system parameters like pressure, electric field or frequency. Hence, the only option remaining is taking phenomenological expressions which fit to experimental data. Using these results and solving the continuity equation of the electron plasma (5.10), the corona discharge threshold can be predicted. In particular, air and nitrogen are considered since they are the most relevant in Sat-Com applications.

5.3.1 Air

As mentioned, the case in which the gas filling the microwave component is air is studied in more detail. Basically, air is a mixture of gases. Approximately 78% nitrogen and 21% oxygen with a few percent of other molecules like water vapour, carbon dioxide, nitrogen oxide or argon. All the expressions presented along this section are extrictly valid for dry air.

First of all the diffusion coefficient for air, according to [23] and [25], is taken as electric field independent:

$$D = \frac{10^6}{p}\,[cm^2 s^{-1}]. \tag{5.11}$$

The electron collision frequency is taken from [23] as

$$\nu_c = 5 \times 10^9\, p\,[s^{-1}]. \tag{5.12}$$

It is important to realise that both D and ν_c are not the typical values that can be found in books (see, e.g., [24]) which are taken at zero electric field. These are effective values which can describe the system behavior for the typical electric fields of breakdown.

A suitable phenomenological expression for the ionisation rate (ν_i) can be extracted from experimental results in [25] and can be expressed as:

$$\nu_i = 5.14 \times 10^{11}\, p \exp(-73\alpha^{-0.44})\,[s^{-1}], \tag{5.13}$$

with:

$$\alpha = \frac{E_{rms}}{p(1+\omega^2/\nu_c^2)^{1/2}} \equiv \frac{E_{eff}}{p}. \tag{5.14}$$

Expression (5.13) holds for $32 < \alpha < 100$.

Following again the measurement data from [25], the two body attachment rate (ν_{a2}) is:

$$\nu_{a2} = 7.6 \times 10^{-4}\, p\,\alpha^2(\alpha+218)^2\,[s^{-1}], \tag{5.15}$$

which is accurate in the range $0 < \alpha < 60$.

The three body attachment (ν_{a3}) can be taken field independent as [114]:

$$\nu_{a3} = 10^2\, p^2\,[s^{-1}]. \tag{5.16}$$

Fig. 5.3 shows the ionisation and the attachment rates ($\nu_a = \nu_{a2} + \nu_{a3}$) for dry air as a function of α. It is to be noticed the common point where both mechanisms are equal. The only physical process releasing electrons is ionisation whereas diffusion and attachment are the electron loosing mechanisms. It is therefore clear, by inspection of Fig. 5.3, that the discharge can only occur if α is greater or equal than the crosspoint value. At high pressures, where diffusion is negligible, this crosspoint directly drives to the electric field threshold for corona discharge. As seen in Fig 5.3, the common point occurs for $\alpha = 32\,[Vcm^{-1}torr^{-1}]$, which results in the well-known relation for ionisation breakdown at sea level [25]:

$$E_{break} = 32 \cdot p\,[Vcm^{-1}]$$

On the other hand, at low pressures - where diffusion losses are much more important - this crosspoint only results in a very conservative breakdown onset.

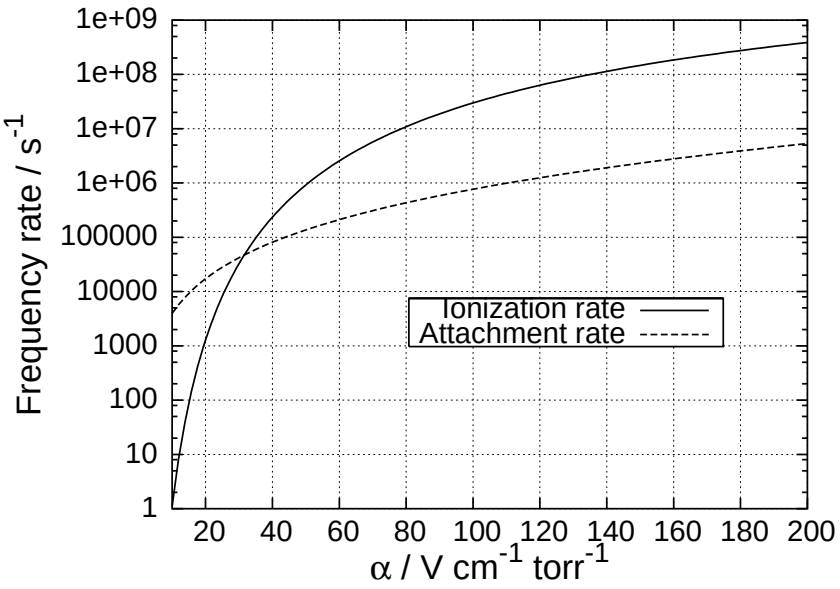

Figure 5.3: *Ionisation and attachment rates for dry air.*

5.3.2 Nitrogen

N_2 is extremely important since it is generally used for performing tests instead of air because of its stability and because the breakdown is close to air around the critical zone [23]. In the following, all the physical mechanisms are quantitatively defined in order to predict the corona onset in N_2.

On the one hand, the electron collision frequency for N_2 is:

$$\nu_c = 8.1 \cdot 10^9 \, p \, [s^{-1}]. \tag{5.17}$$

On the other hand, the diffusion coefficient for N_2 is taken as:

$$D = \frac{1.4 \cdot 10^6}{p} \, [cm^2 s^{-1}]. \tag{5.18}$$

In the case of N_2, no phenomenological expressions have been found in the bibliography for the ionisation rate. Nevertheless, the siglo-database [115] provides the measured Townsend's first ionisation coefficient (α_i) for different values of α. Moreover, the electron mobility (μ_i) is also provided and therefore, the ionisation rate can be calculated from the following relationship [23], [24]:

$$\nu_i = \alpha_i \cdot \mu_i \cdot E. \tag{5.19}$$

Using the experimental values of α_i and μ_i in the siglo-database [115], two functions have been fitted to these data which allow the computation of these parameters for any

electric field. Fig. 5.4 shows the experimental data and the curve fitted to them. From these fittings, the ionisation coefficient and the mobility become

$$\alpha_i = 39.1\, p \cdot \exp(-106.8\, \alpha^{-0.692})\, [cm^{-1} torr^{-1}], \tag{5.20}$$

and

$$\mu_i \cdot p = 3.297 \cdot \exp(12.127\, \alpha^{-0.0236}) - 101.346\, \alpha + 1 \cdot 10^5\, [V^{-1} s^{-1} cm^2 torr]. \tag{5.21}$$

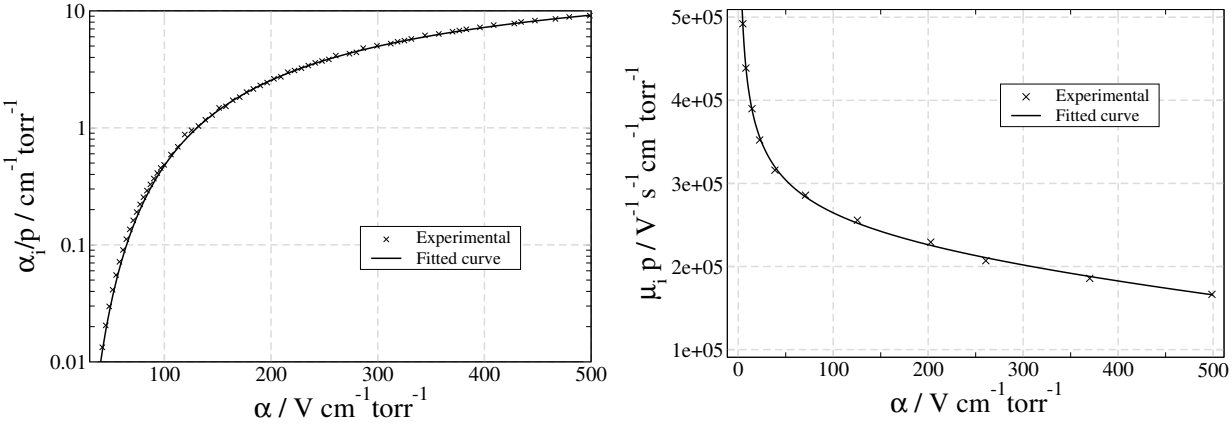

(a) Ionisation coefficient of N_2.

(b) Electron mobility of N_2.

Figure 5.4: *Siglo-database [115] fitted to the curves used in this work.*

Using (5.20) and (5.21) in (5.19), the ionisation rate finally results in:

$$\nu_i = 129\, p \exp(-106.8\alpha^{-0.692}) \cdot \left[\exp(12.127\alpha^{-0.0236}) - 101.346\alpha + 1 \cdot 10^5\right] \cdot \alpha\, [s^{-1}]. \tag{5.22}$$

As already mentioned, one of the most important properties of N_2, as far as its breakdown properties are concerned, is its positive electron-affinity. As a consequence, N_2 hardly attaches electrons easily and, thus, one can effectively consider that

$$\nu_a = 0, \tag{5.23}$$

for the electric field range of interest. Even if ν_a were not zero, it could be neglected because it would always be insignificant in relation to ν_i.

Using the air characteristics (5.11 to 5.16) and the nitrogen ones (5.17 to 5.23), both gases can be compared in terms of breakdown threshold. To do this, the relevant parameter to be used is $(\nu_i - \nu_a)/D$, which provides the corona susceptibility of a particular gas. Such a parameter comprises all the mechanisms involving the discharge, completely characterising the breakdown; the larger its value, the lower the breakdown onset for a

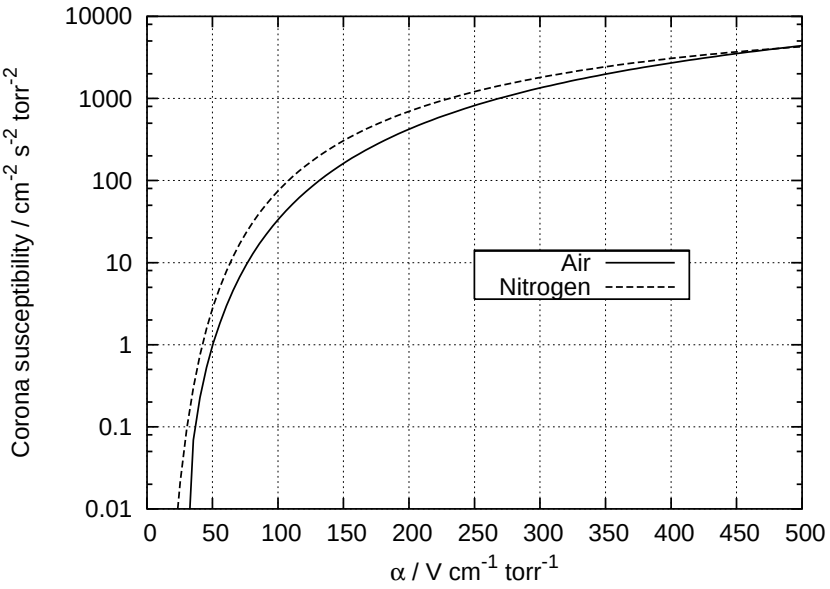

Figure 5.5: *Comparison between corona susceptibilities for air and nitrogen.*

particular gas. Fig. 5.5 shows this parameter for both gases. It is seen how nitrogen presents a slightly larger susceptibility except for large values of α, for which both contributions become very similar.

All the necessary properties in order to characterise the corona discharge in the presence of air or nitrogen have been presented. Using them, the corona threshold can be determined in terms of the microwave frequency and/or the environment pressure, as explained in the next chapter.

5.4 Factors affecting the breakdown threshold

In this section, several factors which can affect the corona onset are outlined. In particular the magnetic field and the temperature are analysed. For each parameter, its impact in the breakdown threshold is described.

5.4.1 Magnetic field

In previous analysis on microwave filters and resonators, this effect has not been considered (see e.g. [37]). The reasons for this are that the analysis becomes much more complex and that the results are only affected at low pressures ($p < 30 torr$) [23]. However, it is in this range where the critical pressure of the Corona breakdown is located and where it has relevance for Sat-Com applications. This worry is even more dramatic if it is taken into account that the presence of the magnetic field results in a lowering of the

corona breakdown level [23] and, therefore, if not considered, the predicted breakdown can be much higher than the experimental one.

The influence of the magnetic fields in the corona discharge is twofold: firstly, the magnetic field influences the efficiency in the transfer of energy from the field to the electrons, and secondly, the diffusion is altered because the electrons paths become helicoidal. The first factor leads to a modification of the effective field of (5.7) by including the cyclotron resonance. This results in [23]:

$$E_{eff}^2 = \frac{E^2}{2}\left[\frac{1}{1+\frac{(\omega-\omega_b)^2}{\nu_c^2}} + \frac{1}{1+\frac{(\omega+\omega_b)^2}{\nu_c^2}}\right], \tag{5.24}$$

where

$$\omega_b = \frac{e}{m}|B|,$$

e being the electron charge, m the electron mass and B the magnetic flux amplitude. Obviously, the original definition of the effective field is recovered when the magnetic field vanishes, since (5.7) is retrieved.

The second effect is the change in diffusion. Following again MacDonald [23], one has to define a different diffusion coefficient for each field component in terms of the magnetic field. The different diffusion coefficient components can be expressed as:

$$D_i = D\frac{b_i}{\sqrt{(1+\overline{b}^2)}}, \tag{5.25}$$

where

$$b_i = \frac{\omega_{bi}}{\nu_c},$$

and

$$\overline{b} = \sqrt{(b_x^2 + b_y^2 + b_z^2)}.$$

Fig. 5.6 shows the influence of the magnetic field for a particular case of a device operating at 7 GHz. It is seen how, for high pressures, the impact of the magnetic field in the breakdown threshold is negligible. However, as pressure is decreased the effect becomes more and more important because the electron mean free path is larger and therefore, the magnetic field strongly curves the electron trajectories. Nevertheless, the magnetic field necessary for this to happen is quite large. In fact, the impact of the magnetic field can be neglected since inside of the microwave components investigated in this work it is always too small in order to have a relevant effect.

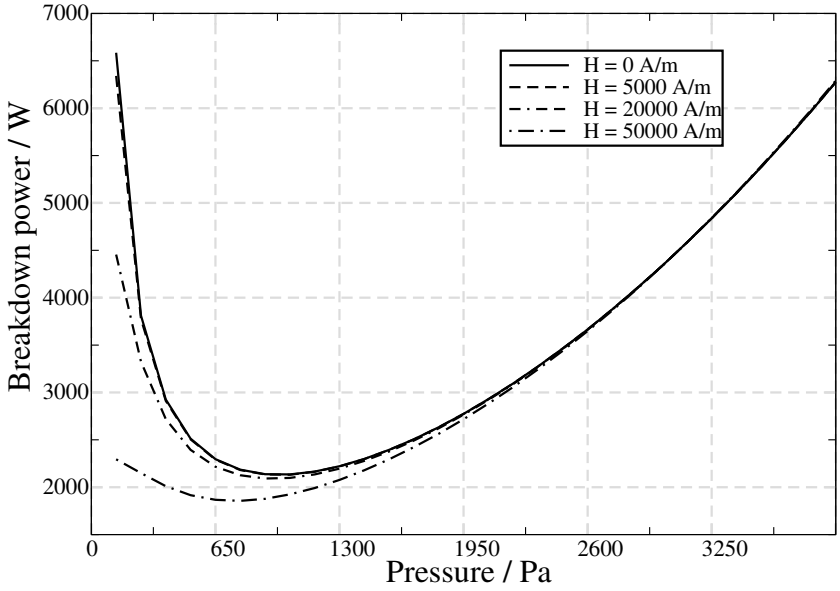

Figure 5.6: *Paschen curve: breakdown level as a function of the magnetic field H.*

5.4.2 Temperature

Temperature aspects are important in microwave devices for Sat-Com applications. This is due to the fact that the environment conditions and/or the high energy density that can be present in relatively small regions inside of the components can importantly alter the temperature of the gas in it. Thus, an analysis of the influence of the temperature in the corona breakdown is important in order to establish realistic margins between the measured onset in laboratory conditions and the breakdown during operation.

First of all, it is important to notice that although pressure is always taken as the parameter when analysing the corona discharge threshold, the parameter to take into consideration is, indeed, the gas density. Thus, if a pressure p is taken, it is implicitly assumed that the gas density is:

$$N = 2.687 \cdot 10^{19} \left(\frac{p}{760}\right) \cdot \left(\frac{273}{T}\right) [part./cm^3]. \tag{5.26}$$

Hence, when the pressure is kept constant and the temperature is changed, a variation in the gas density occurs. This has been considered by previous authors (e.g. [32]) defining an effective pressure as a function of the temperature:

$$p^* = \frac{T_0}{T} \cdot p, \tag{5.27}$$

where T_0 is taken as the room temperature.

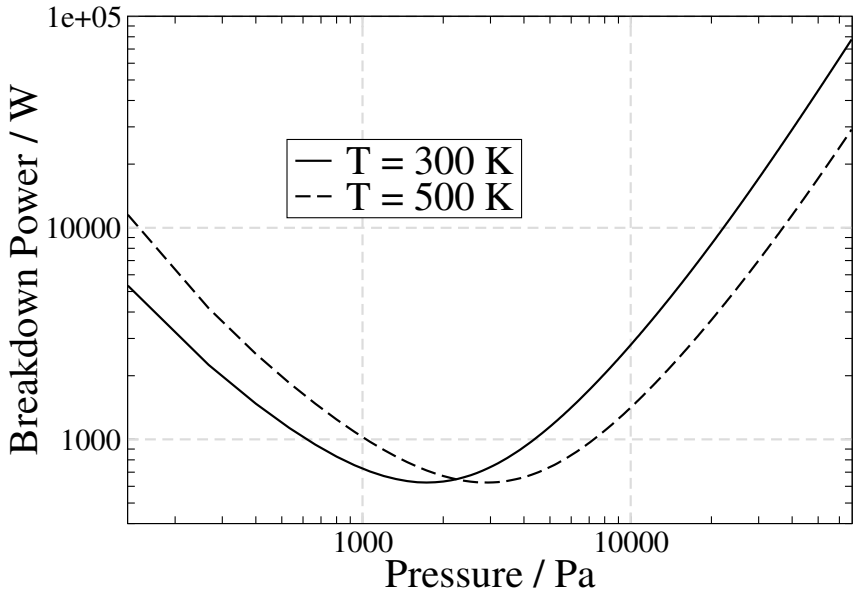

Figure 5.7: *Paschen curve: breakdown level as a function of the environment pressure for two different temperatures.*

This way, all the equations considered so far are valid for different temperatures just exchanging p by p^*. From (5.27), it is seen that the increase in temperature *does not reduce* the whole breakdown threshold but shifts the critical pressure to a lower pressure value. This leads to a decrease in the threshold at the right part of the Paschen curve and an increase at the left part of such a plot, as Fig. 5.7 shows. This is valid for air and nitrogen. The reason is that no significant change in the chemical composition of air and nitrogen occurs for temperatures below 2000 K.

However, in air, there is another effect for temperatures around 2000 K or higher, since nitride oxide (NO) molecules are produced according to:

$$\tfrac{1}{2}N_2 + \tfrac{1}{2}O_2 + 21.4 \text{ kcal/mol} \rightarrow NO$$

Despite the fact that the NO concentration can not be too high (not more than 10 %), its ionisation potential (9.25 eV) is the lowest of all the species which form air and therefore, even a small concentration of NO molecules results in a high impact in the ionisation mechanism. In fact, for temperatures higher than 4000 K, the NO molecules completely dominate the ionisation process.

Nevertheless, for reaching temperatures around 2000 K, very special conditions are necessary [32]. In particular, foreign particles can be present inside of the component which can heat up locally the device until such a temperature range. As far as this work is concerned, the only temperature effect considered is the change in the gas density, i.e., (5.27) is used.

Chapter 6

Corona discharge breakdown calculation

In this chapter, different calculations of the corona discharge breakdown are presented. The main objective is presenting analytical and numerical techniques to solve (5.10). The breakdown criterion is given in terms of the type of excitation: continuous wave (CW) or pulse. The results are compared in order to remark in which situations CW and pulse considerably differ. Moreover, it is shown that for our particular application, the pulse breakdown is, indeed, a single pulse breakdown. The corona discharge equation is solved in two different ways: an analytical solution, based on assuming homogeneity of the electric field everywhere in the device, and a numerical solution, which considers the exact fields distribution. Finally, the problem of the field singularities on the corners is analysed, addressing, by means of particular computations, that it is not relevant for Sat-Com applications. This will be confirmed by the full simulations performed on the devices presented in the next chapter.

6.1 Breakdown Criterion

In this section, the corona breakdown criterion is defined in terms of the different system parameters. This is done for the cases of CW and pulse excitations. First of all, a breakdown criterion is required regardless the excitation type, i.e., the general condition/s that must happen for the development of the discharge. Obviously, the suitable parameter to be used is the free electron density within the device. Physically, the breakdown field (or power) threshold can be defined as the minimum field (or power) necessary to disturb the normal electromagnetic response of a particular device. It is therefore dependent on the electromagnetic field distribution within such a component. Additionally, it is also dependent on the particular gas filling the structure, since the response of a gas subjected to microwave radiation differs from one to another, as explicitly expounded in the previous chapter for the cases of air and nitrogen. Thus, it is not easy to define a general theoretical criterion valid for an arbitrary component filled with an arbitrary gas. Mathematically, it

is convenient to define the breakdown onset in terms of a threshold ratio between the free electron density after a time t and the initial background electron density n_0. To sum up, if condition

$$\frac{n(t)}{n_0} \geqslant \frac{n_B}{n_0} \equiv \chi \tag{6.1}$$

is satisfied, breakdown occurs. In (6.1), n_0 is the initial electron density prior to the application of any electromagnetic field and the ratio n_B/n_0 defines the breakdown criterion. Therefore, breakdown occurs when, for a particular time (t_B), the electron density has reached a threshold value such that the condition in (6.1) is fulfilled. The problem immediately arises related to the value of χ. On the one hand, the background electron density is not known. In fact, n_0 can vary several orders of magnitude between sea level and Ionosphere (see Fig. 5.2). It depends on the source of free electrons (P) and the electron losses difference when no external electric field is applied. On the other hand, the electron density breakdown value (n_B) is also unknown and basically depends on the electromagnetic field distribution in the component and on the gas filling it.

Thus, it is clear that the application of a general criterion valid in any situation becomes almost impossible. Fortunately, the impact of the chosen value of χ on the calculated breakdown is not critical since either it does not really enter in the breakdown equation or it enters logarithmically, as shown in the next sections.

6.1.1 Continuous Wave Breakdown calculation

The first case of operation under investigation is CW, i.e., in this excitation type the wave is of constant amplitude and frequency, and infinite in time.

The solution of (5.10) provides the electron density as a function of time. The breakdown criterion is based on the fact that the electron density grows very fast once more electrons are freed than absorbed. This can be easily seen if (5.10) is solved for the case of an attachment-controlled corona discharge case (diffusion can be neglected) and taking the electric field homogeneous in the structure ($\nu_i \neq \nu_i(x)$ and $\nu_a \neq \nu_a(x)$). Under these assumptions, (5.10) becomes:

$$\frac{\partial n}{\partial t} = (\nu_i - \nu_a)n, \tag{6.2}$$

whose solution is just:

$$n(t) = n_0 e^{(\nu_i - \nu_a)t}. \tag{6.3}$$

Hence, once the number of electrons freed due to the gas ionisation is slightly larger than the number of electrons lost because of their attachment to the gas molecules, an avalanche is instantaneously formed due to the exponential nature of the solution.

Therefore, the breakdown condition for the case of CW operation can be simplified to

$$\frac{dn}{dt} = 0. \tag{6.4}$$

As a matter of fact, this condition is conservative. Nevertheless, it provides a very accurate breakdown level at the range of pressures of interest. At higher pressures, where the plasma formation time rises, such an approach becomes too conservative and a significant error is introduced [37]. As a consequence of (6.3), the general equation (where diffusion is also considered) to be solved in order to determine the breakdown onset is

$$D\nabla^2 n + (\nu_i - \nu_a)n + P = 0, \tag{6.5}$$

which is stationary (time-independent).

The fact that the final equation to be solved is stationary simplifies its solution in the case of complex devices, for which resort has to be taken to numerical techniques. As an example, Finite Differences (FD) method instead of Finite Differences in Time Domain (FDTD) one can be applied. This has as a result an easiness of implementation from the computational programming point of view, and obviously, a more efficient numerical approach. Of course, to follow such a procedure to tackle the problem is extremely useful for the determination of the corona breakdown onset. However, the main disadvantage is that it is not possible to study the time evolution of the free electron density. From the high-power microwave component designer viewpoint, although, the knowledge of the breakdown power is sufficient in order to design a corona free device accomplishing the specific margins required.

6.1.2 Pulse breakdown calculation

In laboratory tests, the pulse excitation is sometimes used instead of the CW. This can be due to two reasons: using a pulse source, higher powers can be reached and/or it is not desired to damage the device under test (DUT). In the cases of an expected high breakdown level, the pulse source can feed the required power, whereas, if the DUT is a final prototype to be adapted to a satellite subsystem, the possible damage that could cause a high-power continuous signal can be avoided.

The first trivial fact that must be underlined is that the pulsed breakdown power must be always higher or equal to the CW breakdown power. This is obvious since the signal is not applied continuously. Indeed, the pulse breakdown level must tend to the CW onset when the pulse duration (PD) is very long. If the pulse duration is rather short, a higher power must be applied in order to ignite the discharge because during the inter-pulse time (pulse repetition interval (PRI)), no electric field is present, and therefore, electron losses are important.

The solution to (5.10) is much more complex in the case of pulse excitation since time considerations must be considered. Therefore, in order to simplify the numerical approach, when calculating the breakdown threshold for pulse operation the real aim is to determine it from a stationary problem.

For the case of pulse operation, it is useful to express the breakdown criterion in logarithmic form in terms of the effective ionisation rate ($\nu(t) = \nu_i - \nu_a - \nu_D$), making use of the exponential evolution of the free electron density above the breakdown onset. Therefore, from (6.3), one has that

$$\nu t_B = \ln\left(\frac{n_B}{n_0}\right), \tag{6.6}$$

provided that ν is constant until the breakdown time is reached. This is the general criterion that is going to be applied in the case of pulse excitation in the next sections. We can see how the uncertainty of the breakdown threshold ratio (n_B/n_0) enters logarithmically in the breakdown condition. In the next section, the impact of this uncertainty in the breakdown onset is quantitatively analysed. The typical range of values for this logarithm is between 20 and 40. In particular, for air it is commonly taken equal to 20 in the existing literature [116].

In the next two sections, the single-pulse breakdown and the multi-pulse breakdown are analysed. This split is done to clearly differentiate if the breakdown process occurs in a single cycle or if some kind of charge accumulation is needed in successive cycles in order to form the electron plasma. It will be shown that for the pulse characteristics typically used in the Sat-Com industry, the pulse breakdown is, indeed, a single pulse breakdown. In any case, it is assumed that the pulse shape is rectangular. Hence, during the pulse duration, the field amplitude is constant, modulated by a periodic function of time, e.g., sinus distribution.

Single-Pulse Breakdown

In the case of single pulse excitation, the breakdown condition must be closely related to the pulse duration (τ_p). Of course, the discharge will develop if the electron density growth starts before the pulse finishes. In fact, the single-pulse breakdown level is given by the power (electric field) for which the breakdown condition in (6.6) is satisfied exactly when the pulse finishes, i.e., if $t_B = \tau_p$. This is obvious since for an electric field slightly above this value, the discharge would start to develop before. It is also justified by the fact that, like in the case of CW operation, the discharge is extremely fast.

From (6.6), and requiring that the breakdown occurs exactly at $t_B = \tau_p$, the single pulse breakdown criterion can be written as:

$$\nu\tau_p = \ln\left(\frac{n_B}{n_0}\right). \tag{6.7}$$

From this expression, it is found that the breakdown field is extremely dependent on the pulse duration since the free electron growth (ν) is related to the electric field by a non-linear relationship (see e.g. 5.13).

Fig. 6.1 shows the error introduced in the breakdown onset due to the lack of knowledge about the breakdown condition (6.7) in the logarithm. For very low pulse durations the error becomes large, being extremely difficult to provide a reliable breakdown condition. However, for the typical pulses used by the Sat-Com industry (around 10 μs or higher) the error between considering, for instance, a value of 20 or 40 in the logarithm is below a 2% in the breakdown field. These results have been obtained from a simulation (see end of this chapter) of a rectangular waveguide at 9.5 GHz with a height of 0.3 cm ($\Lambda \approx 0.1\ cm$) at a pressure of 10 torr.

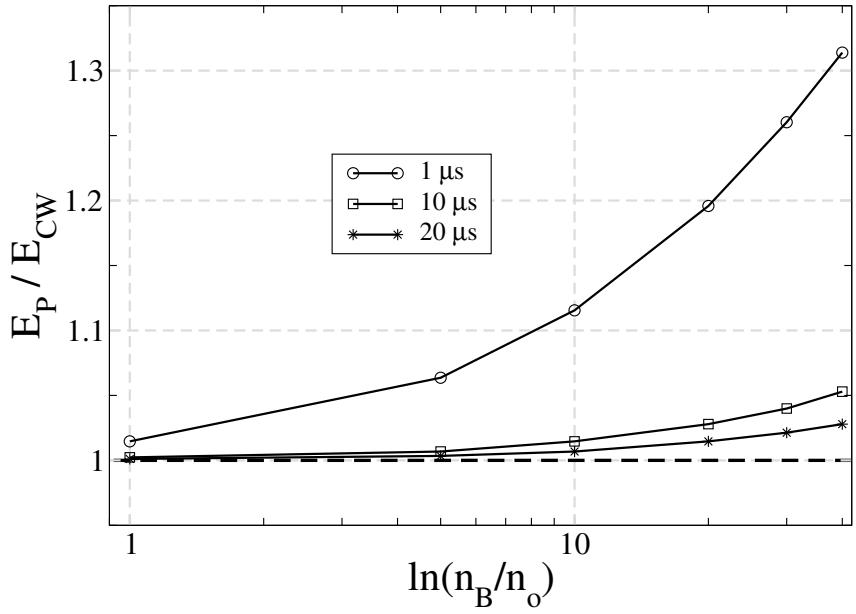

Figure 6.1: *Dependency of the single-pulse breakdown with the breakdown criterion.*

Fig. 6.2 compares the single-pulse breakdown and the CW breakdown electric fields. As expected, the shorter the pulse, the higher the field necessary to ignite the corona discharge. Such a behaviour is usually referred as "pulse hardening" in the literature (see e.g. [116]). Obviously, if $\tau_p \to \infty$, the breakdown criterion is $\nu = 0$, i.e., the CW breakdown result is recovered. It is also interesting to notice that the difference between the CW and the single pulse breakdowns increases as the dimension of the device rises (represented by the characteristic diffusion length in the plot). This can be shown in a very easy way. Assuming that the attachment rate is independent of the electric field (its dependence is much weaker than for the ionisation rate), for the case of CW breakdown is obtained:

$$\nu_i(E_{cw}) = \nu_a + \nu_D,$$

whereas for the case of single pulse excitation, (6.7) can be written as

$$\nu_i(E_{pulse}) - \nu_a - \nu_D = \frac{\ln\left(\frac{n_B}{n_0}\right)}{\tau_p}.$$

Since both ν_a and ν_D are field-independent, the following can be written:

$$\frac{\nu_i(E_{pulse})}{\nu_i(E_{cw})} = \frac{\ln\left(\frac{n_B}{n_0}\right)}{\tau_p \cdot \nu_i(E_{cw})} + 1 \equiv \xi. \tag{6.8}$$

As the dimensions become larger, the losses due to diffusion become smaller, and thus, the electric field required to ignite corona is also lower for both, pulse and CW. This decrease in the breakdown field leads to an increment of ξ, resulting in a higher ratio between the pulse and the CW breakdown fields, as inferred from (6.8).

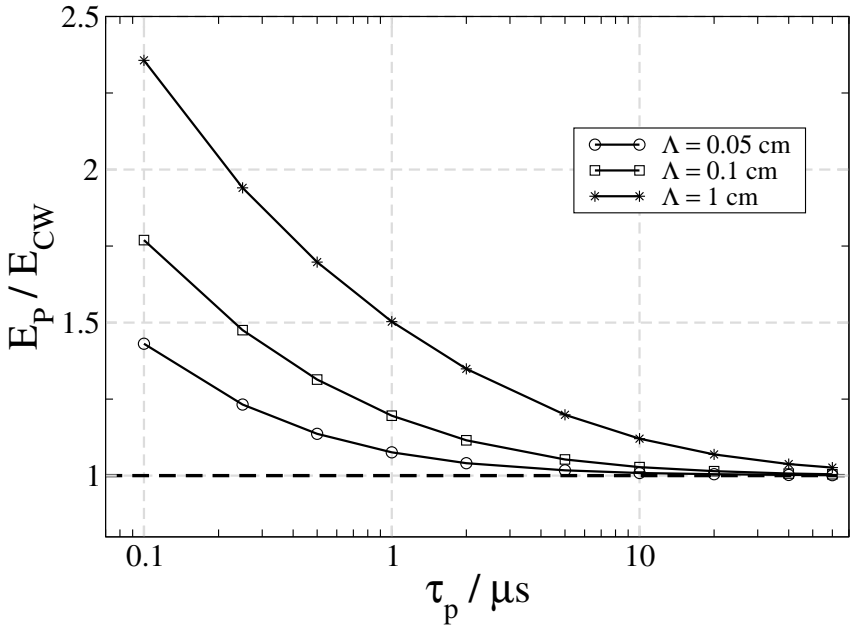

Figure 6.2: *Dependency of the single-pulse breakdown with the pulse duration at a frequency of 9.5 GHz and a pressure of 10 torr.*

Multi-Pulse Breakdown

The breakdown condition for the multi-pulse operation is related to both pulse duration and pulse repetition interval (PRI), i.e., the time between pulses. Evidently, the breakdown onset must increase as the ratio between the pulse duration and the pulse repetition interval decreases since, during the inter-pulse time, no field is applied. The

period ($\overline{T}$) of the multi-pulse signal is the sum of the pulse duration (τ_p) and the pulse repetition interval (T_p):

$$\overline{T} = \tau_p + T_p$$

Since the pulse is rectangular, the amplitude of the root mean square (RMS) field (E_0) is constant during pulses and zero during the inter-pulse time, i.e.:

$$E(t) = \begin{cases} E_0, & k\cdot(\tau_p+T_p) < t < (k+1)\cdot\tau_p + k\cdot T_p \\ 0, & (k+1)\cdot\tau_p + k\cdot T_p < t < (k+1)\cdot(\tau_p+T_p) \end{cases}, k = 0,1,2,... \tag{6.9}$$

where k is the pulse number.

Hence, the growth of the free electron density must follow a similar relationship as a function of time. The electron growth (or decay) rate can be written as [116]:

$$\nu(t) = \begin{cases} \nu_+, & k\cdot(\tau_p+T_p) < t < (k+1)\cdot\tau_p + k\cdot T_p \\ -\nu_-, & (k+1)\cdot\tau_p + k\cdot T_p < t < (k+1)\cdot(\tau_p+T_p) \end{cases},$$

where $\nu_+ > 0$ is the growth of the electron density during the pulse k and ν_-(with $\nu_- > 0$) is the free electron loss during inter-pulse intervals. It has been assumed that the power applied is enough to result in a positive growth of electrons during a pulse duration. This is true if such a power is above the corona CW breakdown power, which is always the case since the pulse breakdown field must be higher than the CW one.

For the multi-pulse case, the breakdown condition is defined by considering that the power necessary to ignite the discharge is lower if the discharge occurs during a pulse duration. In fact, the lowest breakdown level is given by the input power which makes the breakdown to occur exactly at the end of a pulse duration (like in the case of the single pulse breakdown criterion) for the maximum number of cycles k. Mathematically, this maximum is taken as an infinite value for the number of cycles, which is not physically possible but provides the lowest breakdown onset, very close to the real (measurable) threshold [116].

Thus, the breakdown time t_B is taken as $t_B = k\overline{T} + \tau_p$, and, as a consequence, the breakdown criterion in (6.6) for the multi-pulse operation becomes:

$$(k\overline{T} + \tau_p)\nu = \ln\left(\frac{n_B}{n_0}\right), \tag{6.10}$$

and then, using the temporal dependence of the net free electrons production rate, a quite simple result is achieved:

$$k(\nu_+\cdot\tau_p - \nu_-\cdot T_p) + \nu_+\tau_p = \ln\left(\frac{n_B}{n_0}\right). \tag{6.11}$$

As mentioned, the multi-pulse breakdown criterion is mathematically taken considering that the discharge occurs after an infinite number of pulses, i.e., $(k \to \infty)$, and then (6.11) is written as:

$$\nu_+ \cdot \tau_p - \nu_- \cdot T_p = 0, \tag{6.12}$$

which is notably intuitive since, while the pulse is "on", a growth of the electron density takes place but when the pulse is "off", the electron density decreases due to diffusion and attachment processes. Moreover, it is interesting to notice that the breakdown criterion in this case is not dependent on which multiplicity factor is taken as breakdown criterion for the electron growth, i.e., it is independent of n_B/n_0.

It is worthwhile to realize that (6.11) is both the single-pulse and the multi-pulse breakdown criteria. For $k \to 0$, (6.7) is recovered which is the single-pulse breakdown criterion.

An analogous procedure to the one followed for the single-pulse case can be pursued in order to relate the pulse breakdown to the CW one. During the pulse duration, the growth rate is:

$$\nu_+ = \nu_i - \nu_{a2} - \nu_D. \tag{6.13}$$

On the contrary, during the inter-pulse intervals, the losses are mainly due to diffusion and, in a second extent, to three body attachment (in the case of air)

$$\nu_- = \nu_D + \nu_{a3}. \tag{6.14}$$

With this information, the breakdown condition (6.12) can be written as:

$$\frac{\nu_i(E_{pulse})}{\nu_i(E_{cw})} = \left(\frac{T_p}{\tau_p}\right) \cdot \left(\frac{\nu_D + \nu_{a3}}{\nu_i(E_{cw})}\right) + 1, \tag{6.15}$$

and therefore, the same kind of behaviour as in the single-pulse case is observed: the higher the device dimensions, the higher the ratio between multi-pulse and CW breakdown onsets.

At this point, both the single-pulse and the multi-pulse breakdown criteria have been derived. Fig. 6.3 shows the results obtained, making a direct comparison between both breakdown levels. It is seen, as expected, that as the ratio between the PD and the PRI decreases, the multi-pulse breakdown level becomes increasingly larger than the single-pulse one. In fact, the only situation in which the multi-pulse breakdown onset is below the single-pulse one is for $\tau_p = 1\mu s$ and $\tau_p/T_p = 0.1$ or higher. Both conditions are hardly fulfilled in common pulse sources used by the Sat-Com industry. A typical set of pulse characteristics would be a pulse duration around 10 μs and a pulse repetition interval around one millisecond.

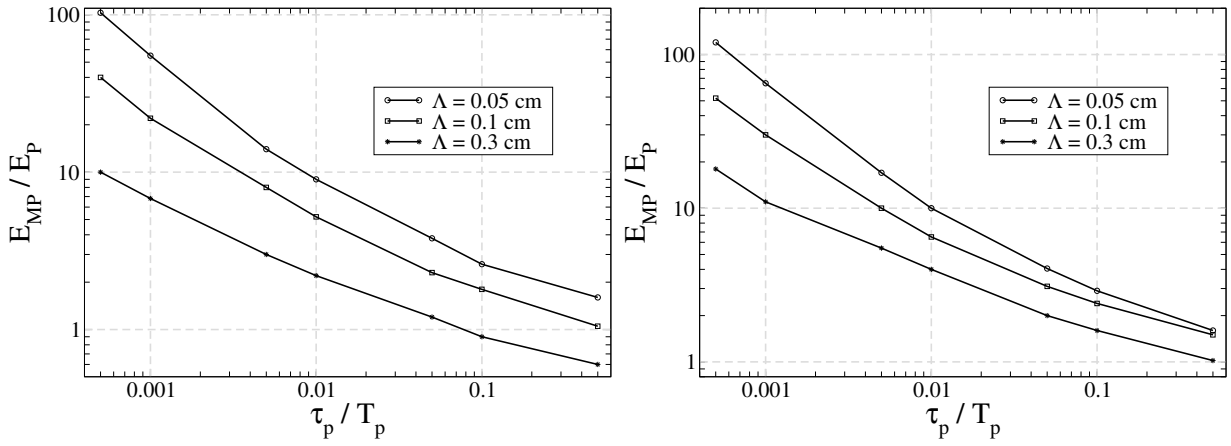

(a) $\tau_p = 1\mu s$ (b) $\tau_p = 10\mu s$

Figure 6.3: *Multi-pulse - Single-pulse ratio.*

6.2 Breakdown computation

In this section, the corona discharge equation is solved using the breakdown criteria above derived. Such a solution provides the breakdown level of a particular device. Two ways are followed to solve the corona equation. First, a simple analytical approach is used. This approach has the advantage of providing the very worst case (lowest possible breakdown) very efficiently. Moreover, it is, in principle, accurate if specific conditions are fulfilled within the device. Secondly, a full numerical computation based on a Finite Differences scheme is developed. This full numerical approach results in a more accurate breakdown level since the complete field distribution inside the component is being considered. The results presented in the next chapter fully validate the procedure developed.

6.2.1 Parallel plates approximation

Many common situations present in microwave components can be simulated following a parallel plate approximation. This approximation assumes that one of the dimensions of the device is much smaller than the rest and, therefore, the electric field can be approximated by its component in the direction of this dimension. In rectangular waveguides, the fundamental mode only has electromagnetic field component in the y-direction. It is therefore in this axis where the parallel plate configuration can take place assuming that the device operates in the fundamental mode. Besides, the y-component has a sinus distribution along the x-axis. However, the parallel plate approximation holds when this field can be taken as constant within a large region of the device. This approach has shown its validity in the analysis of the multipactor discharge [117] for the cases where a particular element of the microwave structure presents a very low height and a very high electric field.

As already shown in the previous chapter, taking (5.5) and assuming that the height of the device is much smaller than the width and the length, it is found that

$$-(\pi/b)^2 + \frac{(\nu_i - \nu_a)}{D} = 0, \tag{6.16}$$

where b is the separation between the parallel plates, in this case, the reduced waveguide height.

If the height is of the order of the waveguide width, another bounded dimension must be considered, and then, the breakdown condition reads:

$$-(\pi/b)^2 - (\pi/a)^2 + \frac{(\nu_i - \nu_a)}{D} = 0, \tag{6.17}$$

a being the waveguide width.

In the case of complex geometries, this approximation is still accurate if in some region of the device the electric field density is high and constant in a relatively large region (no waveguide discontinuities are close to this zone). This will be explicitly shown in the numerical computations of the next chapter for the case of a bandpass filter.

In this work, we have taken the maximum field inside each device element and, assuming a parallel plate configuration, the breakdown threshold for each of these elements has been determined using (6.17). This procedure has three main advantages:

1. It provides a rough idea of both the location of the discharge in the whole device and the critical pressure.

2. It allows the microwave designer to check very quickly if the corona response of the device is within the margins required since the result obtained is a very worst case. Once a breakdown close to the margin is obtained, the full numerical analysis can be performed.

3. It can be used to speed up the numerical calculation. The main problem when searching the corona breakdown power is that one does not know with which power to start. If the first attempted power is very far from the breakdown power onset, many iterations are needed in order to reach the breakdown threshold with the desired precision. Since the analytical approach is very fast and provides the worst case, one can be sure that the final breakdown onset obtained from the numerical calculation is always higher. Therefore, when looking for the breakdown power, this fact can be used for speeding up the power sweep, and hence, the final computational time.

6.2.2 Numerical computation

The solution to (5.10) when the electromagnetic field is highly inhomogeneous - like in complex microwave components - must be obtained numerically. Several methods can be employed to do this. Among them, Finite Elements (FE) and Finite Differences (FD) are the most commonly used. The main advantage of Finite Elements over Finite Differences is the possibility of using complex meshes in order to study arbitrary shape volumes. On the other hand, in the case of simple geometries, FD becomes more appropriate due to its simplicity and power. Since the geometries for which the theory is going to be applied are rectangular, a Finite Differences scheme has been chosen because a meshing procedure based on rectilinear coordinates is perfect for this numerical technique.

A FD scheme rewrites the equations to be solved in terms of the unknown variable and its derivatives in each point using a cubic-like mesh.

Each first space derivative can be discretized as:

$$\left.\frac{dn}{dx}\right|_{x=x_i} \approx \frac{n(x_{i+1}) - n(x_{i-1})}{x_{i+1} - x_{i-1}}, \tag{6.18}$$

and the second derivative is just:

$$\left.\frac{d^2n}{dx^2}\right|_{x=x_i} \approx \frac{\frac{n(x_{i+1})-n(x_i)}{x_{i+1}-x_i} - \frac{n(x_i)-n(x_{i-1})}{x_i-x_{i-1}}}{\frac{x_{i+1}-x_{i-1}}{2}} \tag{6.19}$$

Therefore, the 3D electron density equation (5.10) can be expressed as:

$$\begin{aligned} &\frac{\frac{n(x_{i+1})-n(x_i)}{x_{i+1}-x_i} - \frac{n(x_i)-n(x_{i-1})}{x_i-x_{i-1}}}{\frac{x_{i+1}-x_{i-1}}{2}} + \frac{\frac{n(y_{i+1})-n(y_i)}{y_{i+1}-y_i} - \frac{n(y_i)-n(y_{i-1})}{y_i-y_{i-1}}}{\frac{y_{i+1}-y_{i-1}}{2}} + \\ &\frac{\frac{n(z_{i+1})-n(z_i)}{z_{i+1}-z_i} - \frac{n(z_i)-n(z_{i-1})}{z_i-z_{i-1}}}{\frac{z_{i+1}-z_{i-1}}{2}} + \frac{\nu_i(x_i,y_i,z_i) - \nu_a(x_i,y_i,z_i)}{D} \cdot n(x_i,y_i,z_i) - A = 0 \end{aligned} \tag{6.20}$$

In this equation, A is related to the corona discharge condition. In the case of CW, $A = 0$, whereas in the case of pulse, $A = \frac{\ln\left(\frac{n_B}{n_0}\right)}{\tau_p}$ (the single-pulse case is considered).

In a particular point of the mesh, the electron density can be obtained in terms of the ionisation and attachment rates in that point and the free electron density in the surrounding points of the grid, just rearranging the corresponding terms in (6.20).

Additionally, to solve this equation, boundary conditions must be given. Since the component walls are perfectly metallic, the free electron density on the walls surface is zero, i.e.:

$$n(S) = 0, \tag{6.21}$$

where S is the metallic surface of the device.

However, the device is open in the direction of propagation. Therefore, a boundary condition is still needed for those borders where no metallic walls exist (port planes), i.e., in the planes defined by $z = 0$ and $z = z_f$ (with z_f equal to the device length). At the port planes, the electric field excited is much lower than in many regions inside the device. Hence, for a particular input power slightly above the breakdown, a considerably small field is expected in these planes. Initially (before the application of the signal), the device possesses a certain (unknown) electron density distribution which can be assumed constant. It is therefore expected that, when the electric field is applied, the electron density tends to zero in the regions of low field. Thus, it has been assumed that, in the ports, the same boundary condition holds as in the metallic walls, i.e.,

$$n(z = 0) = 0, \qquad n(z = z_f) = 0. \tag{6.22}$$

Such a boundary condition is of secondary importance since the breakdown occurs far from the port planes. In fact, during the validation of the numerical computation, it was checked that the final result did not change if a different boundary condition for the port planes was used.

Once the boundary conditions have been imposed, the corona breakdown equation can be solved. For such a purpose, several numerical techniques can be used [118]. In this work, an iterative method (red-black Gauss-Siedel algorithm) has been employed for several reasons:

- Lack of knowledge of the real electron density in the device before the application of the field.
- No high precision is required in the computation of n. It is only necessary to know whether, for a particular input power, the free electron density grows or not.
- The solution is continuously computed, which speeds up the process.
- Easiness of implementation without taking resort to external software packages.

An iterative method basically consists in taking a guess solution of the equation in each particular mesh point and iterate until the real solution with the desired precision is reached. Since what we want to know is the variation of the free electron density due to the application of a particular input power, the background electron density (n_0) has been also employed as the guess solution for the complete structure (in each mesh point). In particular, we have taken the background (guess solution) equal to 1. Physically, this means that before applying the signal, a background electron density of $1e/cm^3$ was present in the device. The electromagnetic field distribution within the component results, in turn, in a space distribution of the free electron density. Apart from the electric field distribution itself, such a distribution also depends on the device geometry, which

determines the diffusion losses. In this way, for an input power well below the onset level, the free electron density falls below its background value since the loss of electrons is more important than the gain by ionisation. On the contrary, for input powers well above the threshold, the electron density grows within almost the whole device. For input powers slightly over the threshold, there are zones in the device where the electron density is larger than the background density and zones where the electron density is low due to high losses. The former are those which provide the maximum power that the device can handle without developing a corona arc. This is shown in the next chapter in order to locate the exact place within the component where the discharge occurs, which is also of interest from the engineer point of view.

The important issue is that we are not interested in the real electron density inside the device, but in the breakdown onset. Therefore, our interest is knowing if, for a particular applied field, the electron density increases sufficiently or if, on the contrary, it decreases below the guess solution. Indeed, if we apply a breakdown condition such as (6.4), the corona equation becomes not solvable for electric fields different to the breakdown. However, the residuals (difference in each point of the exact solution of the equation and the numerical one) behave like the time dependent part, i.e., as if they would represent the time evolution of the free electron density. Thus, it is observed that the residuals grow exponentially above breakdown, whereas they tend to drive the free electron density to zero for values below breakdown. This is extremely important from the numerical point of view because it allows to find the breakdown level without solving a time dependent equation which is, surely, much more computational time consuming.

6.2.3 Corner singularities

One of the toughest aspects when computing the electromagnetic fields within microwave devices is the handling of metallic corners. Wedges become an important issue due to the non-singular character of the field close to them. This problem affects any numerical approach used in order to solve the problem. In this way, in discretization methods like Finite Elements or Finite Differences, a very dense mesh is needed near the edges, what even does not ensure the quality of the result. On the other hand, in a full-wave approach, the number of modes required for modelling the discontinuity becomes extremely high and, again, very close to the corner, the correct electromagnetic field value can not be determined. In fact, for solving the field close to these regions, analytical considerations must be followed [119–121].

Since the electron density growth is directly related to the electric field, it is more than likely that it will not be properly determined near the edges. Therefore, there exists a critical danger of determining a wrong breakdown onset due to this corner effect.

Nevertheless, apart from the field itself, the free electron density also depends on other

parameters such as frequency and pressure. As mentioned, in Sat-Com applications the relevant range of pressures is approximately between 100 and 3000 Pa (location of the critical pressure). For these pressures, the main loss mechanism is diffusion since, for low pressures, the diffusion region is large and electrons can freely move to low field regions to, finally, be absorbed at the walls. Therefore, if the diffusion region is large, the electric field must be high enough in a large zone (of the order of the diffusion region) in order to free more electrons than are lost. If the electric field were very high in a small region, the electrons would rapidly diffuse to the low field zones preventing the formation of the electron plasma.

The consequence of this is clear: a very local field enhancement (edge effect) does not cause the corona discharge if, in the surrounding space, the electric field is not sufficiently high. This is extremely important since it allows applying numerical methods without taking special care of the wedges singularities. On the contrary, for high pressures, the diffusion region is reduced and attachment is the main loss mechanism. In this situation, the impact of the corners in the onset determination is critical. Fortunately, this high pressure range is of no interest in Sat-Com applications.

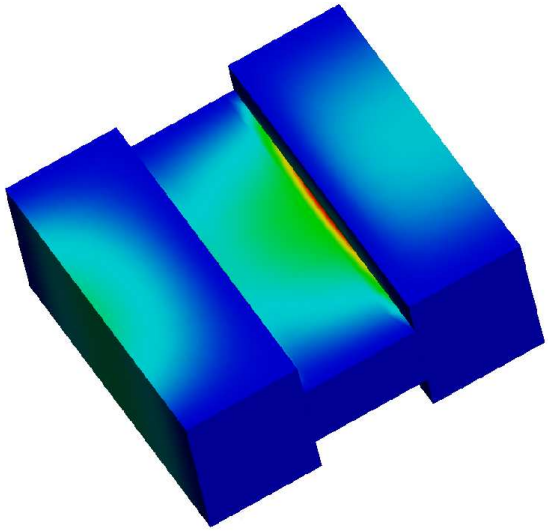

(a) *Electric field in the structure at 9.4 GHz*

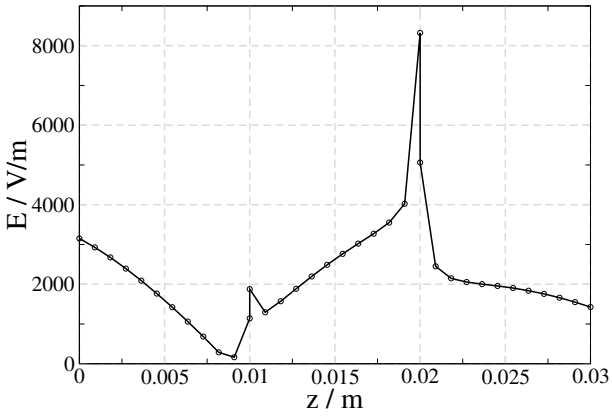

(b) *Electric field at the centre of the structure along the z-axis at 9.4 GHz.*

Figure 6.4: *Geometry and electromagnetic response of the example chosen.*

This physical qualitative behaviour must be quantitatively confirmed in order to ensure that, for the pressures of interest, the corner effects are negligible. Jordan et al. [116] have shown by means of an analytic approach that, indeed, metallic edges are not a problem in the the determination of the breakdown onset. Fig. 6.4 shows an easy structure

that has been chosen to check the effects of the corner singularities. In this case, we have just considered a 3 element structure where the inner element has a reduced height. The ports (outer waveguides) are standard WR 75 waveguides (a = 19.05 mm, b = 9.525 mm) whereas the inner gap has a reduced height of 6.23 mm and the same width. The singularities can be clearly seen in Fig. 6.4(b) where the electric field at the centre of the device (x = 0) is plotted along the z axis. The two peaks correspond to the two discontinuities. Indeed, such peaks indicate that the electric field is not being properly calculated because, otherwise, a smoother transition should occur.

Fig. 6.5 shows the computation of the free electron density for an input power equal to the breakdown power. Two cuts in the structure are presented. One is in the y-z plane, cutting the structure at the centre of the x-axis. The second one is the x-y plane cutting the structure at the point z where the maximum of the electron density is reached. The plots are from top to bottom for 500, 2000, 5000 and 20000 Pa. The lighter the zone (the more yellow), the higher the electron density. The effect above mentioned can be clearly observed. At low pressures, the width of the profile is quite broad. However, as the pressure raises, the distribution becomes more and more local and, finally, it can be observed that the discharge indeed occurs close to the edges. In such cases, the electron density distribution is not properly calculated. Fortunately, as already mentioned, such a pressure range is of secondary interest in Sat-Com applications.

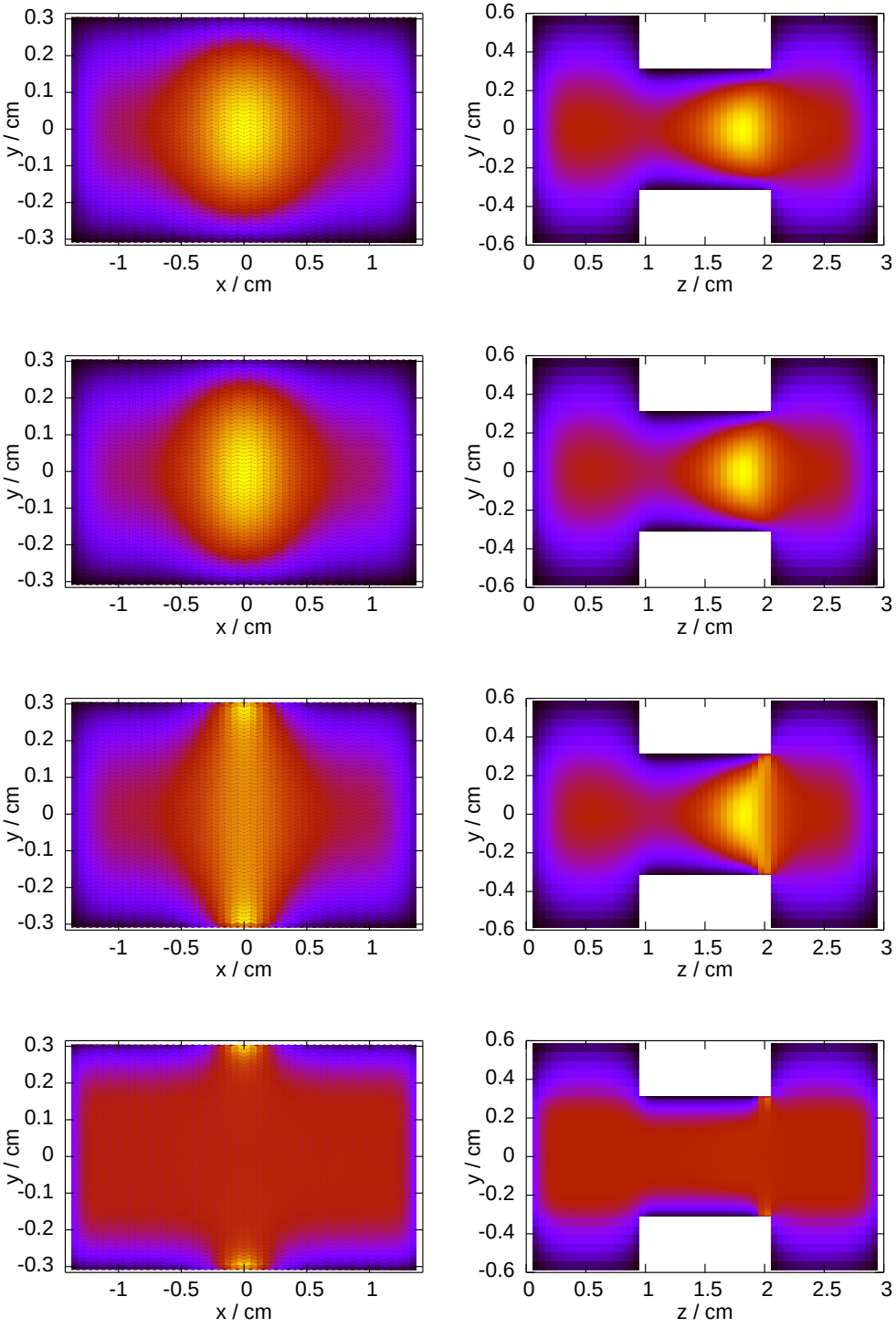

Figure 6.5: *Computed electron density for the structure of Fig. 6.4. The plots are for 500, 2000, 5000 and 20000 Pa (from top to bottom).*

Chapter 7

Corona Results

In this chapter, results in the corona discharge threshold obtained for particular test components are presented. Experimental data together with the theoretical results are shown. Additionally, plots of the free electron density for different input powers above the breakdown onset are also displayed in order to locate where the discharge takes place, i.e., the region in the whole device more prone to develop a corona discharge. Some other calculations for each sample are shown in appendix E. In that appendix, the structures are drawn together with the electric field in the whole device. Furthermore, the scattering parameters are presented and, even more important, the electric field along the z-axis at the centre of the waveguide is also displayed. This last graph provides a great amount of information at a first glance, since the high field regions are quickly recognised.

It is shown along the chapter that an accuracy always better than 0.3 dB is reached, when comparing the simulation results to experimental measurements, for the breakdown power at the critical pressure. This degree of precision obtained is unique for a model/code intended to predict the corona onset [122], allowing for a confident design of free corona microwave devices for Sat-Com applications.

It is necessary to remark that it is not easy to find corona breakdown measured data for complex devices in the existent literature because such components are normally flight models. Thus, a corona discharge is not developed in these structures in order to prevent any sort of damage to the hardware. Moreover, these devices and their testing are commonly out of the possibilities of research institutions like universities and, normally, only Sat-Com industries do deal with them. Thanks to a research project (ESA/ESTEC Contract No. 16827/02/NL/EC), corona breakdown data has been acquired for different structures. Samples operating at different frequency ranges have been used in order to assure that the predictability of the model presented does not fail for different frequency bands. In particular, measurement results in the range from 7.4 GHz to 12.5 GHz have been employed for the validation. The measured data exposed have been obtained either from Tesat-Spacecom GmbH & Co. KG laboratories or from an internal (not published) ESA report [123].

The components analysed have been tested using nitrogen or air as the gas filling the vacuum chamber and, therefore, the samples themselves. Besides, a single CW power source has been employed.

7.1 H-Band transformer gap operating at 7.4 GHz

A transformer gap filter operating in H-Band (WR-112, a = 28.5 mm , b = 12.62 mm) has been used for checking the validity of the model developed in the previous chapters. It has been tested at 7.4 GHz and in the presence of nitrogen. In Fig. E.1, the component is displayed showing that it is a 4-transformer (5 steps) structure. Fig. 7.1 shows the measured breakdown onset (courtesy of Tesat-Spacecom GmbH & Co. KG) together with the simulations performed.

As mentioned in the previous chapter, the analytical results are obtained assuming that the maximum electric field for each particular element within the structure (this component consists of 11 elements) is the electric field in the whole element. Of course, this is the worst case and results, as a consequence, in the lowest possible breakdown level. However, the Sat-Com industry uses such kind of approximations in order to have a rough idea of the breakdown level. The lack of consistency of such an approach can be quickly recognised: the highest electric fields normally occur close to the corners, and it has been demonstrated that such fields do not generate a discharge if the field is not high enough around that zone. Therefore, it is even difficult to define (and compute) a maximum electric field which could be used for the calculation of the corona onset. Consequently, the only reliable option is to employ a full numerical analysis in order to consider the complete electromagnetic field distribution in the particular component.

The error bars of the numerical computation in Fig. 7.1 are related to the parameters of the particular gas. It has been assumed that the phenomenological expressions for the ionisation and the attachment rates have an error of 10% [25]. Such errors have their origin in the fact that these parameters have been measured for the DC case, and not under RF conditions.

Fig. 7.2 shows the free electron density within this structure for two different input powers which result in a corona discharge. It is plotted in the y-z plane taken at the centre of the x-axis. It is found that at power levels well above the breakdown (P = 256 W), the electron density is high in many regions within the device. This means that the input power is so high that the conditions for the development of a corona discharge are fulfilled in many zones in the component. This is a general behaviour for any component fed with an input power well above its corona onset, and can result in the destruction of the device if the power source is not switched off immediately. However, as the input power decreases, the black regions (very low electron density) start to appear everywhere except

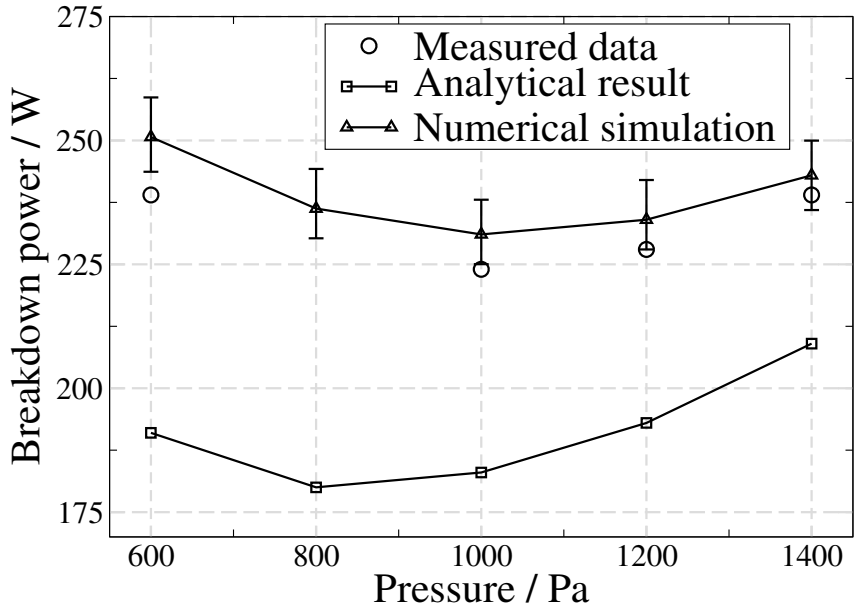

Figure 7.1: *Corona discharge threshold of the structure in Fig. E.1 at a frequency of 7.4 GHz.*

in the corona discharge zone with the lowest breakdown threshold (Fig. 7.2(b)).

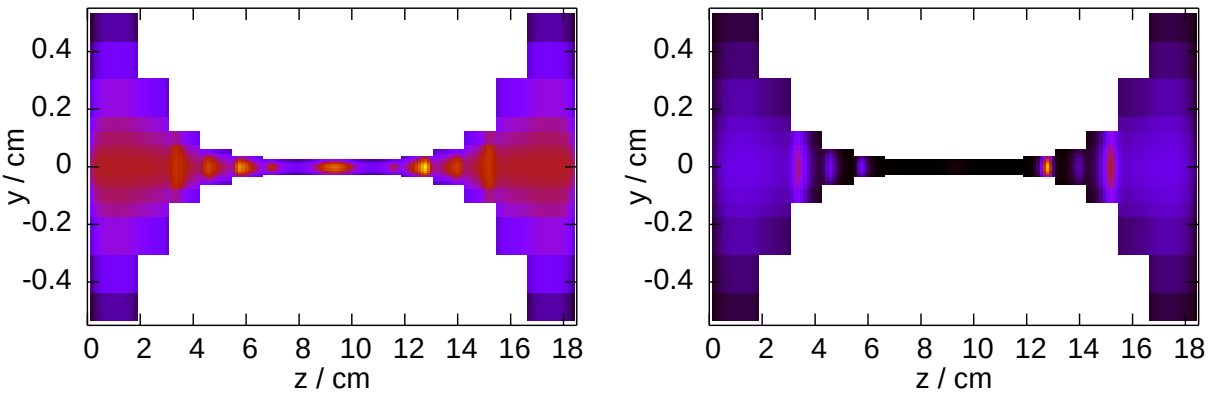

(a) Electron density at 256.2 W.

(b) Electron density at 233 W.

Figure 7.2: *Electron density for different input powers above the breakdown at the critical pressure for the structure in Fig. E.1.*

It is important to realise that the discharge does not occur in the highest field region (inner gap as shown in Fig. E.1(d)) as would be expected. However, this is easily understandable if diffusion losses of electrons are considered in the different regions of the component. As shown in chapter 5, the loss of free electrons due to diffusion is extremely

dependent on the size of the device zone which encloses the high field region (the larger the region, the lower the diffusion losses). Thus, although the electric field is not maximum in the corona discharge region, the diffusion losses are lower than in the inner gap (due to its small height).

It is also found that the discharge region is not symmetric as would be foreseen due to the geometrical symmetry of the device. This is related to the fact that the frequency used for the analysis is not the exact centre frequency of the device and, as a consequence, the electric field distribution is not symmetric either. In fact, the discharge is predicted to occur in the region far from the power source (z = 0). Experimentally, it can not be generally known where the discharge takes place because the detection methods are extremely fast, avoiding, this way, any possible damage to the hardware equipment.

In any case, it is likely that the discharge does not take place where the numerical computation predicts because the difference in the breakdown levels between one place of the device and its symmetric point (symmetric respect to the direction of propagation z) is rather small. As a consequence, if an input power slightly above the breakdown level were used, the zones close to the power source would partially reflect the input signal. Eventually, the full power does not "reach" the further region and, hence, the discharge would not occur there. On the other hand, this reflection increases the electric field between the power source and the reflecting region which finally results in the discharge in that zone.

7.2 X-Band transformer gap operating at 9.5 GHz

A transformer gap in X-Band (WR-90, a = 22.86 mm , b = 10.16 mm) has also been tested for corona in the presence of nitrogen. The sample is shown in photograph E.2(a). Experimental data together with the theoretical prediction is shown in Fig. 7.3. It is seen that, again, the agreement between both is notable.

In this occasion, it is found that the analytical results are around 3 dB below the measured data. Therefore, it is once more verified the need of a full numerical simulation in order to predict the component breakdown onset with a reasonable precision.

As in the case of the component analysed in the previous section, the free electron density is plotted (Fig. 7.4) for two different input powers above the breakdown level. It is found that the corona effect also occurs near a step between two transformers and not in the inner gap where the electric field is maximum (as shown in Fig. E.2(d)). This seems to be a general behaviour of transformer gap components due to the reduced height of the centre element.

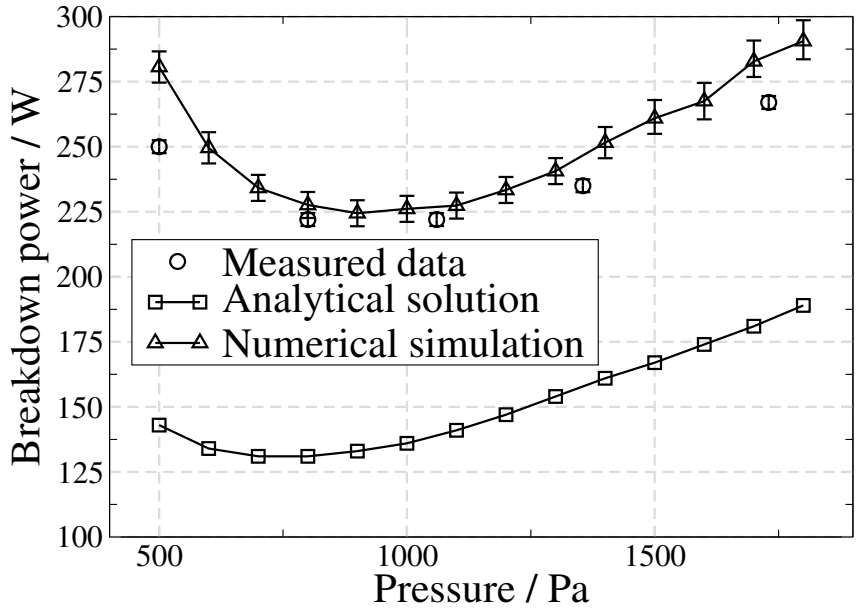

Figure 7.3: *Corona discharge threshold for the structure in photograph E.2(a) at a frequency of 9.5 GHz.*

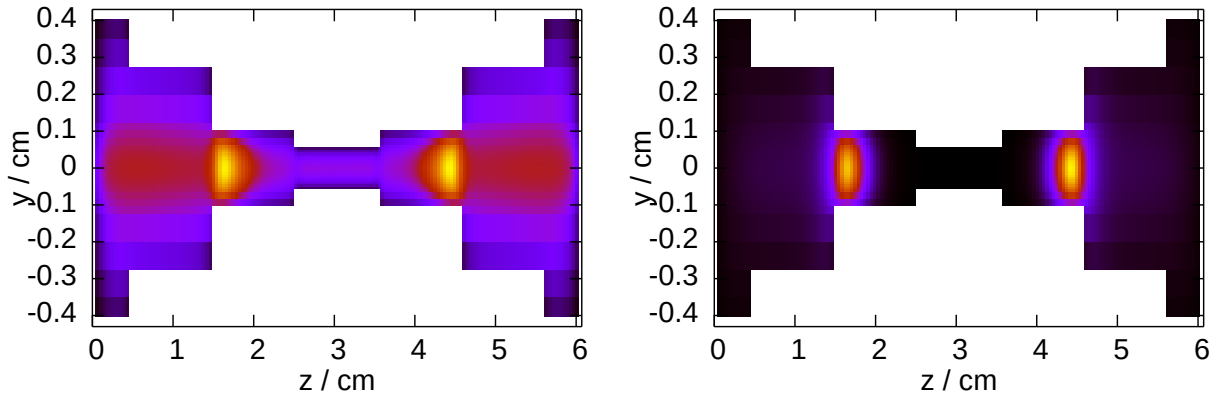

(a) *Electron density at 255 W.*

(b) *Electron density at 226 W.*

Figure 7.4: *Electron density for different input powers above the breakdown at 10 mBar (1000 Pa) for the structure in photograph E.2(a).*

7.3 X-Band bandpass filter operating at 9.5 GHz

Measurements have been carried out for the sample shown in photograph E.3(a). This component is a bandpass filter with a rather small bandwidth of around 100 MHz (see Fig. E.3(c)). Nitrogen has been used for testing this device as well. The experimental data obtained and the theoretical prediction is shown in Fig. 7.5. Once again, the agreement

is significant.

For this component, the electron density is plotted in Fig. 7.6 for two different input powers at 1000 Pa. It is noticed that the corona effect occurs within the second cavity where the electric field is maximum (as shown in Fig. E.3(d)). This is understood if it is taken into consideration the fact that the device has a constant height (except in the ports) and, therefore, the diffusion losses are similar in all the cavities and irises of the device.

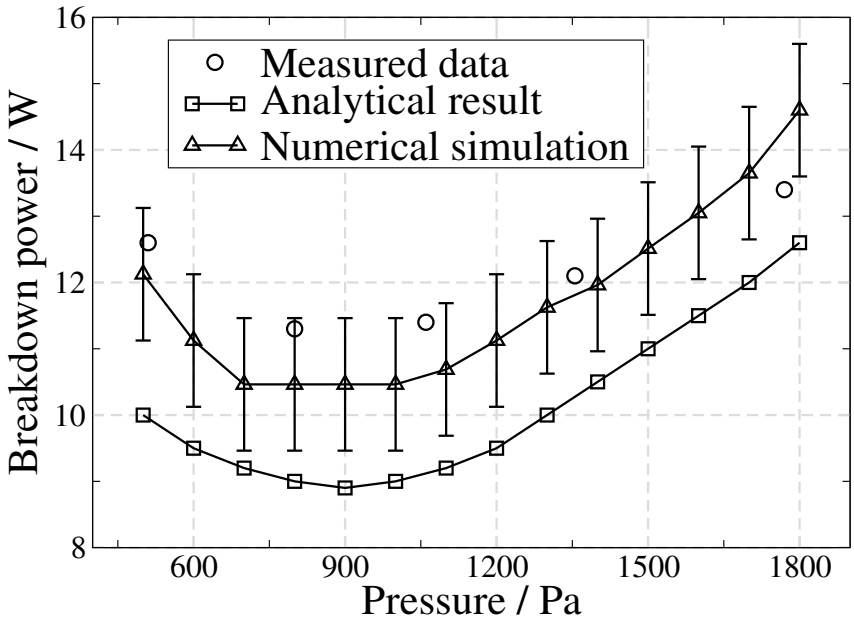

Figure 7.5: *Corona discharge threshold for the structure in Fig. E.3 at a frequency of 9.5 GHz.*

It is also found that, in this case, the analytical and the numerical results do not differ considerably. This can be explained by two facts:

- The discharge occurs within one of the cavities and not near a transition. This results in a relatively good analytical computation because the influence of the rest of the device is minimised.

- Though the error made is only 1 or 2 W, the electric field is so high (see Fig. E.3) that such an error is much larger in terms of electric field, which is what, indeed, controls the discharge.

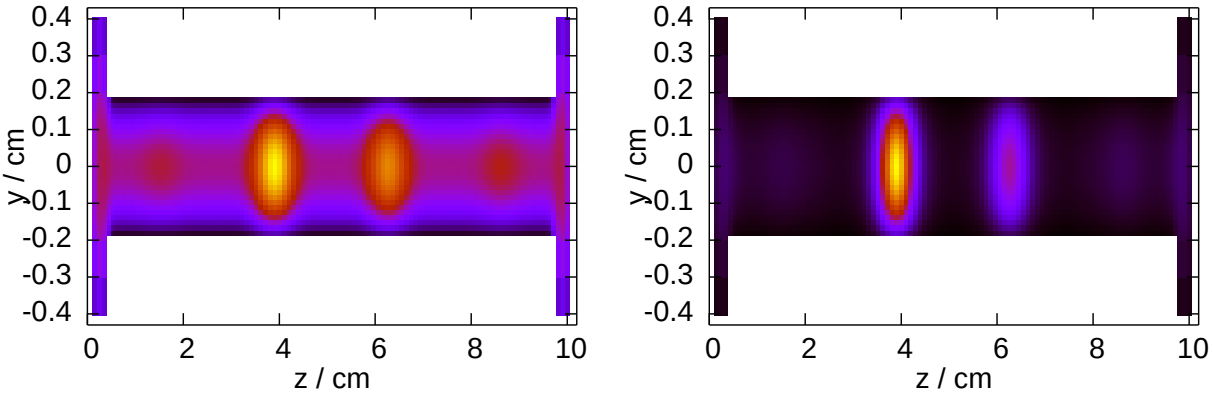

(a) *Electron density at 12.6 W.*

(b) *Electron density at 10.8 W.*

Figure 7.6: *Electron density for different input powers above the breakdown at 1000 Pa for the structure in Fig. E.3.*

7.4 X-Band lowpass filter operating at 9.5 GHz

The component shown in Fig E.4(a) has been also tested for corona in the presence of nitrogen. In this case, it is a corrugated lowpass filter (see Fig. E.4(b)). The measured data and the theoretical results are displayed in Fig. 7.7. Again, the agreement between both is noticeable, fully validating the model developed. Besides, it is seen that the analytical result is rather poor (around 3 dB disagreement) showing, once more, that the full numerical analysis is necessary for the accurate prediction of the breakdown onset.

The free electron density is shown in Fig. 7.8. It is seen that the corona discharge occurs in the inner gap where the electric field is maximum (as shown in Fig. E.4(c)). This happens because, in this component, the inner gap (2.17 mm height) is not much smaller than the other elements whereas the field is, in fact, much higher.

7.5 Ku-Band lowpass filter operating at 12.2 GHz

A test sample (courtesy of Tesat-Spacecom GmbH & Co. KG) operating at Ku band (WR75, a = 19.05 mm , b = 9.525 mm) has also been used for the validation of the model. In this case, it is a corrugated lowpass filter where both the width and the height of the component vary along the structure. The geometry is shown in Fig. E.5. The sample has been tested in the presence of air. Once again, it is found that the agreement is remarkable (approx. 0.25 dB of discrepancy for the critical pressure).

Fig. 7.10 shows the free electron density distribution in this component for different

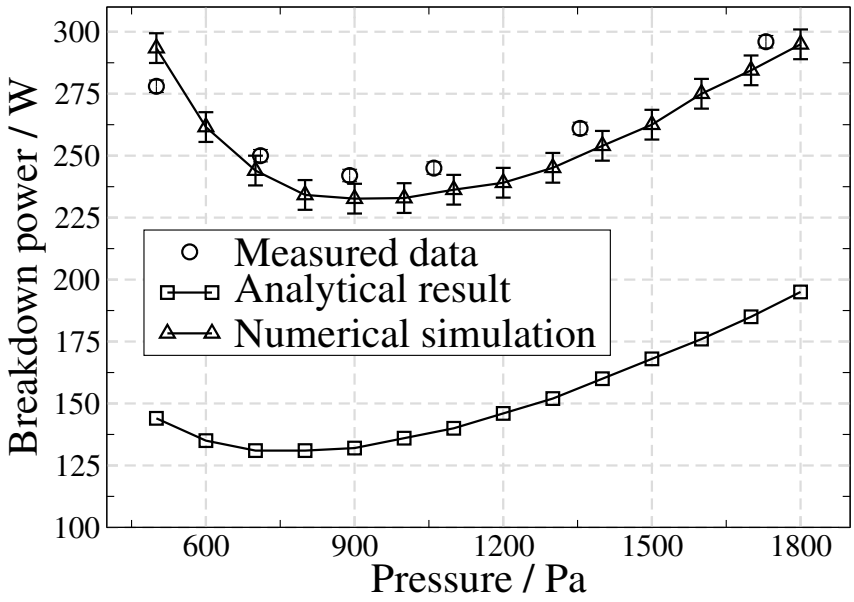

Figure 7.7: *Corona discharge threshold for the structure in Fig. E.4 at a frequency of 9.5 GHz.*

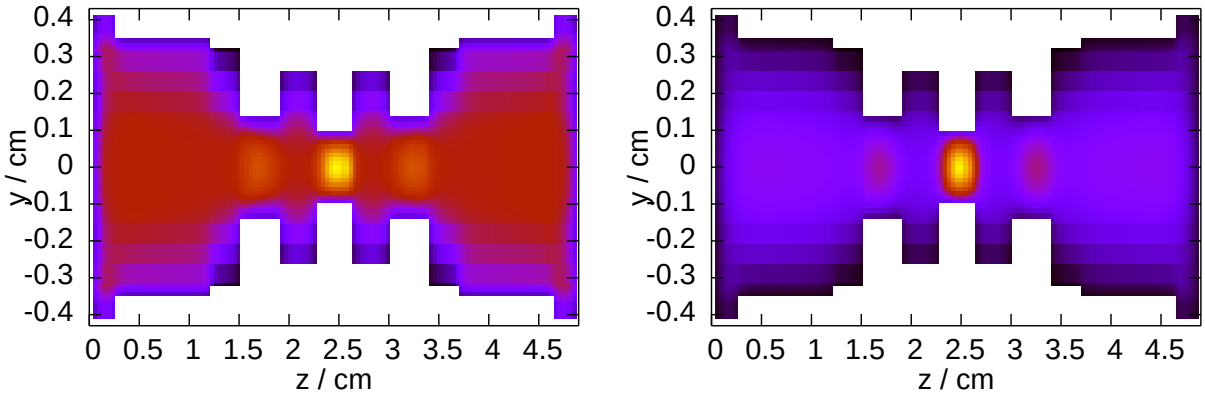

(a) *Electron density at 250 W.*

(b) *Electron density at 236 W.*

Figure 7.8: *Electron density for different input powers above the breakdown at 1000 Pa for the structure in Fig. E.4.*

input powers above the breakdown at 15 mBar (1500 Pa). The location of the discharge is clearly displayed. For this device, the discharge also occurs in the region of highest electric field as seen by comparison with Fig. E.5(c). Such a figure explains why this happens: the difference in the electric field amplitude between the small and the large regions is extremely high which results in the development of the discharge in the small regions in spite of the diffusion losses.

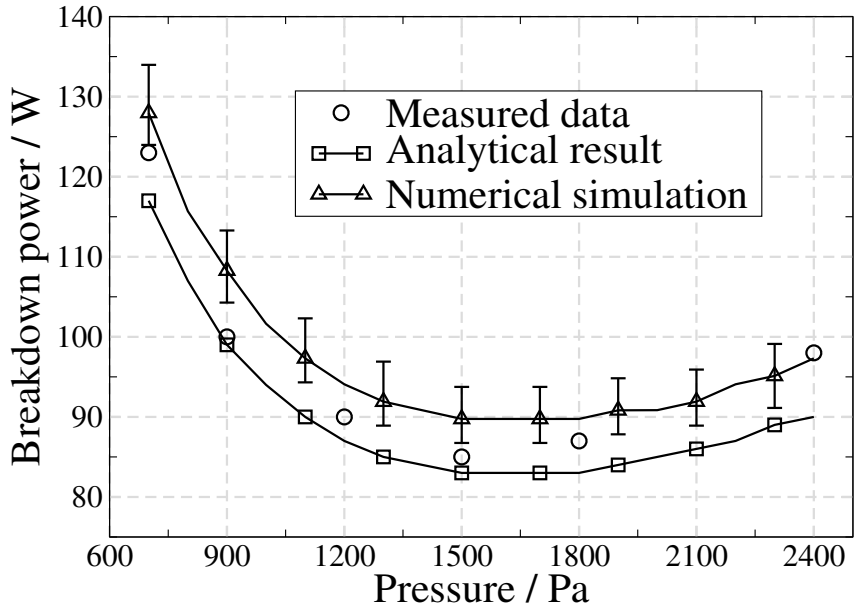

Figure 7.9: *Corona discharge threshold for the structure in Fig. E.5 (Courtesy of Tesat-Spacecom GmbH & Co. KG.).*

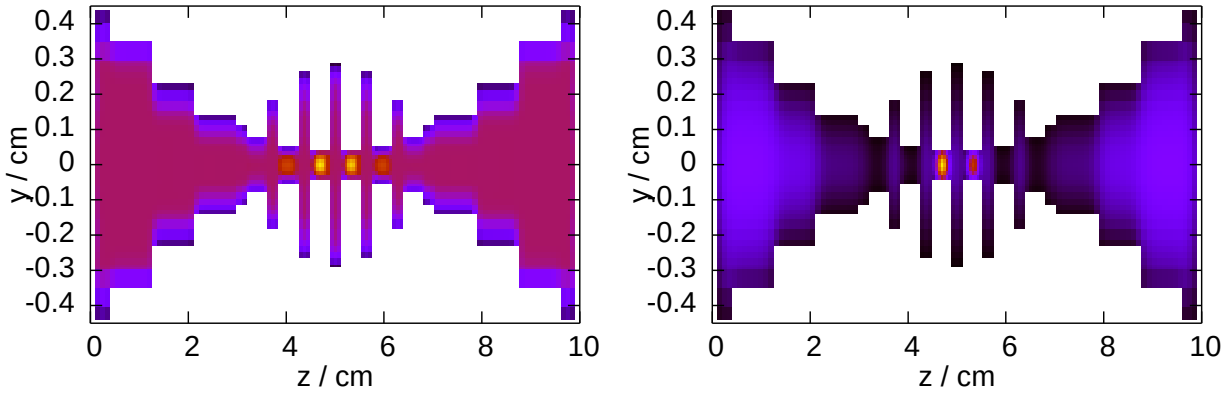

(a) Electron density at 105 W.

(b) Electron density at 90 W.

Figure 7.10: *Electron density for different input powers above the breakdown at 1500 Pa for the structure in Fig. E.5.*

7.6 Ku-Band lowpass filter operating at 12.5 GHz

A corona simulation for the structure shown in Fig E.6 has been performed. In this case, the structure has also been tested in the presence of air for a frequency of 12.5 GHz. Again, we can observe (Fig. 7.11) that the numerical result is in good agreement with the experimental data (for the critical pressure (approx. 1500 Pa) the error is around 0.2 dB).

In this case, the measured data is above the simulation results. Apart from the intrinsic error caused by the measurement itself (which is also shown by using the error bars), an explanation to this is related to the fact that a radioactive source within the vacuum chamber located close to the DUT is necessary in order to achieve reproducibility of the measured data [124]. In fact, if such a radioactive source is not used, the measured data do not follow the Paschen curve, and the breakdown level is a bit higher than in the case in which the radioactive source is used. The data presented in previous sections have been taken at Tesat-Spacecom GmbH & Co. KG facilities using a radioactive source. However, the measured data of the device presented in this section were extracted from the ESA report, which does not explicitly state the use of an electron source.

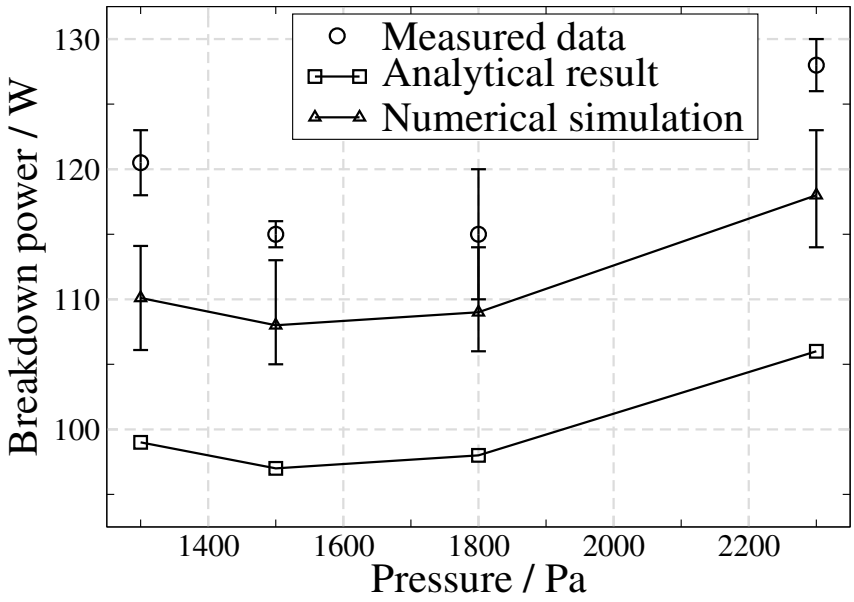

Figure 7.11: *Corona discharge threshold for the structure in Fig. E.6 at a frequency of 12.5 GHz.*

In Fig. 7.12 the free electron density at 1500 Pa within the component is displayed. By inspection of Fig. E.6(c), it can be easily recognised that the discharge occurs in the highest field region, like in the case of the Ku-Band lowpass filter of section 7.5.

7.7 Summary

Several conclusions can be extracted in relation to the corona discharge data (both theoretical and experimental) presented in this chapter:

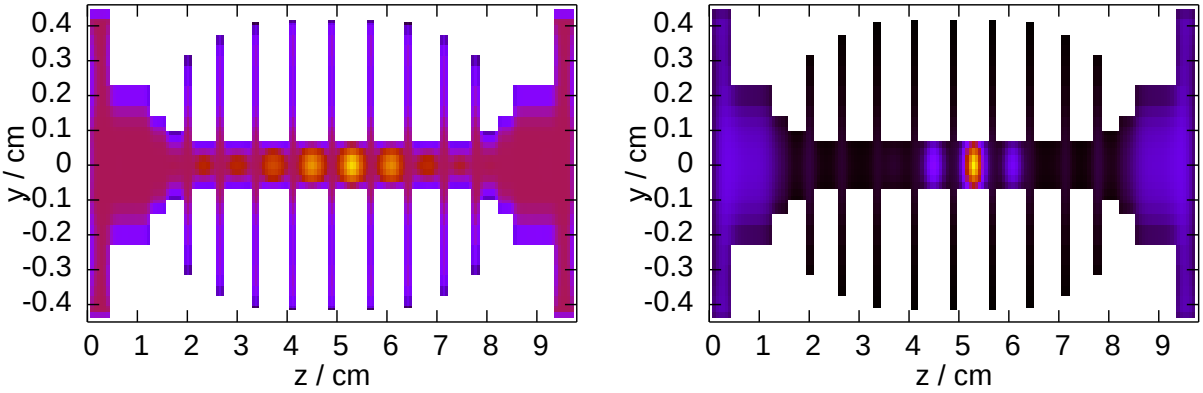

(a) *Electron density at 137 W.*

(b) *Electron density at 110 W.*

Figure 7.12: *Electron density for different input powers above the breakdown at 1500 Pa for the structure in Fig. E.6.*

Breakdown level

- Both for nitrogen and air a remarkable agreement between the measured data and the simulation is achieved using a full numerical approach.

- The error introduced using the analytical approach depends on the particular component. In devices where the discharge occurs far from the discontinuities, the analytical result becomes quite reliable (e.g. bandpass). However, in devices where the discharge tends to develop near steps between waveguide elements (e.g. transformer gaps), or where the element enclosing the high field region is short in the direction of propagation (e.g. corrugated filters), such an approach is quite poor.

Location of the discharge

- In transformer gap structures, the discharge tends to occur in the transformers and not in the inner gap due to the high diffusion losses in small regions.

- In corrugated lowpass and bandpass filters, the discharge tends to happen in the high field region since the dimensions of these zones are usually large. This is specially true in the case of bandpass filters because the height of the device is commonly kept constant along the propagation direction (inductive filter).

- For symmetrical structures, the asymmetry in the location of the discharge (if it occurs) is due to the fact that the operating frequency is not the centre frequency of the structure. If this asymmetry leads to a discharge location further from the source port, it is to be foreseen that, experimentally, this behaviour will not be observed because of the power reflection along the device. A real example of the

location of the corona arc is shown in Fig. E.7. It is seen that the arc occurred close to the input port (indeed in the sixth element of the whole structure) and, then, it propagated towards the power source. This can be catastrophic since the test bed equipment can be damaged due to the high temperatures reached.

Chapter 8

Conclusions & Outlook

The incessant increase in the number of carriers, as well as their power levels, leads to a considerable risk of RF breakdown and intermodulation interference in communications satellites. The occurrence of these phenomena can severely degrade the functionality of a satellite, rendering it useless for communication applications. Therefore, it is important to assess such a risk in order to minimise it during the satellite lifetime.

In this thesis, Passive Intermodulation at rectangular waveguide flanges and Corona Discharge in complex filters based on rectangular waveguide technology have been investigated. The following sections summarise the results achieved and propose further development in these research areas.

8.1 Conclusions

In the case of Passive Intermodulation, a model for the computation of the intermodulation level as a function of different system parameters has been developed. Such calculation has been based on assuming that the PIM level for a particular set of system parameters is known. Such an approach does not allow to predict the absolute intermodulation level but to investigate the impact of different parameters on it. This helps to understand the PIM phenomenon in metallic contacts and to assess the importance of each system parameter. This knowledge can be useful in order to design waveguide flanges presenting low intermodulation levels.

Apart from the theoretical investigation, experimental research in real waveguide connections has been performed. It has been found, as expected, that silver-plated connections present lower PIM levels than aluminium junctions. Besides, it has been shown that, in the case of metals like aluminium, it is of critical importance to connect the waveguides with high pressure. However, for relatively clean surfaces, like silver-plated, the importance of high pressures is secondary. In these cases, it is more important to have the contact pressure shared on the whole contact surface. The use of gaskets has allowed to assess the impact of several coating metals on the PIM response. It has been shown that a very soft material like indium helps to reduce the PIM level in the case of

aluminium waveguides. However, it is not helpful in the case of silver-plate connections. This suggests that the cleanliness of the surfaces is more important than the softness of the contacting material. In the case of aluminium contacts, the intermodulation level as a function of the combined power has been also investigated. It is clear that deviations from the N dB/dB rule are more important in those cases where junctions are not properly tightened. For the well-tightened cases, deviations are reduced and the rule is almost perfectly followed. This clearly manifests that the oxide layers on the aluminium surfaces are not broken and, therefore, the local increase of the temperature in the contact zones has a negligible effect.

The intermodulation level as a function of the power ratio has been studied as well. No deviations from the theoretical behaviour have been observed, which confirms the hypothesis that high order intermodulation products do not affect the lower ones in real-life applications. This is important in order to ensure that higher intermodulation orders falling in the reception band do not need to be measured, reducing, this way, the costs associated to a complete PIM test campaign. Moreover, if higher order contributions are negligible, the Taylor expansion up to the intermodulation order required can be used in order to simulate the PIM response of the system.

In the second part of this thesis, a full analysis of the Corona Discharge problem in rectangular waveguide based devices has been carried out. The physical processes underlying behind such a phenomenon and relevant to Sat-Com applications have been described. Moreover, these mechanisms have been quantitatively considered, allowing for a detailed analysis of the discharge process. By means of the calculation of the electron density in the case of equilibrium, the breakdown onset has been numerically computed. Two results have been presented: an analytical one based on the maximum field in the device, which consequently results in the worst case possible, and a numerical result based on a Finite Differences approach which considers the full electromagnetic field distribution within the component. It has been checked that, in many occasions, the analytical calculation results in an extremely low breakdown onset. This is even more important if it is considered that such kind of approximations are currently employed by the Sat-Com industry in order to design space hardware. Additionally, it has been verified that metallic corners are not a critical issue in the determination of the breakdown threshold for the pressures of interest. However, they become critical if higher pressures are considered. The location of the Corona Discharge within the whole device has been also determined for different structures. It has been shown that in some cases the discharge does not occur in the regions of highest electric field as would be expected.

An accuracy always better than 0.3 dB when comparing the simulation (numerical) results to experimental measurements is reached for the breakdown power at the critical pressure. Such a precision is extremely difficult to achieve and, as far as Sat-Com applications are concerned, it is an outstanding outcome if it is taken into consideration that, at least, a margin of 3 dB between tested breakdown onset and operation power level must be provided. Even more critical, up to now, a minimum margin of 6 dB between simulation and specifications has been normally required. Hence, the results obtained in

the framework of this thesis help to reduce such a margin allowing the high-power space engineer to design free-corona hardware in a faster and more confidently way. This finally results in a reduction of the costs associated to hardware design for space applications.

8.2 Outlook

The line of work initiated in this thesis may be continued with the investigation of several topics related to PIM at waveguide connections. First of all, different materials from those analysed in this work can be investigated. In particular, metals with low contact resistance are likely to present low intermodulation levels. Different waveguide connections to the ones used in this work must be also investigated, both in terms of bolts configuration (location and number) and operation at different frequency bands. This last point is particularly important since higher frequency ranges are more prone to suffer intermodulation due to the sensitivity of the signals to small system irregularities. Apart from this, PIM tests are commonly carried out using two carriers only (sometimes three carriers are employed). However, no theoretical prediction is used in order to confirm that the worst case is being analysed. In fact, as shown in [125], depending on the number of signals, their frequency separation and the intermodulation order to be analysed, the PIM level for the multicarrier case can be above the two carrier configuration. Therefore, it is also necessary to experimentally investigate the intermodulation level response when using several carriers in order to assess the impact of the carrier frequency and amplitude distributions in the intermodulation level.

Regarding Corona Discharge, a large amount of research areas are still open and deserve a further attention from the scientific community. In particular, following a similar approach to the one developed here, the corona breakdown onset of different types of structures can be determined. Among them, probably the most interesting are microwave devices based on ridge or double-ridge rectangular waveguides, cylindrical or elliptical waveguides, and coaxial transmission lines. Moreover, the prediction of the Corona Discharge threshold in the case of complex filters with tuning screws is a tough task which has to be carried out in the next years. Electrical breakdown in filters partially filled with dielectric materials is also interesting for the Sat-Com industry. Dielectrics in microwave filters are commonly employed because they allow for a higher miniaturisation. No prediction of the corona phenomenon in this kind of subsystems has been performed until now.

Finally, the interest in the prediction of the corona threshold in re-entry vehicles is growing up due to several space missions which intention is to provide information about the physical properties of planetary objects in the solar system (e.g. Mars or Titan). For such cases, knowledge of the atmosphere properties of these space bodies is necessary in order to assess the risk of development of a Corona Discharge in the final stages of a space mission.

Acknowledgements

In the following, I would like to express my gratitude to all the organisations which have helped me to carry out this PhD thesis:

- **European Commission:** Financing in the frame of the project "Millimetre-wave and microwave components design framework for ground and space multimedia network", contract number RTN1-1999-00105.
- **European Space Agency (ESA/ESTEC):** Financing in the frame of the projects:
  - "Multipactor and Corona Discharge: Prediction, simulation and design in microwave components", Contract No. 18827/02/NL/EC
  - "Surface Treatment and Coating for the Reduction of Multipactor and Passive Intermodulation (PIM) Effects in RF Components",
    Contract No. 17025/03/NL/EC.
- **Tesat-Spacecom GmbH & Co. KG:** to provide many of the experimental data presented in this thesis and to provide the facilities in order to perform the PIM measurements.

List of Symbols

a	waveguide width
b	waveguide height
B	magnetic flux
B_T	bolt head/washer radius
d	distance between the flat surface and the asperities height mean
D_i	modified diffusion coefficient per coordinate
e	electron charge
e^-	electron
E	electric field
E_{eff}	effective electric field
E_{rms}	root mean square electric field
E_i	Young's modulus
$E^{'}$	equivalent Young's modulus
f	frequency
H	magnetic field
H	hardness of the softest material in contact
l	interference distance
$\overline{l}$	interference distance average
l_c	critical interference distance
L_T	thinckness of the bolted plates
m	electron mass
M	molecule
n	free electron density
n_0	background free electron density
n_B	breakdown free electron density
N	gas density
P	electron production rate
p	pressure
p^*	effective pressure
r	asperity radius
R_a	average roughness
t	time
t_B	breakdown time

T	temperature
T_p	pulse repetition interval
$\overline{T}$	period
$\overrightarrow{v}$	velocity of the gas
z_f	device length

α	effective field divided by p
α_i	ionisation coefficient
β	roughness parameter
β_r	recombination rate
γ	effective ionisation rate
η	microasperity density
$\hbar$	reduced Planck constant
μ_i	electron mobility
ν	net ionisation rate
ν_c	electron-neutral collision rate
ν_i	ionisation rate
ν_a	attachment rate
ν_{a2}	two-body attachment rate
ν_{a3}	three-body attachment rate
ϕ^*	Gaussian distribution of microasperities height
σ	standard deviation of the surface heights
σ_s	standard deviation of the asperity heights
τ_p	pulse duration
ω	angular frequency
Λ	diffusion length

List of Acronyms

AC	Alternate Current
BeCu	Beryllium-Copper
DC	Direct Current
DUT	Device Under Test
ESA	European Space Agency
ESTEC	European Space Research and Technology Centre
FD	Finite Differences
FDTD	Finite Differences in Time Domain
FE	Finite Elements
FEM	Finite Elements Method
FEST	Full-wave Electromagnetic Software Tool
IM	InterModulation
MIM	Metal-Insulator-Metal
PD	Pulse Duration
PIM	Passive InterModulation
PRI	Pulse Repetition Interval
RF	RadioFrequency

Appendix A

Contact Impedance calculation

The total impedance of the circuit of Fig. 2.7 provides the voltage drop in the junction as shown in (3.18). The total impedance is the parallel sum of the non-contact capacitor impedance and the sum in serie of the envelope constriction resistance and the sum in parallel of the contact capacitor impedance and the constriction resistance.

The impedance of the upper branch of the circuit is

$$Z_1 = R_C + \frac{Z_c \cdot R_{const}}{Z_c + R_{const}} = R_C + \frac{|Z_c|^2 \cdot R_{const}}{|Z_c|^2 + R_{const}^2} + \frac{Z_c \cdot R_{const}^2}{|Z_c|^2 + R_{const}^2} \equiv Re\{Z_1\} + Im\{Z_1\} \qquad (A.1)$$

where: $Re\{Z_1\} = R_C + \frac{|Z_c|^2 \cdot R_{const}}{|Z_c|^2 + R_{const}^2}$, $\qquad Im\{Z_1\} = \frac{Z_c \cdot R_{const}^2}{|Z_c|^2 + R_{const}^2}$.

The total impedance results in

$$Z = \frac{Z_{n-c} \cdot Z_1}{Z_{n-c} + Z_1} = \frac{(Re\{Z_1\} + Im\{Z_1\}) \cdot Z_{n-c}}{Re\{Z_1\} + Im\{Z_1\} + Z_{n-c}}. \qquad (A.2)$$

And, finally, the modulus of the impedance becomes

$$|Z| = \frac{\left(|re\{Z\}|^2 + |im\{Z\}|^2\right)^{1/2}}{|re\{Z_1\}|^2 + |im\{Z_1\} + Z_{n-c}|^2}, \qquad (A.3)$$

where:

$re\{Z\} = Re\{Z_1\} \cdot |Z_{n-c}|^2$,

$im\{Z\} = Im\{Z_1\} \cdot |Z_{n-c}|^2 + |Im\{Z_1\}|^2 \cdot Z_{n-c} + |Re\{Z_1\}|^2 \cdot Z_{n-c}$.

Appendix B

PIM samples

The samples are presented in this appendix. The full-length waveguides can be seen in photograph B.1 where also the two waveguide flanges are shown: the flange under test (six hole configuration) and the interface flange to the test set-up (eight hole configuration). Photograph B.2 shows the two kind of gaskets used during the test campaign. And finally, in Fig. B.3 the dimensions of the flanges and gaskets are presented.

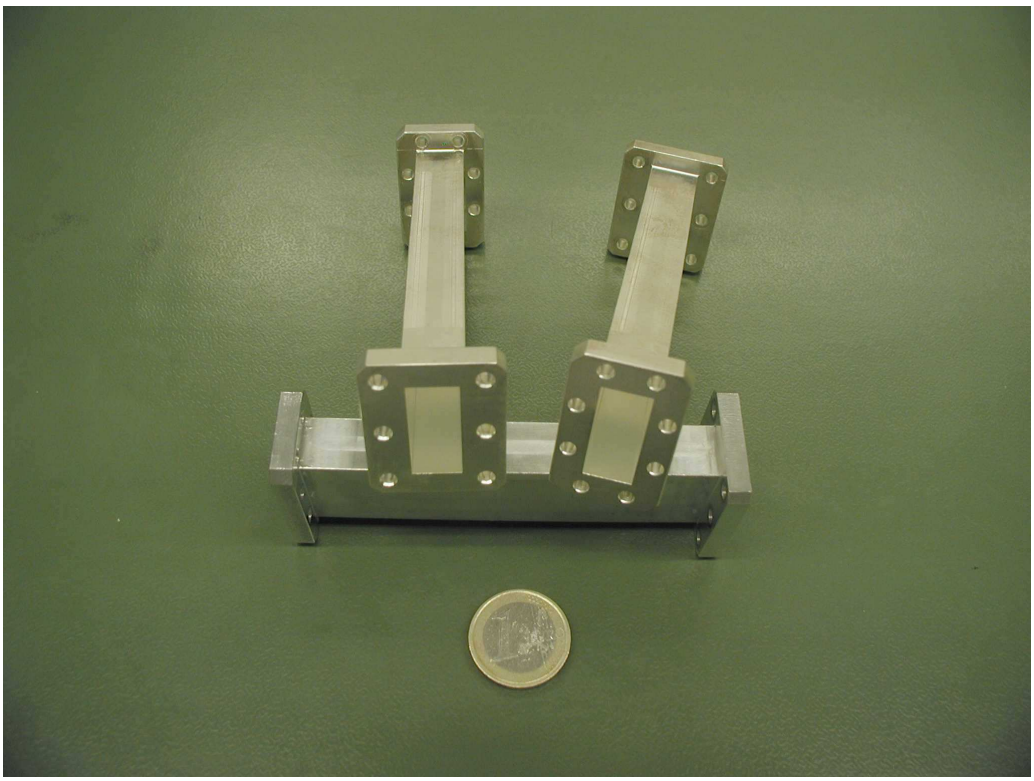

Figure B.1: *Waveguides used. The flange under test (6 holes) and the interface flange (8 holes) with the test set-up are shown.*

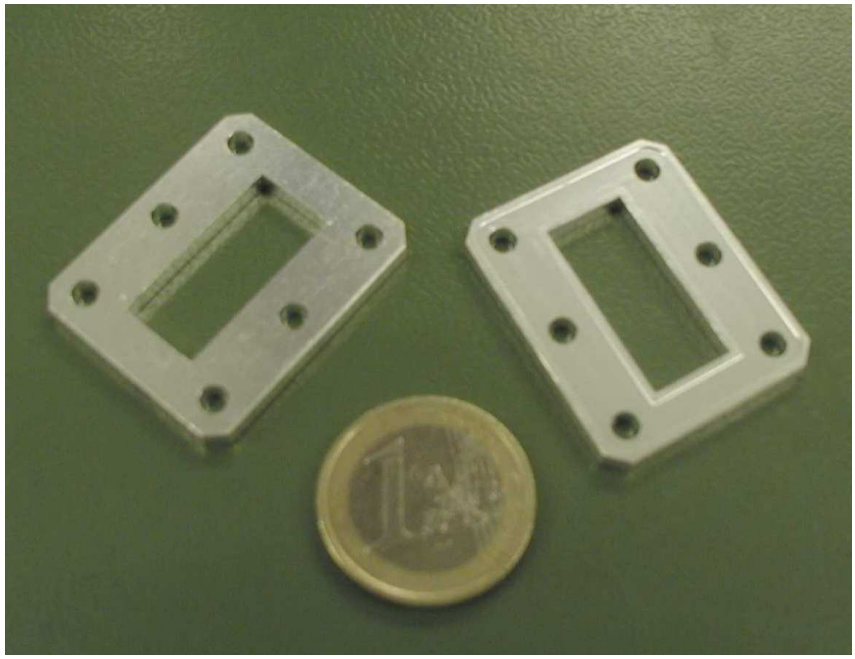

Figure B.2: *Gaskets employed; on the left a flat gasket, on the right a bridged gasket.*

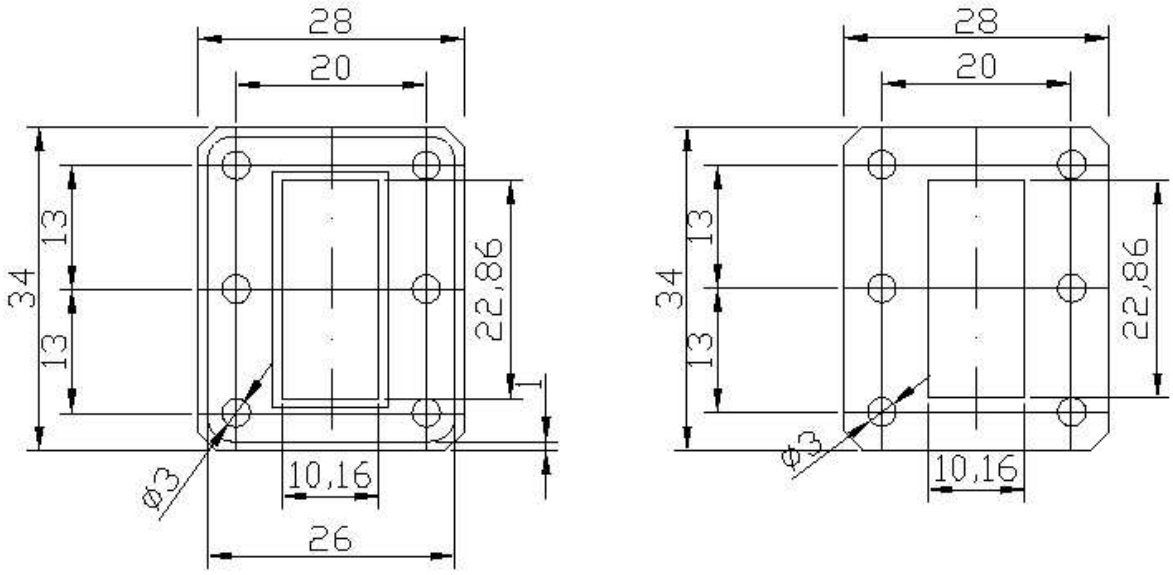

Figure B.3: *Dimensions of the flanges (and gaskets) used.*

Appendix C

PIM Test set-up

The following photographs show the test set-up used for the PIM measurements. Basically, one needs two sinthesizers and two amplifiers are needed in order to reach high power levels in the input. For combining the input carriers a low-PIM diplexer is used. After the DUT, an output diplexer is used to separate the PIM frequency (which is amplified and finally goes to the spectrum analyser) from the input signals (which are driven to a low-PIM load).

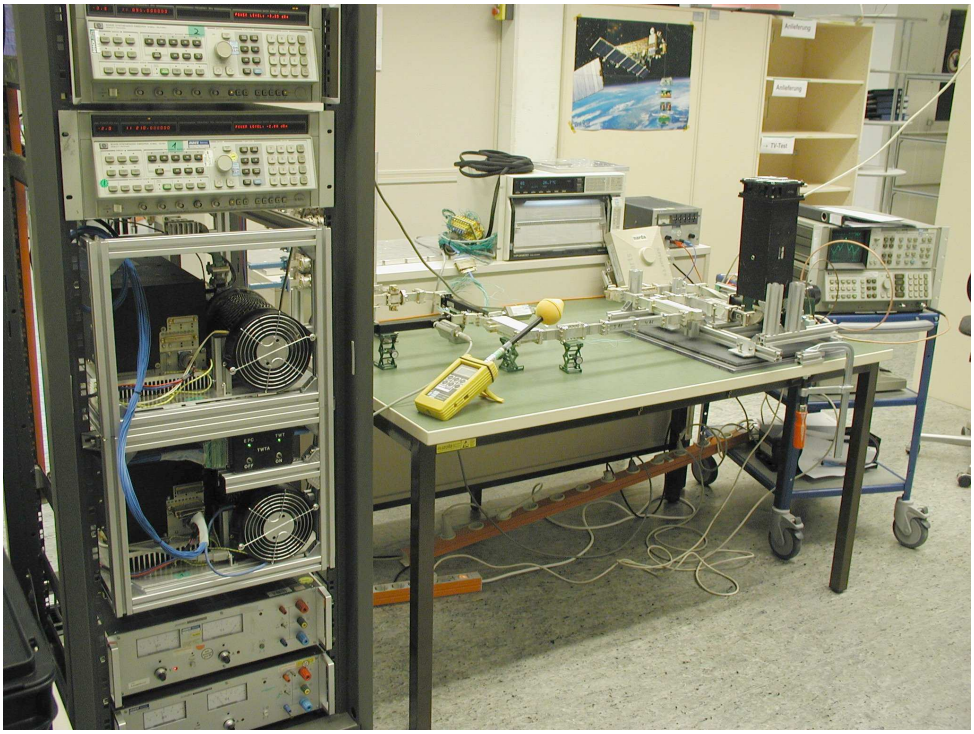

Figure C.1: *Complete PIM test set-up.*

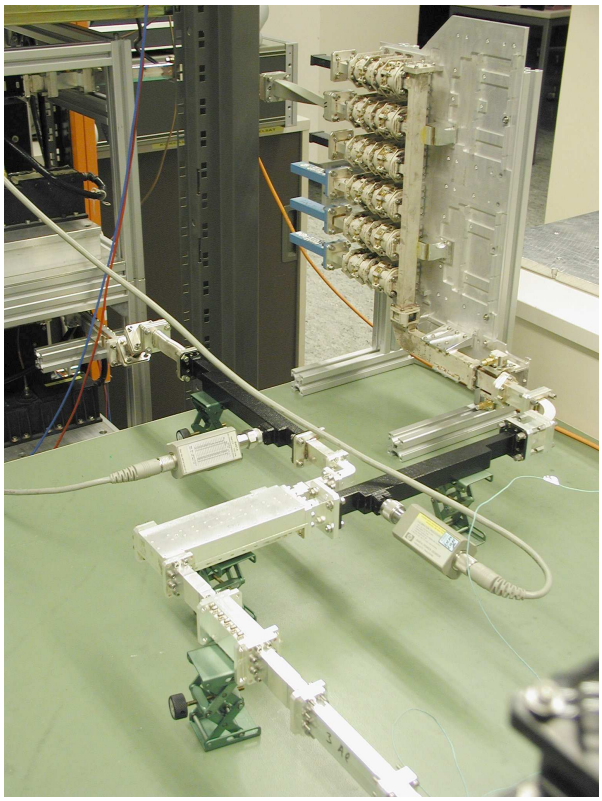

Figure C.2: *Test set-up input.*

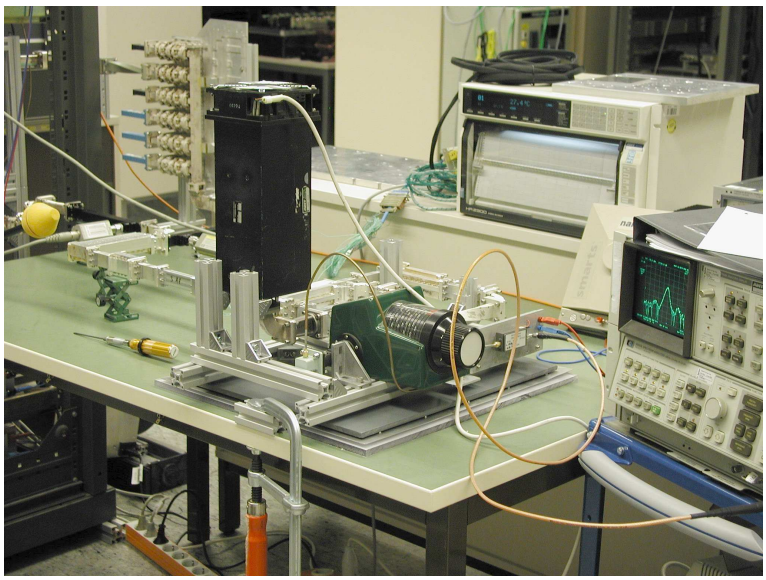

Figure C.3: *Test set-up output.*

Appendix D

PIM results for special coatings

In this appendix, the experimental results obtained when using special gaskets are presented for the following cases:

- Aluminium waveguides
  - Hard gold gaskets
  - Beryllium-Copper gaskets gaskets
  - Indium gaskets
  - Seal sheets for the contact evaluation
- Silver-plated aluminium waveguides
  - Hard gold gaskets
  - Beryllium-Copper gaskets gaskets
  - Indium gaskets

D.1 Aluminium waveguides

D.1.1 Hard gold gaskets

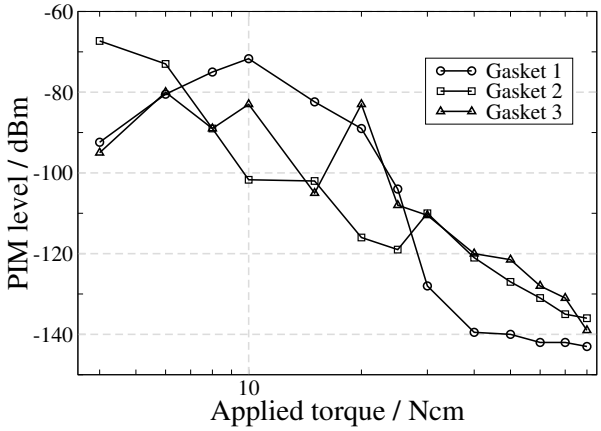

(a) *PIM level versus applied torque when one flat gasket is inserted.*

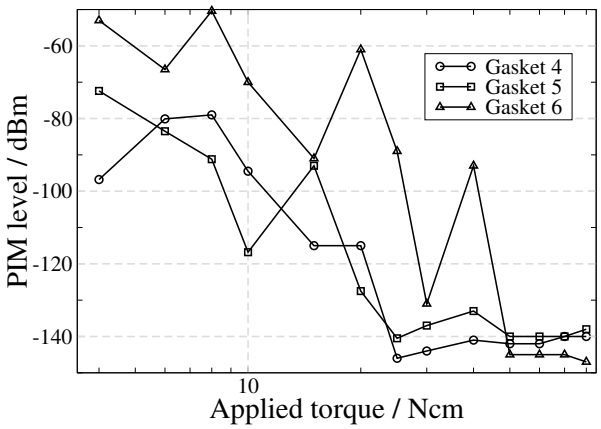

(b) *PIM level versus applied torque when one bridged gasket is inserted.*

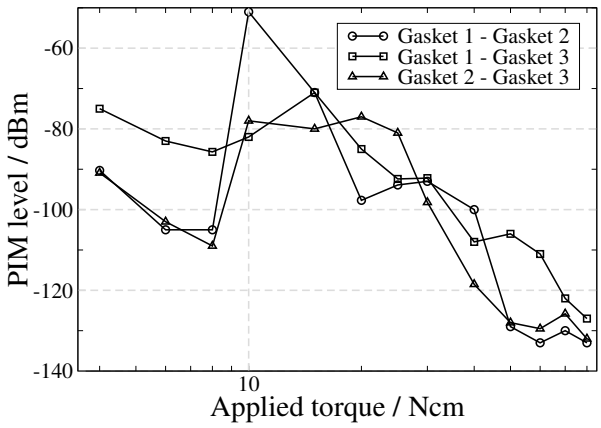

(c) *PIM level versus applied torque when two flat gaskets are inserted.*

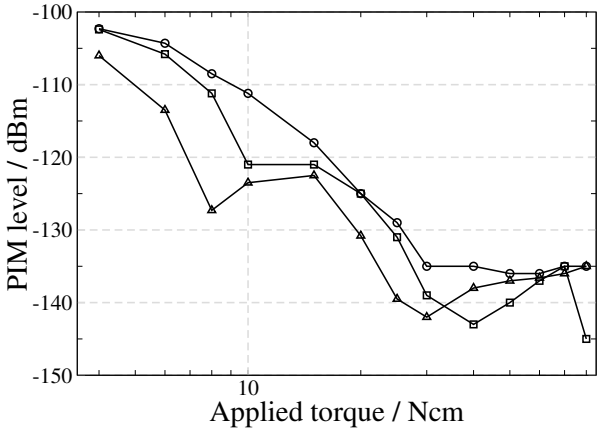

(d) *PIM level versus applied torque without gaskets.*

Figure D.1: *Effect of inserting hard gold gaskets on the junction, P = 60 W.*

D.1.2 Beryllium-Copper gaskets

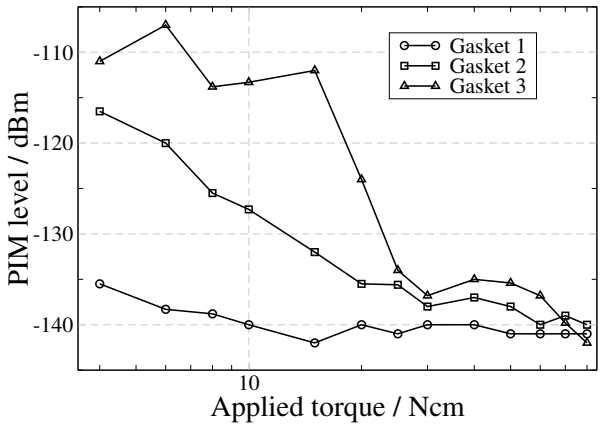

(a) *PIM level versus applied torque when one flat gasket is inserted.*

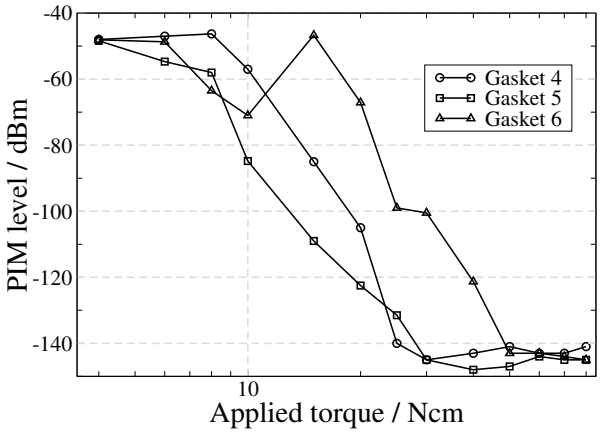

(b) *PIM level versus applied torque when one bridged gasket is inserted.*

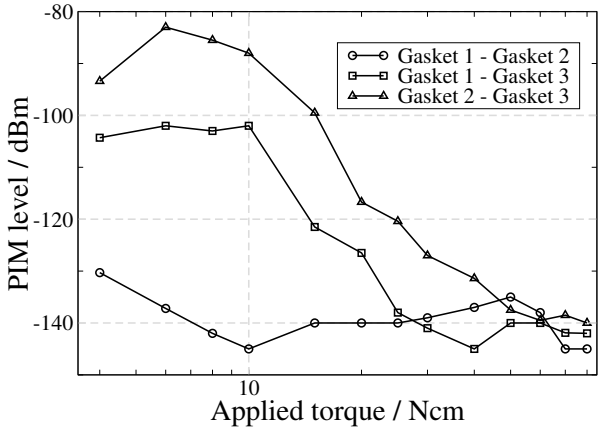

(c) *PIM level versus applied torque when two flat gaskets are inserted.*

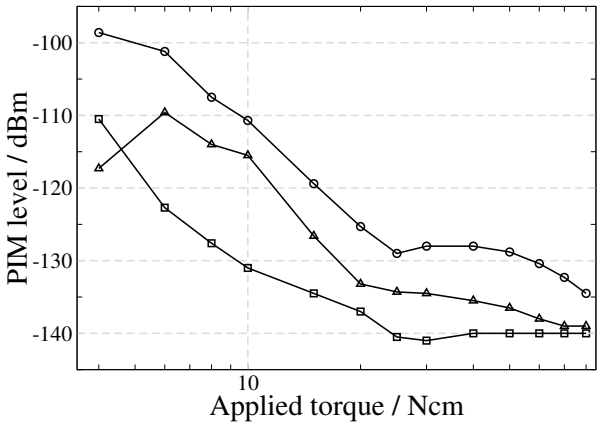

(d) *PIM level versus applied torque without gaskets.*

Figure D.2: *Effect of inserting BeCu gaskets on the junction, P = 60 W.*

D.1.3 Indium Gaskets

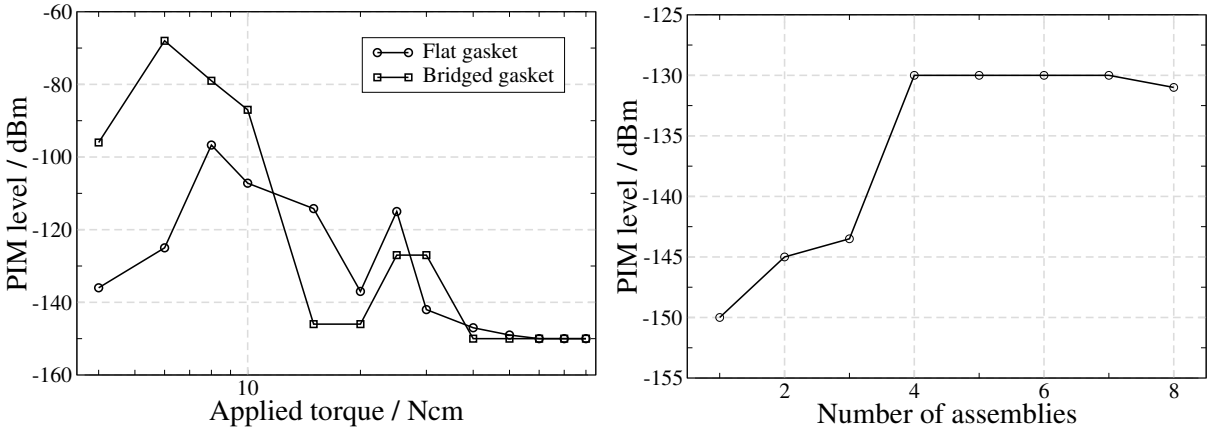

(a) *PIM level versus applied torque when one gasket is inserted.*

(b) *Effect of assembly/disassembly cycles.*

Figure D.3: *Effect of inserting indium gaskets on the junction, $P = 60$ W.*

D.1.4 Seal sheets for the contact evaluation

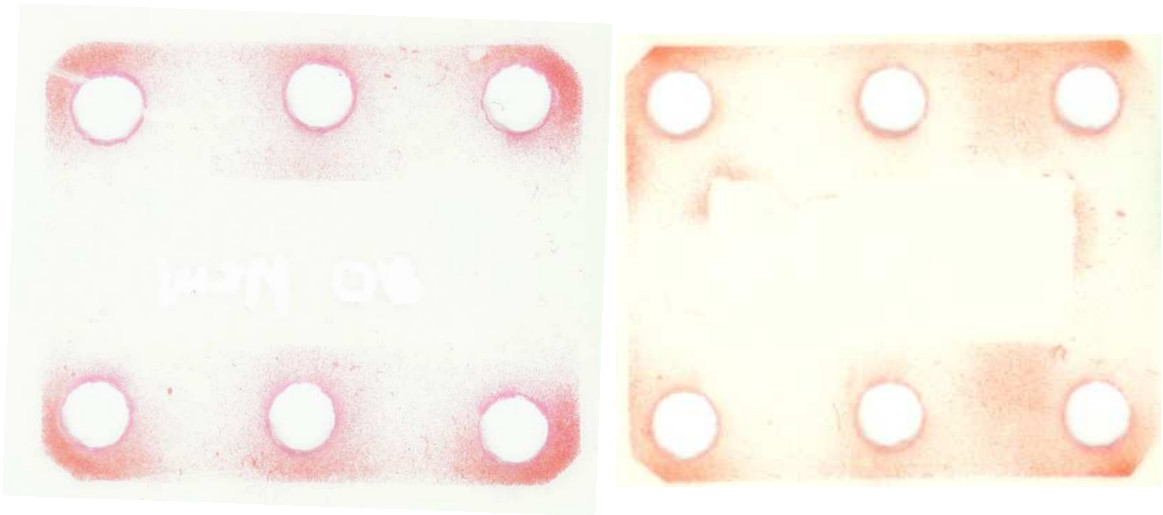

(a) *Seal for the case that no gasket is introduced.*

(b) *Seal for the case that two flat gaskets are inserted.*

Figure D.4: *Seal of an aluminium waveguide connection and the case in which a flat gasket is inserted.*

D.2 Silver-plated aluminium waveguides

D.2.1 Hard gold gaskets

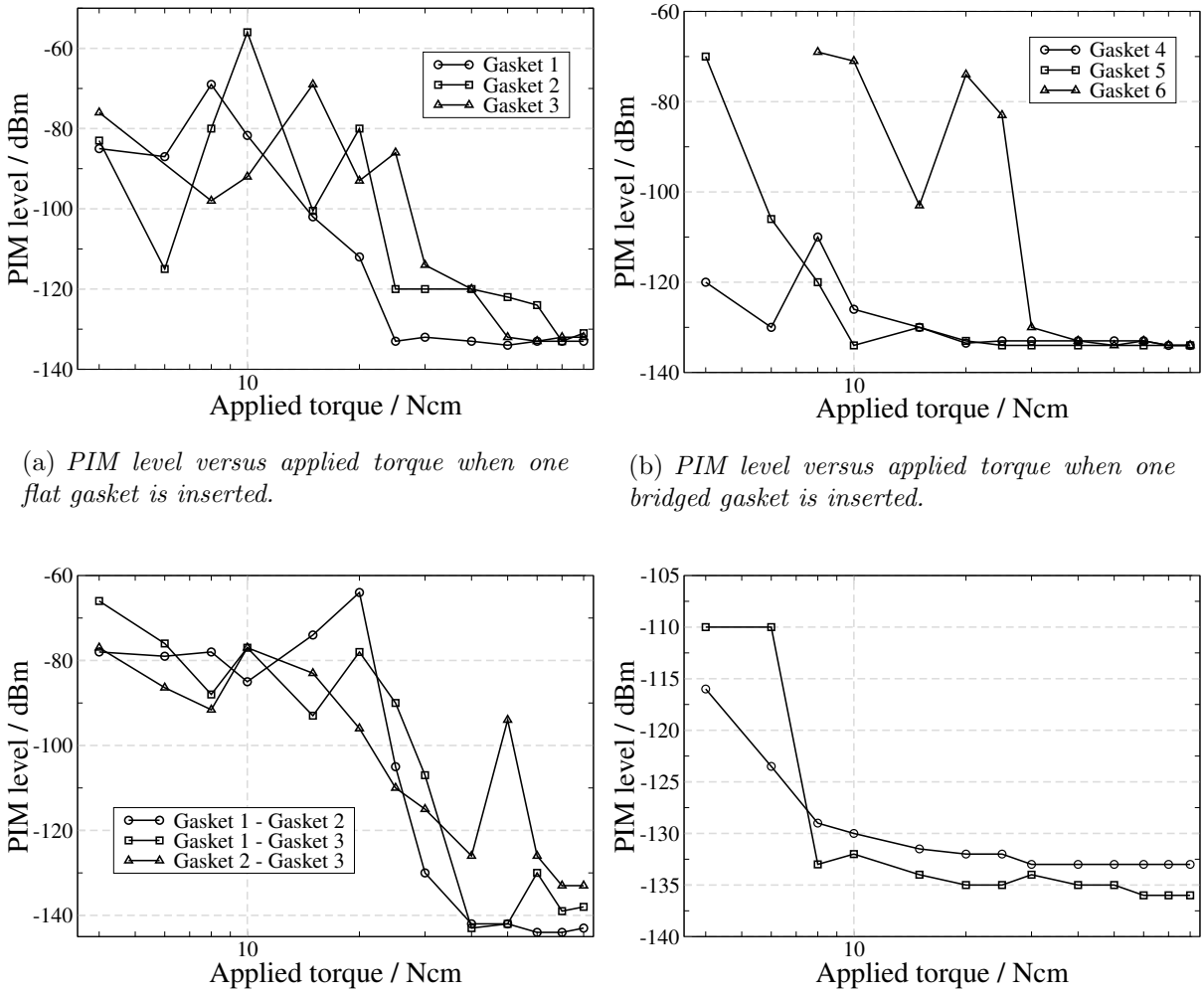

(a) *PIM level versus applied torque when one flat gasket is inserted.*

(b) *PIM level versus applied torque when one bridged gasket is inserted.*

(c) *PIM level versus applied torque when two flat gaskets are inserted.*

(d) *PIM level versus applied torque without gaskets.*

Figure D.5: *Effect of inserting hard gold gaskets on the junction, P = 340 W.*

D.2.2 Beryllium-Copper gaskets

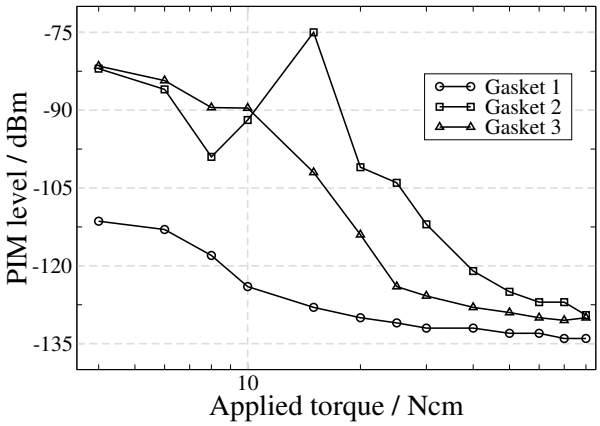

(a) *PIM level versus applied torque when one flat gasket is inserted.*

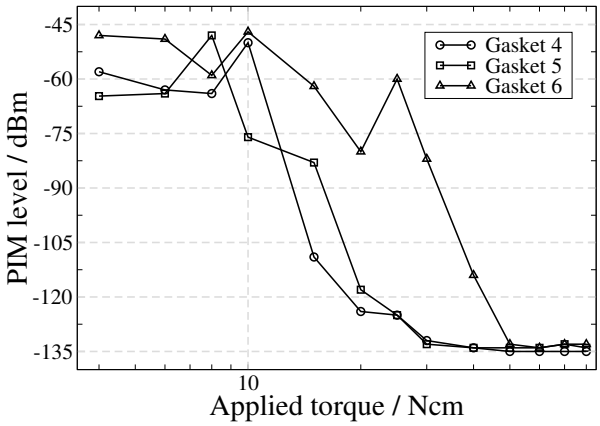

(b) *PIM level versus applied torque when one bridged gasket is inserted.*

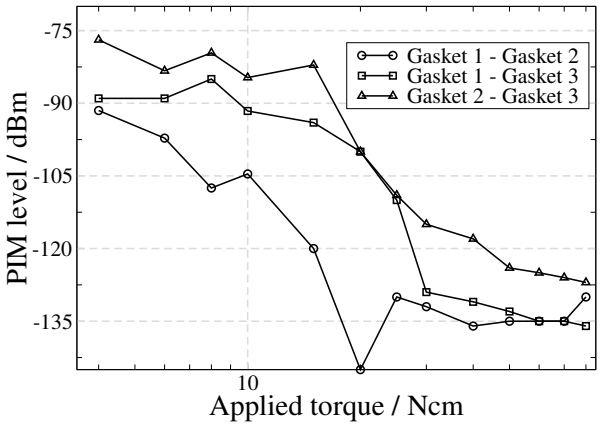

(c) *PIM level versus applied torque when two flat gaskets are inserted.*

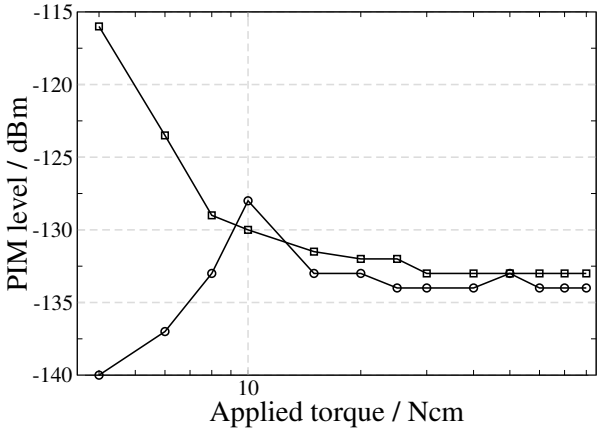

(d) *PIM level versus applied torque without gaskets.*

Figure D.6: *Effect of inserting BeCu gaskets on the junction, P = 340 W.*

D.2.3 Indium gaskets

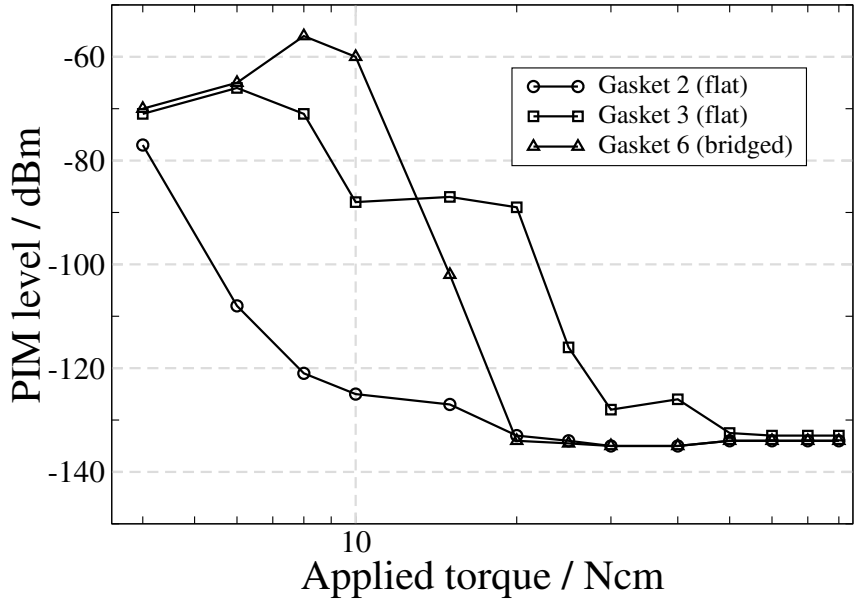

Figure D.7: *Effect of inserting indium gaskets on the junction, P = 340 W.*

Appendix E

Test components

In this appendix all the samples used for testing the software are displayed. If possible, photographs showing the samples themselves are presented. Additionally, the electric field is plotted in order to show the high field regions which are, in principle, more prone to develop a corona discharge. The frequency chosen for plotting the field is the same as at which the corona measurements have been performed. The S parameters are also shown in order to characterise each component. The samples shown are:

- H-Band transformer gap operating at 7.4 GHz.
- X-Band transformer gap operating at 9.5 GHz.
- X-Band bandpass filter operating at 9.5 GHz.
- X-Band lowpass filter operating at 9.5 GHz.
- Ku-Band lowpass filter operating at 12.2 GHz.
- Ku-Band lowpass filter operating at 12.5 GHz.
- Ku-Band lowpass filter showing the effects of a discharge.

E.1 H-Band transformer gap operating at 7.4 GHz

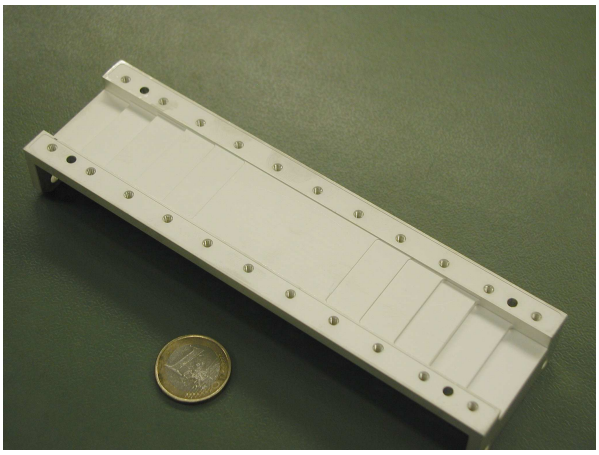

(a) *Photograph of the half part of the sample. Courtesy of Tesat-Spacecom GmbH & Co. KG.*

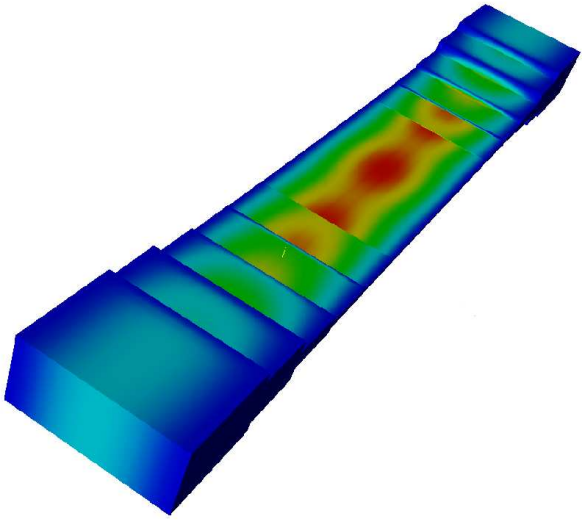

(b) *Electric field in the structure at 7.4 GHz.*

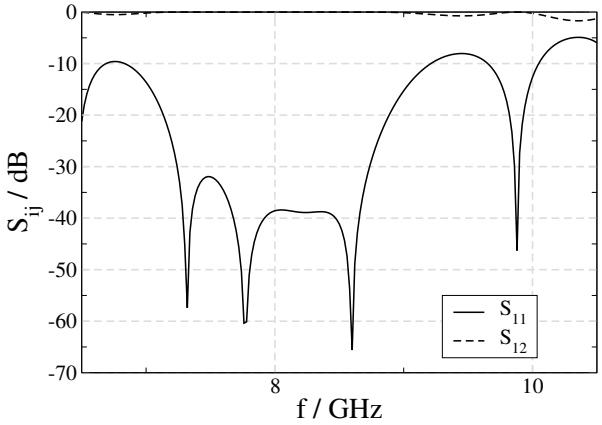

(c) *S parameters.*

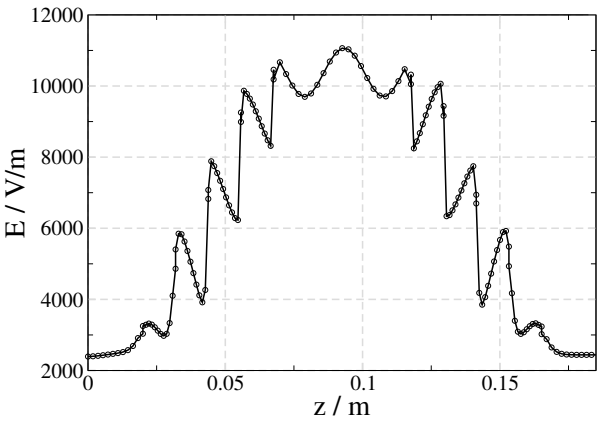

(d) *Electric field at the centre of the structure along the z-axis at 7.4 GHz.*

Figure E.1: *Geometry and electromagnetic response of the component.*

E.2 X-Band transformer gap operating at 9.5 GHz

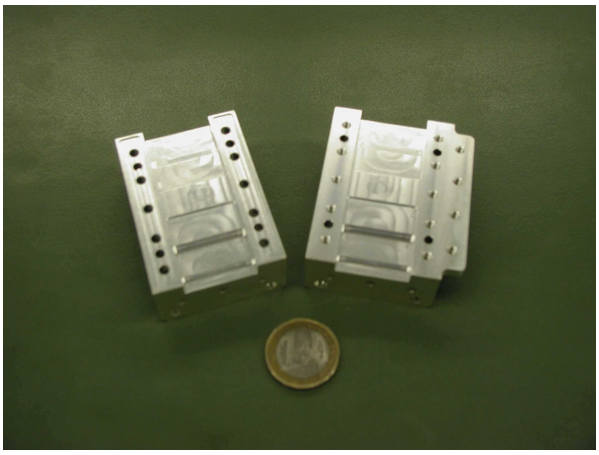

(a) *Photograph of the structure.*

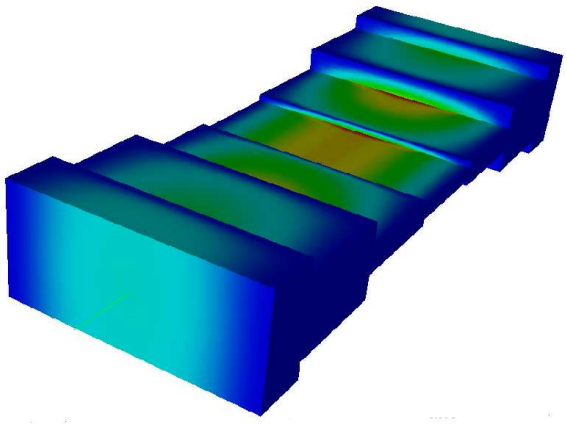

(b) *Electric field in the structure at 9.5 GHz.*

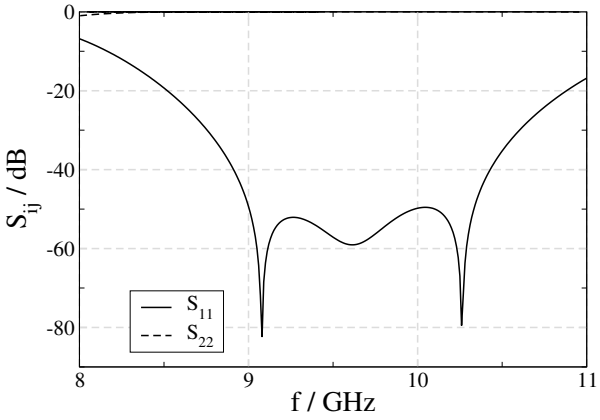

(c) *S parameters.*

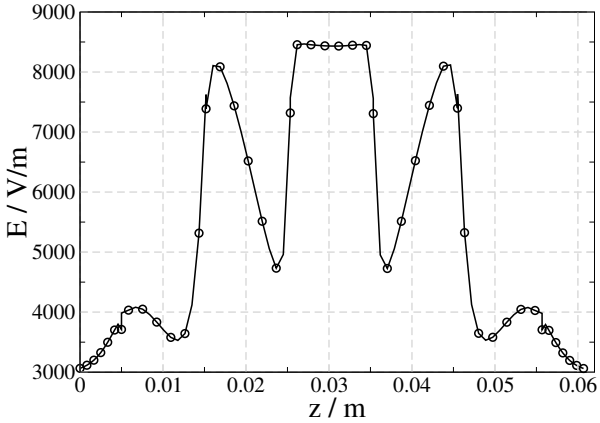

(d) *Electric field at the centre of the structure along the z-axis at 9.5 GHz.*

Figure E.2: *Geometry and electromagnetic response of the component.*

E.3 X-Band bandpass filter operating at 9.5 GHz

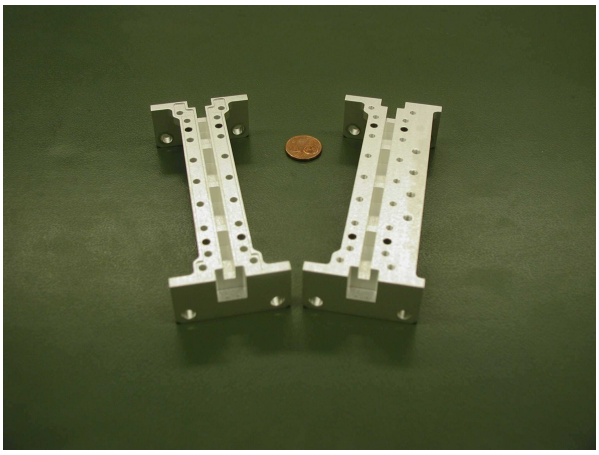

(a) *Photograph of the structure.*

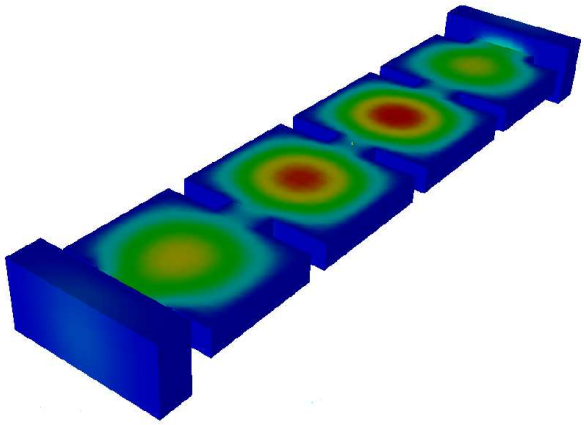

(b) *Electric field in the structure at 9.5 GHz*

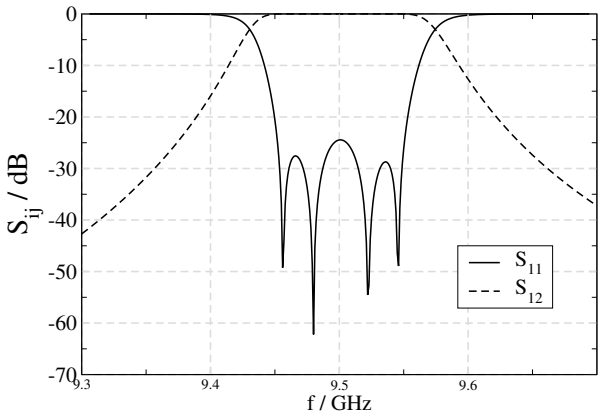

(c) *S parameters.*

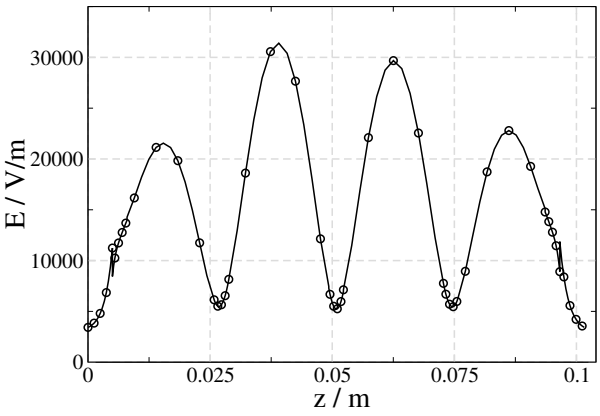

(d) *Electric field at the centre of the structure along the z-axis at 9.5 GHz.*

Figure E.3: *Geometry and electromagnetic response of the component.*

E.4 X-Band lowpass filter operating at 9.5 GHz

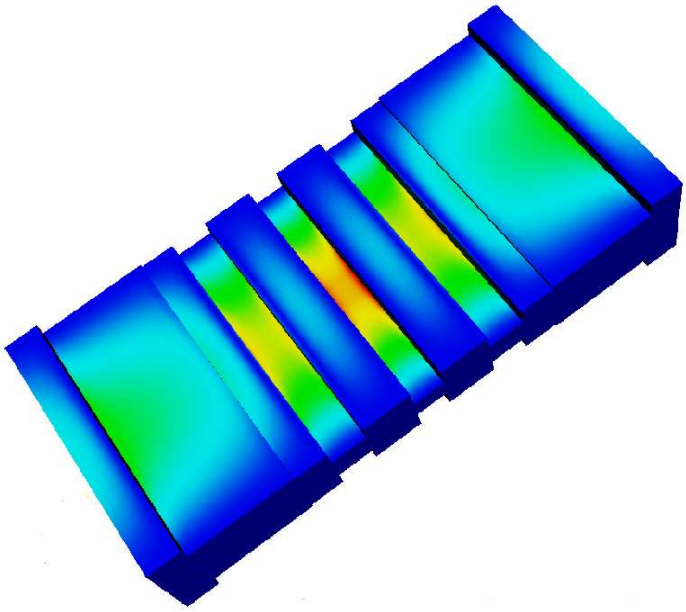

(a) *Electric field in the structure at 9.5 GHz.*

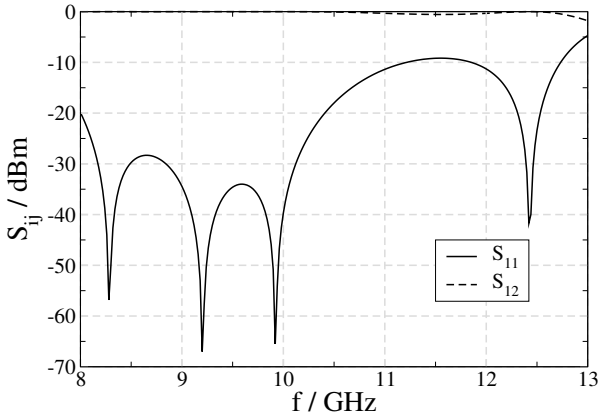

(b) *S parameters.*

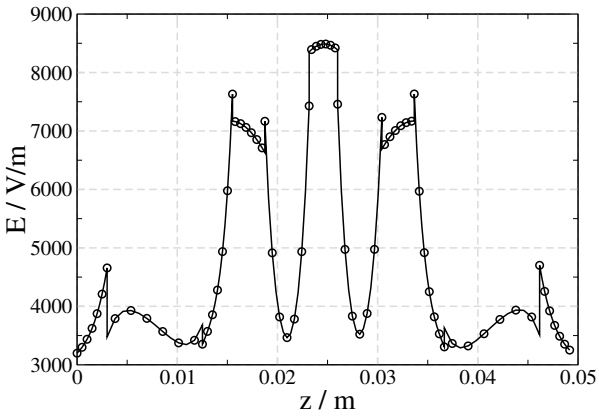

(c) *Electric field at the centre of the structure along the z-axis at 9.5 GHz.*

Figure E.4: *Geometry and electromagnetic response of the component.*

E.5 Ku-Band lowpass filter operating at 12.2 GHz

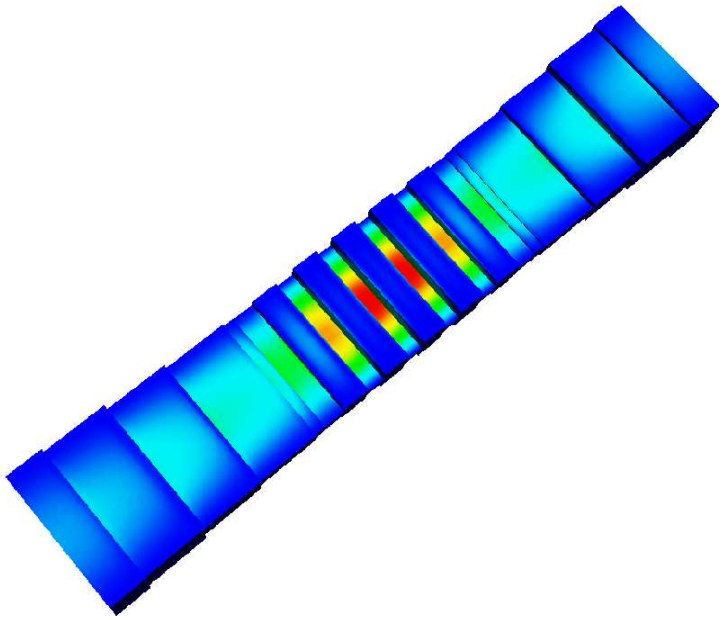

(a) *Electric field in the structure at 12.2 GHz.*

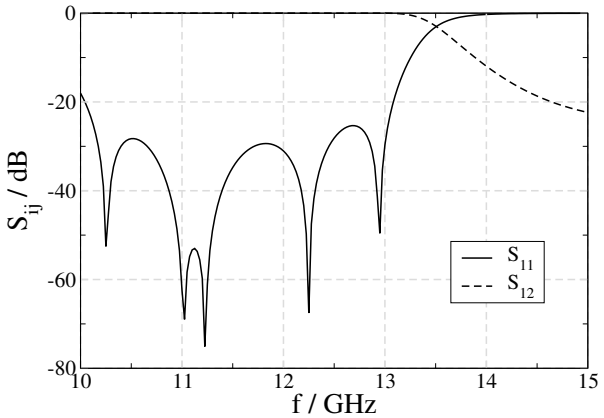

(b) *S parameters.*

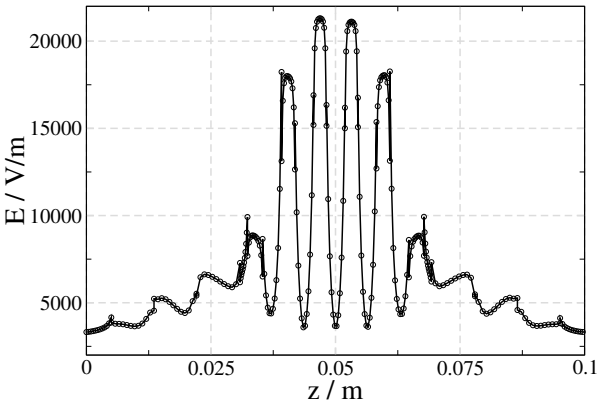

(c) *Electric field at the centre of the structure along the z-axis at 12.2 GHz.*

Figure E.5: *Geometry and electromagnetic response of the component.*

E.6 Ku-Band lowpass filter operating at 12.5 GHz

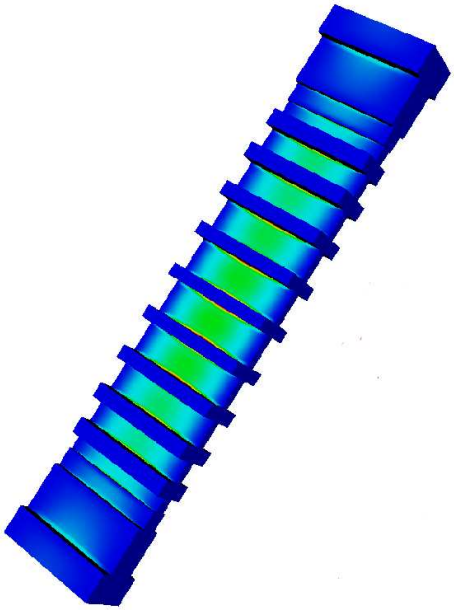

(a) *Electric field in the structure at 12.5 GHz.*

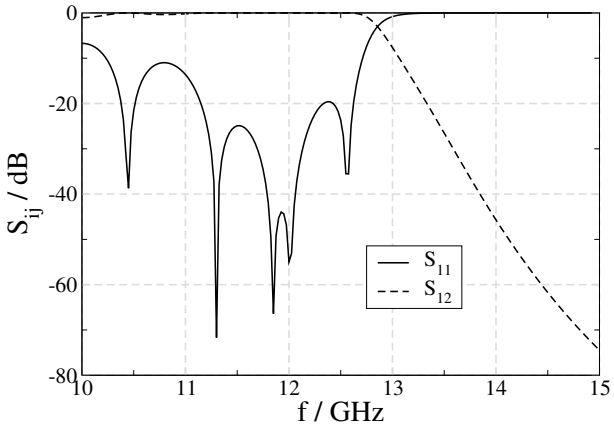

(b) *S parameters.*

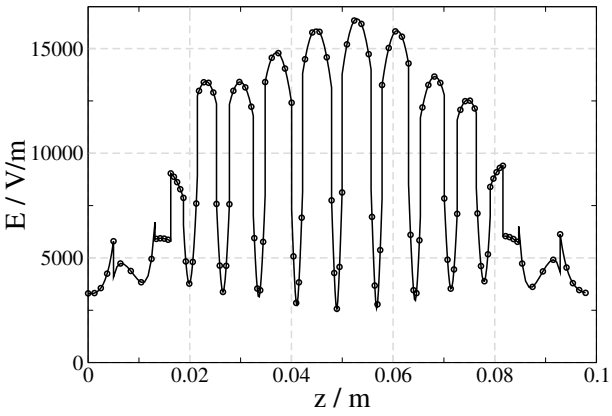

(c) *Electric field at the centre of the structure along the z-axis at 12.5 GHz.*

Figure E.6: *Geometry and electromagnetic response of the component. Courtesy of Tesat-Spacecom GmbH & Co. KG.*

E.7 Ku-Band lowpass filter showing the effects of a discharge

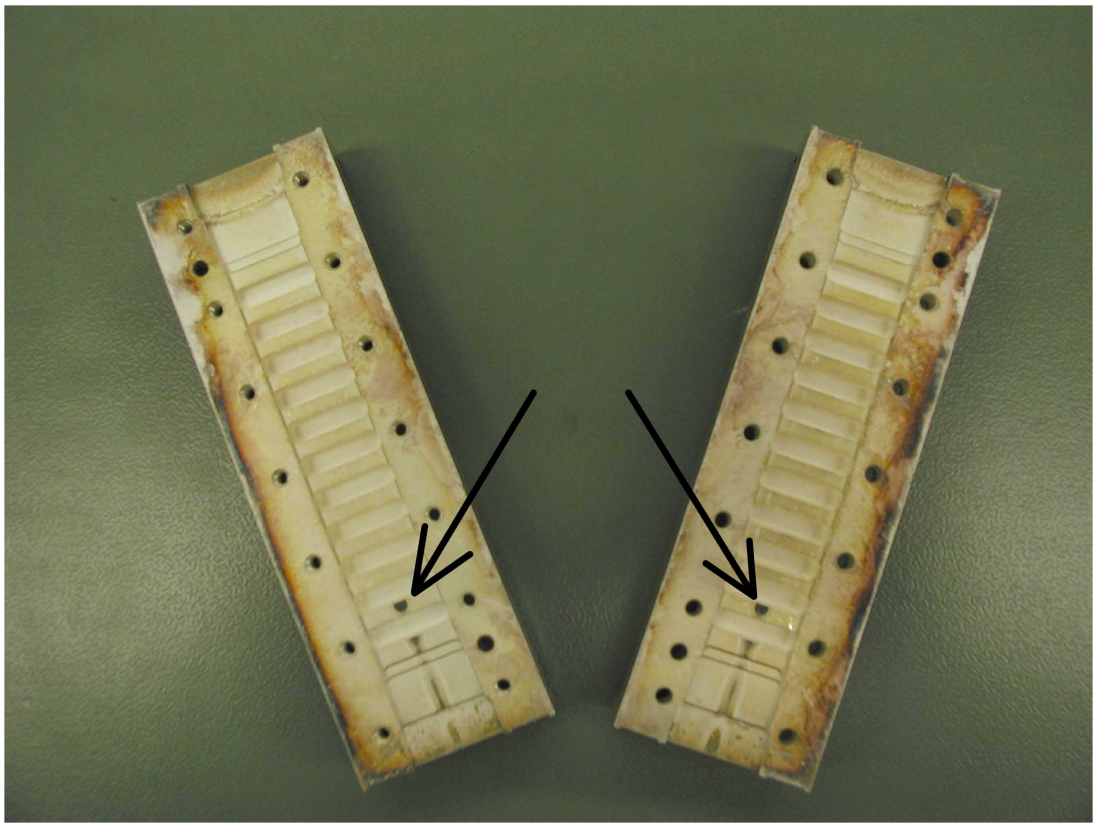

Figure E.7: *A lowpass filter showing the effects of the development of an arc produced by a corona discharge. Courtesy of Tesat-Spacecom GmbH & Co. KG.*

Bibliography

[1] P. L. Lui, "Passive Intermodulation interference in communication systems", *Electronics & Communication Engineering Journal*, pp. 109–118, June 1990.

[2] R. C. Chapman, J. V. Rootsey, and I. Polidi, "Hidden Threat - Multicarrier Passive Component IM Generation", tech. rep., American Institute of Aeronautics and Astronautics Inc., 1976.

[3] C. F. Hoeber, D. L. Pollard, and R. R. Nicholas, "Passive Intermodulation product generation in high power Comunications Satellites", *A.I.A.A.,* 11^{th} *Communications Satellite Systems Conference*, March 1986.

[4] J. W. Boyhan, H. F. Lenzig, and C. Koduru, "Satellite Passive intermodulation: Systems considerations", *IEEE Transactions on Aerospace and Electronic Systems*, vol. 32, pp. 1058–1064, July 1996.

[5] A. P. Foord and A. D. Rawlings, "A study of Passive Intermodulation interference in space RF Hardware", *ESTEC Contract 111036, Final Report*, May 1992.

[6] S. D. Mitchell, *An Investigation Into Passive Intermodulation Properties of Space Qualified Materials*. PhD thesis, University of Kent, Canterbury, 1996.

[7] R. D. Cox, "Measurement of Waveguide Component and Joint Mixing Products in 6-GHz Frequency Diversity Systems", *IEEE Transactions on Communication Technology*, vol. 18, pp. 33–37, 1970.

[8] E. Weibel and U. Hügel, "Tests Evaluate the Influence of Junctions on PIM", *Microwaves & RF*, pp. 70–80, 1998.

[9] M. Bayrak and F. A. Benson, "Intermodulation products from nonlinearities in transmission lines and connectors at microwave frequencies", *Proceedings of IEE*, vol. 122, pp. 361–367, April 1975.

[10] F. Arazm and F. A. Benson, "Nonlinearities in Metal Contacts at Microwave Frequencies", *IEEE Transactions of Electromagnetic Compatibility*, vol. 3, pp. 142–149, August 1980.

[11] R. H. Martin, "Non-Linearity in RF Cables and Connectors", *ERA Report 2885*, April 1976.

[12] R. H. Martin and A. Williams, "Measurement of Intermodulation Products at UHF in Aircraft Related Situations", *ERA Report 3082*, September 1976.

[13] R. H. Martin, "Predictions of Intermodulation Product levels over the Frequency Range 20 MHz - 5 GHz", *ERA Report 77-2021*, September 1977.

[14] R. H. Martin and A. Williams, "Non-Linearity in RF Cables and Connectors - Supplementary results at UHF", *ERA Report 77-2022*, October 1977.

[15] R. Udiljak, *Multipactor in Low Pressure Gas*. PhD thesis, Chalmers University of Technology, Goteborg, Sweden, 2004.

[16] J. Kunz, "On the Pressure in the Corona Discharge", *Physical Review*, vol. 19, no. 2, pp. 165–172, 1922.

[17] C. S. Fazel, "Time and Pressure Measurements in the Corona", *Physical Review*, vol. 19, no. 2, pp. 157–164, 1922.

[18] M. A. Herlin and S. C. Brown, "Breakdown of a Gas at Microwave Frequencies", *Physical Review*, vol. 74, pp. 291–296, August 1948.

[19] L. M. Hartman, "Theory of High Frequency Gas Discharges. III. High Frequency Breakdown", *Physical Review*, vol. 73, pp. 316–325, February 1948.

[20] A. D. MacDonald and S. C. Brown, "High Frequency Gas Discharge Breakdown in Helium", *Physical Review*, vol. 75, pp. 411–418, February 1949.

[21] S. C. Brown and A. D. MacDonald, "Limits for the Diffusion Theory of High Frequency Gas Discharge Breakdown", *Physical Review*, vol. 76, pp. 1629–1633, December 1949.

[22] W. P. Allis and S. C. Brown, "High Frequency Electrical Breakdown of Gases", *Physical Review*, vol. 87, pp. 419–424, August 1952.

[23] A. D. MacDonald, *Microwave breakdown in gases*. John Wiley & Sons, 1966.

[24] Y. P. Raizer, *Gas Discharge Physics*. Springer, 1991.

[25] W. Woo and J. DeGroot, "Microwave absorption and plasma heating due to microwave breakdown in the atmosphere", *IEEE Physical Fluids*, vol. 27, no. 2, pp. 475–487, 1984.

[26] D. J. DeBitetto and L. H. Fisher, "Townsend Ionization Coefficients and Uniform Field Breakdown in Hydrogen and Nitrogen at High Pressures", *Physical Review*, vol. 104, pp. 1213–1220, December 1956.

[27] D. J. DeBitetto and L. H. Fisher, "Second Townsend Coefficient at High Pressures", *Physical Review*, vol. 111, pp. 390–394, July 1958.

[28] M. A. Harrison and R. Geballe, "Simultaneous Measurement of Ionization and Attachment Coefficients", *Physical Review*, vol. 91, pp. 1–7, July 1953.

[29] A. D. MacDonald, D. U. Gaskell, and H. N. Gitterman, "Microwave Breakdown in Air, Oxygen, and Nitrogen", *Physical Review*, vol. 130, pp. 1841–1850, June 1963.

[30] E. L. Huber, "Breakdown Processes in Nitrogen, Oxygen, and Mixtures", *Physical Review*, vol. 97, pp. 267–274, January 1955.

[31] G. C. Light and E. C. Taylor, "Microwave Breakdown in High-Temperature Air", *Journal of Applied Physics*, vol. 39, pp. 1591–1597, February 1968.

[32] D. G. Anderson, M. Lisak, and P. Lewin, "Thermal Lowering of the Threshold for Microwave Breakdown in Air-Filled Waveguides", *IEEE Transactions on Microwave Theory and Techniques*, vol. 35, pp. 653–656, July 1987.

[33] H. W. Bandel and A. D. MacDonald, "Microwave Breakdown in Air plus H_2O", *Journal of Applied Physics*, vol. 41, pp. 2903–2905, June 1970.

[34] H. F. A. Verhaart and P. C. T. van der Laan, "The influence of water vapor on avalanches in air", *Journal of Applied Physics*, vol. 55, pp. 3286–3292, May 1984.

[35] P. A. Calva and F. P. Espino, "Threshold curves of the various modes of corona discharges in atmospheric air", *IEEE Anual Report- Conference on Electrical Insulation*, pp. 612–615, 1997.

[36] P. M. Platzman and E. H. Solt, "Microwave Breakdown of Air in Nonuniform Electric Fields", *Physical Review*, vol. 119, pp. 1143–1149, August 1960.

[37] D. Anderson, U. Jordan, M. Lisak, and T. Olsson, "Microwave Breakdown in Resonators and filters", *IEEE Transactions on Microwave Theory and Techniques*, vol. 47, pp. 2547–2556, December 1999.

[38] R. Holm, *Electrical Contacts*. 4^{nd} Edition, New York: Springer, 1967.

[39] J. A. Greenwood and J. B. P. Wiliamson, "Contact of Nominally Flat Surfaces", *Proceedings of the Royal Society (London)*, vol. 295, pp. 300–319, 1966.

[40] J. Rudzitis, V. Padamans, E. Bordo, and R. Haytham, "Random process model of rough surfaces contact", *Measurement Science and Technology*, vol. 9, pp. 1093–1097, 1998.

[41] A. Y. Suh and A. A. Polycarpou, "Surface Roughness Characterization of Disks Intended for Extremely High Density Recording", *Magnetic Recording Conference*, pp. 27–29, 2002.

[42] A. Misra, "Mechanistic model for contact between rough surfaces", *Journal of Engineering mechanics*, vol. 126, pp. 475–484, May 1997.

[43] L. Kogut and I. Etsion, "Elastic-Plastic Contact Analysis of a Sphere and a Rigid Flat", *Journal of applied Mechanics*, vol. 69, pp. 657–662, September 2002.

[44] U. Sellgren, S. Bjorklund, and S. Andersson, "A finite element-based model of normal contact between rough surfaces", *Wear*, vol. 254, pp. 1180–1188, 2003.

[45] W. Yan and K. Komvopoulos, "Contact Analysis of elastic-plastic fractal surfaces", *Journal of Applied Physics*, vol. 84, pp. 3617–3624, October 1998.

[46] J. A. Ogilvy, "Numerical simulation of elastic-plastic contact between anisotropic rough surfaces", *Journal of Physics D: Applied Physics*, vol. 25, pp. 1798–1809, December 1992.

[47] C. Y. Poon and R. S. Sayles, "The classification of rough surface contacts in relation to tribology", *Journal of Physics D: Applied Physics*, vol. 25, pp. A249–A256, January 1992.

[48] M. T. Singer, "Electrical Resistance of Random Rough Contacting Surfaces Using Fractal Surface Modeling", in *Proceedings of the Thirty-Seventh IEE Holm Conference*, pp. 73–82, 1991.

[49] L. Kogut and K. Komvopoulos, "Electrical contact resistance theory for conductive rough surfaces", *Journal of Applied Physics*, vol. 94, no. 5, pp. 3153–3162, 2003.

[50] Y. H. Jang and J. R. Barber, "Effect of contact statistics on electrical contact resistance", *Journal of Applied Physics*, vol. 94, pp. 7215–7221, December 2003.

[51] L. Boyer, "Contact Resistance Calculations: Generalizations of Greenwood's Formula including Interface Films", *IEEE Transactions on Components and Packaging Technologies*, vol. 24, pp. 50–58, March 2001.

[52] R. S. Timsit, "Electrical Contact Resistance: Properties of Stationary Interfaces", *IEEE Transactions on Components and Packaging Technology*, vol. 22, pp. 85–97, March 1999.

[53] R. Malucci, "Multispot Model of Contacts Based on Surface Features", in *Proceedings of the 36th IEEE Holm Conference on Electric Contacts*, pp. 625–634, August 1990.

[54] R. D. Naybour and T. Farrell, "Connectors for Aluminum Cables: A Study of the Degradation Mechanisms and Design Criteria for Reliable Connectors", *IEEE Transactions on Parts, Hybrids, and Packaging*, vol. 9, pp. 30–36, March 1973.

[55] H. J. de los Santos, *RF MEMS Circuit Design for Wireless Communications*. Artech House, 2002.

[56] T. A. S. of Mechanical Engineers, *ASME B46. 1-2002: Surface texture (surface roughness, waviness and lay)*. 2002.

[57] E. J. Abbott and F. A. Firestone, "Specifying Surface Quality - a Method Based on Accurate Measurement and Comparison", *Mech. Eng.*, vol. 55, pp. 569–572, 1933.

[58] J. H. Horng, "An Elastic-Plastic Asperity Microcontact Model for Rough Surfaces", *ASME journal of Tribology*, vol. 120, pp. 82–88, 1998.

[59] N. Yu and A. A. Polycarpou, "Contact of Rough Surfaces With Asymmetric Distribution of Asperity Heights", *ASME Journal of Tribology*, vol. 124, pp. 367–376, April 2002.

[60] L. Kogut and I. Etsion, "A Finite Element Based Elastic-Plastic Model for the Contact of Rough Surfaces", *Tribology Transactions*, vol. 46, pp. 383–390, 2003.

[61] J. I. McCool, "Predicting Microfracture in Ceramics via a Microcontact Model", *ASME Journal of Tribology*, vol. 108, pp. 380–386, 1986.

[62] J. I. McCool, "Extending the Capability of the Greenwood Williamson Microcontact Model", *Transactions of the ASME*, vol. 122, pp. 496–502, July 2000.

[63] Y. Zhao, D. M. Maietta, and L. Chang, "An asperity microcontact model incorporating the transition from elastic deformation to fully plastic flow", *Transactions of the ASME*, vol. 122, pp. 86–93, January 2000.

[64] K. L. Johnson, *Contact Mechanics*. Cambridge: Cambridge University Press, 1985.

[65] W. R. Chang, I. Etsion, and D. B. Bogy, "An Elastic-plastic Model for the Contact of Rough surfaces", *ASME journal of Tribology*, vol. 109, pp. 257–263, 1987.

[66] W. R. Chang, I. Etsion, and D. B. Bogy, "Static Friction Coefficient Model for Metallic Rough Surfaces", *ASME journal of Tribology*, vol. 110, pp. 57–63, 1988.

[67] H. Hertz, "On the Contact of Elastic Bodies", *Journal fuer die reine und angewandie Mathematic*, vol. 92, pp. 156–171, 1881.

[68] K. A. Nuri and J. Halling, "The normal approach between rough flat surfaces in contact", *Wear*, vol. 32, pp. 81–93, 1975.

[69] K. Komvopoulos and N. Ye, "Three-Dimensional Contact Analysis of Elastic-Plastic Layered Media With Fractal Surface Topographies", *Transactions of the ASME*, vol. 123, pp. 632–640, July 2001.

[70] N. Ye and K. Komvopoulos, "Indentation analysis of elastic-plastic homogeneous and layered media: Criteria for determining the real material hardness", *Journal of Tribology*, vol. 125, pp. 685–691, October 2003.

[71] Z. Q. Gong and K. Komvopoulos, "Mechanical and Thermomechanical elastic-plastic contact analysis of layered media with patterned surfaces", *Journal of Tribology*, vol. 126, pp. 9–17, January 2004.

[72] H. J. Mathieu, M. Datta, and D. Landolt, "Thickness of natural oxide films determined by AES and XPS with/without sputtering", *Journal of Vacuum Science and Technology*, vol. 3, pp. 331–335, March/April 1985.

[73] M. Vladimirescu, R. Kwiatkowsky, and K. Engel, "Passive Intermodulation Distortion in RF Coaxial Electro-Mechanical Switches for Space Applications", in *Proceedings of the 4th International ESA Workshop in Multipactor, Corona and Passive Intermodulation*, (Noordwijk, The Netherlands), September 2003.

[74] Y. V. Sharvin *Soviet Physics JETP*, vol. 21, p. 655, 1965.

[75] A. Mikrajuiddin, F. G. Shi, H. K. Kim, and K. Okuyama, "Size-dependent electrical constriction resistance for contacts of arbitrary size: from Sharvin to Holm limits.", *Material Science in Semiconductor Processing*, vol. 2, pp. 321–327, 1999.

[76] M. Antler, "Contact Resistance of Oxidized Metals: Dependence on the Mating Material", *IEEE Transactions on Components, Hybrids, and Manufacturing Technology*, vol. 10, pp. 420–424, September 1987.

[77] J. R. Osias and J. H. Tripp, "Mechanical Disruption of surface films on metal", *Wear*, vol. 9, pp. 388–397, 1966.

[78] J. V. Rootsey, "Intermodulation Study. (Intermodulation products in Satellite ground antennas)", tech. rep., Philco-Ford Corporation, August 1973.

[79] S. Sze, *Physics of semiconductor devices.* 2^{nd} Edition: John Wiley & sons, 1981.

[80] A. Bohm, *Quantum Theory.* Englewood Cliffs, New Jersey: Prentice-Hall, Inc., 1951.

[81] J. Singh, *Quantum Mechanics: Fundamentals & Applications to Technology.* New York: John Wiley & sons, 1997.

[82] C. Kittel, *Introduction to Solid State Physics.* 2^{nd} Edition, New York: John Wiley & sons, 1956.

[83] J. G. Simmons, "Potential Barrier Shape Determination in Tunnel Junctions", *Journal of Applied Physics*, vol. 10, p. 10, 1963.

[84] A. Sommerfeld and H. A. Bethe, *Handbuch der Physik von geiger und Scheel*, vol. 24/2. Berlin, 1933: Julius Springer-Verlag, 1933.

[85] R. Holm, "The Electric Tunnel Effect across Thin Insulator Films in Contacts", *Journal of Applied Physics*, vol. 22, p. 569, 1951.

[86] J. G. Simmons, "Generalized formula for the electric tunnel effect between similar electrodes separated by a thin insulating film", *Journal of Applied Physics*, vol. 34, pp. 1793–1803, January 1963.

[87] J. G. Simmons, "Potential barriers and emission-limited current flow between closely spaced parallel metal electrodes", *Journal of Applied Physics*, vol. 35, pp. 2472–2481, August 1964.

[88] J. Kadlec, "Temperature dependence of the tunnel current in sandwiches: Does the barrier change with temperature?", *Solid-State Electronics*, vol. 17, pp. 469–475, 1973.

[89] M. Sunjic and L. Marusic, "Dynamical effects in electron tunneling: Self-consistent semiclassical image potentials", *Physical Review B*, vol. 44, p. 9092, October 1991.

[90] M. Nakayama, J. Yanagisawa, F. Wakaya, and K. Gamo, "Focused Ion Beam Process for Formation of a Metal/Insulator/Metal Double Tunnel Junction", *Jpn. Journal of Applied Physics, Part 1*, no. 38, p. 7151, 1999.

[91] J. Fransson, O. Eriksson, and I. Sandalov, "Effects of non-orthogonality in the time-dependent current through tunnel junctions", *Physical review*, vol. 64, September 2001.

[92] H. A. Bethe, "Theory of Boundary Layer of Crystal Rectifiers", *MIT Radiat. Lab. Rep.*, vol. 43, p. 12, 1942.

[93] J. G. Simmons, "Generalized thermal J-V characteristic for the electric tunnel effect", *Journal of Applied Physics*, vol. 35, pp. 2655–2658, September 1964.

[94] M. Braunovic and M. Marjanov, "Thermoelastic Ratchening Effect in Bolted Aluminium-to-Aluminium Connections", *IEEE Transactions on Components, Hybrids, and Manufacturing Technology*, vol. 11, pp. 54–63, March 1988.

[95] I.-K. Cho, J. T. Kim, M. Y. Jeong, T.-G. Choy, and Y. I. Kang, "Analysis and Optimization of Passive Intermodulation in Microwave Coaxial Cavity Filters", *ETRI Journal*, vol. 25, pp. 133–139, April 2003.

[96] J. Z. Wilcox and P. Molmud, "Thermal Heating Contribution to Intermodulation Fields in Coaxial Waveguides", *IEEE Transactions on Communications*, vol. 24, pp. 238–243, February 1976.

[97] E. Hallen, *Electromagnetic Theory*. 37 Essex Street, London: Chapman & Hall Ltd, 1962.

[98] C. A. Balanis, *Advanced Engineering Electromagnetic*. New York: John Wiley & sons, 1989.

[99] L. Kogut and K. Komvopoulos, "Electrical Contact Resistance Theory for Conductive Rough Surfaces Separated by a Thin Insulating Film", *Journal of Applied Physics*, vol. 95, pp. 576–585, 2004.

[100] F. Suarez, C. Palacios, C. Montesano, and F. Rueda, "A Titanium coating tested in Passive Intermodulation", in *Proceedings of the 4th International ESA Workshop in Multipactor, Corona and Passive Intermodulation*, (Noordwijk, The Netherlands), September 2003.

[101] P. Bolli, S. Selleri, and G. Pelosi, "Passive Intermodulation on Large Reflector Antennas", *IEEE Antenna's and Propagation Magazine*, vol. 44, pp. 13–20, October 2002.

[102] C. D. Bond, C. S. Guenzer, and C. A. Carosella, "Intermodulation generation by electron tunneling through Aluminium-Oxide films", *Proceedings of the IEEE*, vol. 67, pp. 1643–1652, December 1979.

[103] C. K. Chow, "Effect of Insulating-Film-Thickness Nonuniformity on Tunnel Characteristics", *Journal of Applied Physics*, vol. 34, pp. 2599–2602, September 1963.

[104] Z. Hurych, "Influence on Non-Uniform Thickness of Dielectric Layers on Capacitance and Tunnel Currents", *Solid-State Electronics*, vol. 9, pp. 967–979, 1966.

[105] C. G. Karagiannopoulos, P. D. Bourkas, C. T. Dervos, and C. A. Kagarakis, "Physical Interpretations Concerning Nonlinear Conductivity Phenomena Across No-Load Switching Contacts", *IEEE Transactions on Components, Hybrids, and Manufacturing Technology*, vol. 14, pp. 137–142, March 1991.

[106] N. B. Carvalho and J. C. Pedro, "Large - and Small-Signal IMD Behavior of Microwave Power Amplifiers", *Microwave Theory and Techniques, IEEE Transactions on*, vol. 47, pp. 2364–2374, December 1999.

[107] "Brush Wellman webpage." http://www.brushwellman.com.

[108] S. Willibald, *Bolted Connections for Rectangular Hollow Sections under Tensile Loading*. PhD thesis, Universitat Fridericiana zu Karlsruhe, Karlsruhe, Germany, 2003.

[109] S. Song and K. P. Moran, "Thermal and electrical resistances of bolted joints between plates of unequal thickness", *Semiconductor Thermal Measurement and Management Symposium, 1993. SEMI-THERM IX., Ninth Annual IEEE*, pp. 28–34, February 1993.

[110] M. Beyer, W. Boeck, K. Möller, and W. Zaengl, *Hochspannungstechnik: Theoretische und praktische Grundlagen für die Anwendung*. Springer-Verlag, 1986.

[111] A. Hatch and H. Williams, "The secondary electron resonance mechanism of Low-Pressure High-Frequency gas breakdown", *IEEE journal of Applied Physics*, vol. 25, p. 417, April 1954.

[112] T. K. Gaisser, *Cosmic Rays and Particle Physics*. Cambridge University Press, 1990.

[113] S. Chapman, "The absorption and dissociative ionizing effect on monochromatic radiation in an atmosphere on a rotating earth", *Proceedings of Physical Society*, vol. 43, pp. 26–45, January 1931.

[114] D. Anderson, M. Lisak, and T. Lewin, "Breakdown in air-filled microwave waveguides during pulsed operation", *Journal of Applied Physics*, vol. 56, pp. 1414–1419, September 1984.

[115] "The Siglo Data base, CPAT and Kinema Software." http://www.siglo-kinema.com.

[116] U. Jordan, *Microwave Breakdown Physics and Applications*. PhD thesis, Chalmers University of Technology, Goteborg, Sweden, 2002.

[117] A. Woode and J. Petit, "Diagnostic investigations into the multipactor effect, susceptibility zone measurements and parameters affecting a discharge", *ESA- Working paper No.1556-*, November 1989.

[118] W. H. Press, B. P. Flannery, S. A. Teukolsky, and W. T. Vetterling, *Numerical Recipes: The Art of Scientific Computing*. Cambridge (UK) and New York: Cambridge University Press, 1st ed., 1986.

[119] J. Meixner, "The Behaviour of Electromagnetic Fields at Edges", *IEEE Transactions on Antennas and Propagation*, vol. 20, pp. 442–446, July 1972.

[120] I. M. Braver, P. S. Fridberg, K. L. Garb, and I. Yakover, "The Behaviour of the Electromagnetic Field Near the Edge of a Resistive Half-Plane", *IEEE Transactions on Antennas and Propagation*, vol. 36, pp. 1760–1768, December 1988.

[121] I. Farina and T. Rozzi, "Numerical Investigation of the Field and Current Behavior Near Lossy Edges", *IEEE Transactions on Microwave Theory and Techniques*, vol. 49, pp. 1355–1358, July 2001.

[122] D. Raboso, *Private communication*. European Space Agency (ESA).

[123] D. Raboso, *ESA internal report (not classified)*. European Space Agency (ESA).

[124] D. Wolk, U. Woechner, K.-G. Hampf, and W. Hartmann, *Private communication*. Tesat-Spacecom GmbH & Co. KG.

[125] C. Vicente, "Intermodulation at waveguide flanges", 2002. Diploma de Estudios Avanzados, D.E.A., University of Valencia, Valencia, Spain.

Curriculum Vitae

Carlos Pascual Vicente Quiles

Date of birth: 12 September 1976

Place of birth: Elche (Alicante), Spain

Marital status: Single

Education

- 1981-1989 - Baix Vinalopo primary school in Elche (Spain).
- 1989-1994 - Carrus high school in Elche (Spain).
- 1994-1999 - Degree of Physics in the University of Valencia (Spain).
- 1999-2001 - Advanced Studies Diploma (D.E.A.).
- 2001-2005 - PhD Thesis at the Technical University of Darmstadt.

Professional experience

- 2001-2005 - Research Assistant at the Technical University of Darmstadt(TUD).